

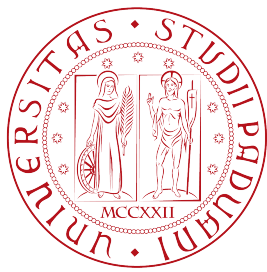
UNIVERSITÀ DEGLI STUDI DI PADOVA
DEPARTMENT OF INFORMATION ENGINEERING
Master Thesis in Telecommunication Engineering

DESIGN OF REAL-TIME OPTICAL COHERENCE
TOMOGRAPHY

Master Candidate
GIANLUCA MARCON

Supervisor
LUCA PALMIERI

April 18, 2018
Academic Year 2017/2018



UNIVERSITÀ DEGLI STUDI DI PADOVA
DEPARTMENT OF INFORMATION ENGINEERING
Master Thesis in Telecommunication Engineering

DESIGN OF REAL-TIME OPTICAL COHERENCE
TOMOGRAPHY

Master Candidate
GIANLUCA MARCON

Supervisor
LUCA PALMIERI

April 18, 2018
Academic Year 2017/2018

*If one feels the need of something
grand, something infinite,
something that makes one feel
aware of God, one need not go
far to find it. I think that I see
something deeper, more infinite,
more eternal than the ocean in
the expression of the eyes of a
little baby when it wakes in the
morning and coos or laughs
because it sees the sun shining
on its cradle.*

Vincent van Gogh

Dedicated to my niece, Teresa.

April 2018

ABSTRACT

Optical Coherence Tomography (OCT) is a non-invasive imaging technique that exploits the coherence property of light to generate 2-D (cross-sectional) and 3-D (volumetric) images of a live sample from the backscattered electromagnetic field. OCT imaging has found widespread application in medicine, mainly in the areas of *Ophthalmology* and *Angiography*, but also in industrial processes where non destructive or contactless testing is necessary.

There are two main categories of OCT systems: Time-Domain OCT (TD-OCT) and Fourier-Domain OCT (FD-OCT). As the names suggest, the former technique makes use of time domain measurements, while the latter takes advantage of the frequency contents of the reflected signals. FD-OCT offers significant advantages over TD-OCT, such as faster scanning rates, better imaging resolution, and enhanced sensitivity, while at the same time requiring no mechanical movements of critical components such as lenses or collimators.

In this thesis I focus on a particular FD-OCT technique called Swept-Source OCT (SS-OCT), which uses a rapidly tunable narrow band laser as a light source. A working SS-OCT system capable of real-time imaging is fully developed, along with the data-acquisition and signal-processing modules needed for a complete tomographic imaging device.

Future development includes the migration of the signal processing stack on a Graphics Processing Unit (GPU) in order to enhance the performance of the system making use of the General-Purpose computing on Graphics Processing Units (GPGPU) paradigm. This approach opens up the possibility to implement more advanced and refined OCT schemes, such as Polarization-Sensitive OCT (PS-OCT) and Speckle Variance OCT (svOCT).

SOMMARIO

La Tomografia a Coerenza Ottica (OCT) è una tecnica di imaging non invasiva che sfrutta la proprietà di coerenza della luce per generare immagini 2-D (a sezioni) e 3-D (volumetriche) di un campione in vivo a partire dalla luce retrodiffusa dallo stesso. La tecnica OCT ha trovato ampio utilizzo nel campo della medicina, in particolare nelle aree dell' *Oftalmologia* e dell' *Angiografia*, ma anche in processi industriali

in cui sono necessarie misure non distruttive e senza contatto.

Vi sono due principali categorie di sistemi OCT: TD-OCT (OCT nel dominio del tempo) e FD-OCT (OCT nel dominio della frequenza). Come suggerisce il nome, la prima di queste due tecniche sfrutta delle misure nel dominio del tempo, mentre la seconda utilizza il contenuto spettrale dei segnali riflessi per ricostruire l'immagine del campione in esame. FD-OCT offre vantaggi significativi rispetto a TD-OCT, come velocità di scansione più elevate, risoluzione più fine e migliore sensitività. Tutto ciò avviene senza che vi siano movimenti meccanici di componenti critici come lenti e collimatori.

In questa tesi lavorerò su un particolare sistema FD-OCT chiamato Swept-Source OCT (ss-OCT) che sfrutta un laser a banda molto stretta e con alta velocità di sintonizzazione. Verrà quindi sviluppato un sistema SS-OCT funzionante, capace di eseguire misure continue e in tempo reale. Il lavoro verterà sulla parte di progettazione e ottimizzazione dello schema ottico e sullo sviluppo di algoritmi per l'acquisizione ed elaborazione dei dati.

Sviluppi futuri verteranno sulla migrazione dell'intero sistema di elaborazione dati su GPU (Graphical Processing Unit) facendo uso del paradigma di General-Purpose computing on Graphics Processing Units (GPGPU), che renderà più efficiente il dispositivo e permetterà la progettazione di tecniche più avanzate come OCT sensibile alla polarizzazione (PS-OCT), per ottenere misure di birifrangenza del campione, o Speckle Variance OCT (svOCT).

In truth, O judges, while I wish to be adorned with every virtue, yet there is nothing which I can esteem more highly than the being and appearing grateful. For this one virtue is not only the greatest, but is also the parent of all the other virtues.

— Marcus Tullius Cicero

ACKNOWLEDGEMENTS

First of all, I would like to thank professor Palmieri, my supervisor, for the opportunity he gave me to work on this project, but mostly for his countless advices which made my job a little easier.

A special thought goes to my class-mates Giacomo, Linda and Caterina, with which I shared these last few months as a university student, and the other lab-mates Riccardo, Leonardo, Gianluca, Francesco and especially Marco, whom I could always rely upon.

I also thank Elena, who was always by my side in the most difficult moments.

Finally, I heartily thank my family for the essential role they played in my life up until now. Thank you Annachiara, Mariella and Giancarlo.

CONTENTS

1	INTRODUCTION	1
1.1	Summary on Optical Coherence Tomography	1
1.2	Applications	3
1.2.1	Medicine	3
1.2.2	Industrial	4
1.2.3	In vivo monitoring of biological specimen	5
1.2.4	Functional imaging	6
1.3	Objectives	6
1.4	Thesis Structure	7
2	BASIC THEORY OF OPTICAL COHERENCE TOMOGRAPHY	8
2.1	Principles of Coherence and Interference	8
2.1.1	Michelson interferometer	10
2.1.2	Fringe visibility	10
2.1.3	The coherence function	12
2.1.4	Coherence length	13
2.2	OCT Terminology	13
2.3	Time Domain OCT	15
2.4	Fourier Domain OCT	18
2.4.1	Spectral Domain OCT	18
2.4.2	Swept-Source OCT	23
3	DESCRIPTION OF THE SETUP	28
3.1	Optical Source	28
3.1.1	Optical Spectrum	28
3.1.2	Axial Resolution	30
3.1.3	Sweep trigger	30
3.1.4	Power profile	31
3.1.5	k-clock	32
3.1.6	Coherence length	34
3.2	Scanning System	36
3.2.1	Collimator	36
3.2.2	Scanning lens	37
3.2.3	Galvanometric Mirrors	40
3.3	Acquisition Board	43
3.3.1	Data Acquisition	44
3.3.2	FFT module	47
3.3.3	External clocking	47
3.3.4	Triggering	48
3.4	Optical Circuit	50
3.4.1	Fiber Couplers	50
3.4.2	Measuring the couplers' length	51
3.4.3	Mach-Zender Interferometer	52
3.4.4	Fiber Michelson interferometer	55

3.4.5	Second scheme	56
3.4.6	Signal-to-noise ratio profile	60
3.4.7	Axial Resolution	61
3.4.8	Thickness measurements	63
4	RESULTS	66
4.1	Data Acquisition Software	66
4.1.1	Controlling the galvanometric mirrors	67
4.1.2	Programming the ATS9350	70
4.1.3	Processing time and delay	74
4.1.4	Saving data to disk	76
4.2	Acquisitions	78
4.2.1	B-scans	78
4.2.2	SS-OCT at 1060 nm	82
4.2.3	En-face images	85
4.2.4	Measuring the transversal resolution	88
4.2.5	Volumetric Data	92
5	CONCLUSIONS	94
A	APPENDIX - OFDR TRACES	96
BIBLIOGRAPHY		98

LIST OF FIGURES

Figure 1.1	OCT and histological images of the human eye.	2
Figure 1.2	Imaging resolution and image penetration compared for different imaging techniques.	3
Figure 1.3	Example of 3D OCT data: human eye obtained with SS-OCT [14] (left) and human finger obtained with SD-OCT [10] (right).	4
Figure 1.4	En-face view for the assessment of macular edema [32].	4
Figure 1.5	Coronary plaque imaged by OCT (left) and Intravascular Ultrasound (IVUS) (right) [24].	5
Figure 1.6	Probe for endoscopic OCT [29].	5
Figure 1.7	Cross-sectional OCT image of a multi-layered plastic foil used in the food packaging industry [43].	5
Figure 1.8	Growth monitoring of <i>Capsicum annuum</i> seeds [35] (left) and lettuce leaf [20] (right).	6
Figure 2.1	Interference fringes created by two beams of equal intensity.	10
Figure 2.2	Diagram of a Michelson interferometer [38].	11
Figure 2.3	Effect of the coherence time of a source on the interference fringes at the output of a Michelson interferometer [38].	11
Figure 2.4	Different types of OCT measurements. [15]	14
Figure 2.5	<i>En-face</i> view reconstructed from volumetric data[15]	14
Figure 2.6	Diagram of the basic TD-OCT setup using a Michelson interferometer.	15
Figure 2.7	Diagram of the basic TD-OCT setup using a Michelson interferometer used in [23].	16
Figure 2.8	Diagram of the basic TD-OCT setup using a Michelson interferometer used in [23].	17
Figure 2.9	Optical ranging setup (left) and measurement (right) of the cornea of the rabbit eye [19].	17
Figure 2.10	Diagram illustrating the different types of OCT modalities.	18
Figure 2.11	Comparison between images of the human retina obtained with standard TD-OCT (left) and high-speed, high-resolution FD-OCT (right).	18
Figure 2.12	Diagram of a typical Spectral-Domain OCT (SD-OCT) scheme.	19

Figure 2.13	SD-OCT interference spectrum generated by two reflective surfaces.	20
Figure 2.14	Interference distortion induced by linear sampling in the λ space.	21
Figure 2.15	Sensitivity falloff in FD-OCT systems [10].	21
Figure 2.16	Artifacts contained in the FD-OCT A-scans[15]	22
Figure 2.17	Complex conjugate artifacts in SD-OCT.	23
Figure 2.18	Diagram of a typical SS-OCT scheme [15]	24
Figure 2.19	Frequency-swept optical source by Axsun [15].	25
Figure 2.20	Complete fiber optic SS-OCT scheme using an external clock source and balanced detection [15].	27
Figure 3.1	The Axsun SSOCT-1310 swept source.	28
Figure 3.2	Spectrum of the Axsun SSOCT-1310 laser, obtained with a 1 nm resolution.	29
Figure 3.3	Sweep trigger of the SSOCT-1310 laser.	31
Figure 3.4	Power profile of the SSOCT-1310 laser.	31
Figure 3.5	Estimate of the instantaneous frequency of the k-clock.	32
Figure 3.6	Behaviour of the useful k-clock at different time instants.	32
Figure 3.7	Estimate of the instantaneous frequency of the k-clock.	33
Figure 3.8	Experimental estimation of the normalized coherence function.	35
Figure 3.9	Diagram of a OCT scanning system.	36
Figure 3.10	Simulation of the spot size at different scan angles.	38
Figure 3.11	Effect of the scanning lens' numerical aperture on spot size and depth of view.	40
Figure 3.12	The Thorlabs GVS002 galvo system.	40
Figure 3.13	Field distortion using two mirrors.	42
Figure 3.14	The final scanning system.	43
Figure 3.15	The acquisition board, AlazarTech ATS9350.	43
Figure 3.16	Diagram highlighting the differences between Sigle-Port acqusitions and Dual-Port acqusitions	45
Figure 3.17	Time diagram of a Traditional AutoDMA acquisition.	46
Figure 3.18	Time diagram of a NPT AutoDMA acquisition.	47
Figure 3.19	Diagram of the FPGA FFT module.	47
Figure 3.20	Example of bad k-clock that requires the use of the dummy clock switchover.	48
Figure 3.21	Diagram of setup for the measurement of fiber couplers' length.	51
Figure 3.22	Diagram of an unbalanced Mach-Zender Interferometer.	52

Figure 3.23	Comparison between the beat frequency acquired with the uniform clock (left) and the k-clock (right). 54
Figure 3.24	Simulated B-scans using the internal 500 MHz clock (top) and the k-clock (bottom). 54
Figure 3.25	SS-OCT setup using a fiber coupler as a Michelson interferometer. 56
Figure 3.26	The reference arm used for this setup. The adjustable fiber collimator (left) and translatable mirror (right) are visible. 56
Figure 3.27	Instability of the laser output power. 57
Figure 3.28	Final SS-OCT setup. 57
Figure 3.29	Time signal when the optical path difference is close to 0. 58
Figure 3.30	OFDR traces used to balance the interferometer. 59
Figure 3.31	Time signal when the optical path difference is close to 0. 60
Figure 3.32	Time signal when the optical path difference is close to 0. 60
Figure 3.33	A-scans of a silver mirror at various imaging depths. 61
Figure 3.34	Signal-to-noise ratio falloff. 61
Figure 3.35	Experimental determination of the axial resolution of the system fitting the A-scan of a silver mirror to a Lorentzian function using a Nonlinear Least Squares method. 63
Figure 3.36	Axial resolution profile on the entire imaging range using four different apodization windows. 64
Figure 3.37	Image of the R1L1S1N target. 64
Figure 3.38	Axial measurement of the R1L1S1N target. 65
Figure 3.39	Axial measurement of a Single Mode Fiber (SMF) with its acrylic coating. 65
Figure 4.1	Data flow of the OCT application. 67
Figure 4.2	Signals used to control the galvanometric mirrors. 68
Figure 4.3	Signals used to control the galvanometric mirrors. 69
Figure 4.4	Processing time at different framerates and varying the number of CPU cores utilized. 75
Figure 4.5	Total delay due to DMA transfer, CPU processing and GPU upload time. 75
Figure 4.6	GPU throughput using OpenGL. 76
Figure 4.7	The SSD write cliff. 77
Figure 4.8	B-scan of the Thorlabs test target. 78

Figure 4.9	B-scans of various samples afflicted by striped artifacts.	79
Figure 4.10	B-scan of an orange peel.	80
Figure 4.11	B-scan of a cherry tomato.	80
Figure 4.12	B-scan of a strawberry.	80
Figure 4.13	B-scan of an onion.	81
Figure 4.14	B-scans of a human finger.	81
Figure 4.15	B-scans of a beef steak.	81
Figure 4.16	Setup of the SS-OCT system working in the 1060 nm range.	82
Figure 4.17	B-scans acquired with the 1060 nm system.	83
Figure 4.18	Birefringence effect on the B-scan of a scotch tape roll.	83
Figure 4.20	<i>En-face</i> view of an orange peel.	85
Figure 4.21	<i>En-face</i> view of sliced cherry tomato.	86
Figure 4.22	<i>En-face</i> images generated using the <i>max</i> (left) and <i>sum</i> (right) methods. From top to bottom: sliced onion, human fingertip, strawberry, orange slice.	87
Figure 4.23	<i>En-face</i> projection of the grid pattern.	88
Figure 4.24	<i>En-face</i> projection of the USAF 1951 test target.	89
Figure 4.25	<i>En-face</i> projection of variable frequency Ronchi rulings.	90
Figure 4.26	<i>En-face</i> projection of the 60, 70 and 80 lp/mm Ronchi gratings.	90
Figure 4.27	<i>En-face</i> projection of the star sector pattern.	91
Figure 4.28	<i>En-face</i> projection of the concentric circles.	91
Figure 4.29	Slicing of a 3D texture.	92
Figure 4.31	Volume rendering of OCT data.	93
Figure 5.1	The Graphical User Interface (GUI) of the final OCT application, showing a B-scan of a finger.	94
Figure A.1	OFDR traces of the first 50-50 coupler (Coupler A).	96
Figure A.2	OFDR traces of the second 50-50 coupler (Coupler B).	97
Figure A.3	OFDR traces of the 90-10 coupler.	97

LIST OF TABLES

Table 1.1	Performance of different implementations of volumetric OCT using GPGPU (adapted from [12]).	2
Table 3.1	Axsun laser datasheet.	29
Table 3.2	Thorlabs F28oAPC-C datasheet.	37
Table 3.3	Thorlabs LSM04 datasheet.	39
Table 3.4	Length of the paths of the fiber couplers.	51
Table 3.5	Path difference of each pair of adjacent ports of the couplers.	51

LISTINGS

ACRONYMS

OCT	Optical Coherence Tomography
SS-OCT	Swept-Source OCT
TD-OCT	Time-Domain OCT
FD-OCT	Fourier-Domain OCT
SD-OCT	Spectral-Domain OCT
PS-OCT	Polarization-Sensitive OCT
svOCT	Speckle Variance OCT
GPGPU	General-Purpose computing on Graphics Processing Units
GPU	Graphics Processing Unit
MZI	Mach-Zender interferometer
OPD	Optical Path Difference
BPD	Balanced Photodiode
OSA	Optical Spectrum Analyzer
SMF	Single Mode Fiber
API	Application Programming Interface

EOCT	Endoscopic Optical Coherence Tomography
IVUS	Intravascular Ultrasound
SEM	Scanning Electron Microscope
MRI	Magnetic Resonance Imaging
DOCT	Doppler OCT
PEG	Photonic and Electromagnetic Group
DEI	Department of Information Engineering
DAQ	data acquisition
DAC	Digital-to-Analog Converter
PZT	piezoelectric transducer
ADC	Analog-to-Digital Converter
SLD	Superluminescent Diode
CCD	charged coupled device
CMOS	complementary metal-oxide semiconductor
SNR	signal-to-noise ratio
FWHM	full-width half-maximum
PSD	power spectral density
OFDI	optical frequency domain interferometry
FFT	Fast Fourier Transform
MEMS	micro electro-mechanical systems
PZT	piezoelectric transducer
EOM	electro-optic modulator
SOA	semiconductor optical amplifier
FDML	Fourier domain mode locking
VCSEL	vertical cavity surface-emitting laser
FPGA	Field Programmable Gate Array
SDK	Software Development Kit
FIFO	First-In First-Out
DMA	Direct Memory Access

LVTTL	Low-Voltage Transistor-Transistor-Logic
OFDR	Optical Frequency-Domain Reflectometer
GUI	Graphical User Interface
API	Application Programming Interface
HDD	Hard Disk Drive
SSD	Solid State Drive
VOA	Variable Optical Attenuator
RAM	Random Access Memory

INTRODUCTION

1.1 SUMMARY ON OPTICAL COHERENCE TOMOGRAPHY

The technique of Optical Coherence Tomography (OCT), firstly introduced in the late 80's by Fujimoto et al. [19] and later improved by Huang et al. [23], was developed for the noninvasive axial and cross-sectional imaging of biological tissues. In a way similar to ultrasonic imaging, 2D images are generated by combining a replica of the impinging electromagnetic radiation with its delayed version reflected by the sample under test.

The advantage over conventional ultrasound techniques is that it permits imaging resolutions that range from 1 to 20 μm , which is up to two orders of magnitude smaller than for ultrasound. This enables the diagnosis of pathologies that were previously only detectable by histological techniques, which have the advantage of higher resolution at the expense of the capability of non-destructive measurement. In fact, histology requires the following steps to be performed on the sample:

- Excision
- Fixation
- Embedding
- Microtoming
- Staining

These operations prevent the use of histology in certain areas where the sample to be analyzed cannot be damaged, such as *Ophthalmology*, a field of medicine which studies the pathologies of the human eyeball and orbit. These characteristics, coupled with its real-time imaging capability, make OCT one of the strongest candidates for this particular branch of medicine.

In Figure 1.1 we can compare the images of a human retina obtained with the first type of OCT technique invented, Time-Domain OCT (TD-OCT) (Figure 1.1a) and histology (Figure 1.1b) [23]. Image quality, while arguably low, is enough to identify and measure the thickness of the main structures of the eye. In Figure 1.1c we can instead see a high quality image of a live sample obtained with the more modern Swept-Source OCT (ss-OCT) technique [14], which allows higher quality measurements and fast image acquisitions.

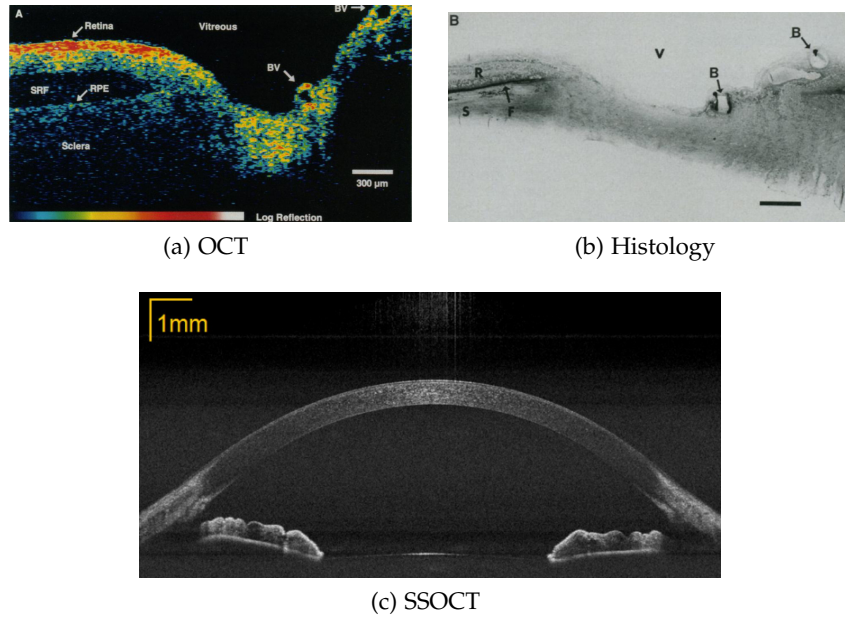


Figure 1.1: Optical coherence tomograph of human retina and optic disk in vitro (top left) and histologic section of the same sample (top right) [23]. On the bottom, a ss-OCT image of a live human eye sample [14].

The first drawback of OCT as a medical imaging technique comes from its relatively low imaging penetration, which is usually between less than a millimeter up to a couple of centimeter, depending on the specific technology and the absorption coefficient of the sample to analyse. In Figure 1.2, a comparison between OCT, Ultrasound, and Confocal Microscopy is available [15]. The trend is that for an increasingly better imaging resolution, imaging depth has to be sacrificed. In this aspect, OCT sits right between the other two techniques, offering micrometer-level resolution for a moderate image penetration.

Whenever cross-sectional images are not sufficient for a correct diagnosis, volumetric data can be exploited for a more in-depth anal-

SOURCE	YEAR	VOXELS	VOL. RATE	SPEED
			Volumes/s	GVoxels/s
Zhang and Kang[47]	2010	6400000	10	0.06
Choi et al. [10]	2012	4194304	41	0.17
Wieser et al. [44]	2014	40960000	26	1.07
Darbrazi [12]	2016	1408800000	2.05	2.89

Table 1.1: Performance of different implementations of volumetric OCT using GPGPU (adapted from [12]).

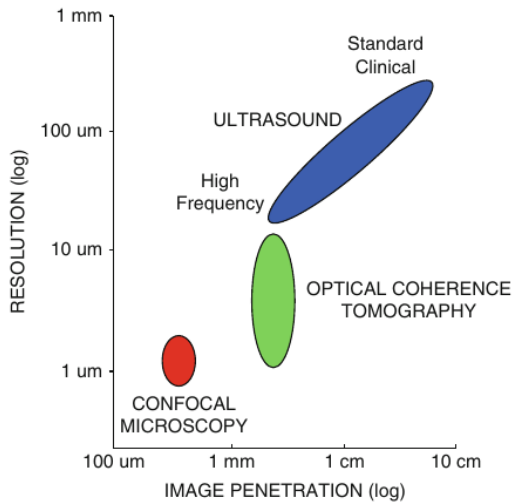


Figure 1.2: Imaging resolution and image penetration compared for different imaging techniques.

ysis. Volumetric images are composed by multiple 2D images captured in succession along a certain scanning direction, creating a 3D grid of datapoints called Voxels. Two examples of 3D-OCT data obtained with SS-OCT (left) [14] and SD-OCT (right) [10] are depicted in Figure 1.3.

With the near-exponential growth in computing power over the last decades, and the advent of GPU computing by means of the GPGPU paradigm, advanced volume rendering and signal-processing algorithms can be applied on large OCT data sets in real-time. In Table 1.1 a few results from the literature are summarized, highlighting the advancement in processing power using GPU solutions (adapted from [12]).

Starting from 3D-OCT data it is also possible to generate *en-face* projections of the sample at different depths, providing an invaluable tool for further analysis. A result of this technique is available in Figure 1.4, which shows a frontal view of the macula, the central part of the retina, affected by an edema.

A voxel is the primary unit of three-dimensional datasets, like the pixel is for 2D data. The word voxel originated by analogy with the word "pixel", with *vo* representing "volume" and *el* representing "element"

1.2 APPLICATIONS

1.2.1 Medicine

Ophthalmic applications have already been briefly mentioned in Section 1.1, but other areas of medicine such as Cardiology [7, 24] and Angiography [25, 39] have benefitted from the diagnostic capabilities of OCT. A comparison between OCT and Ultrasound images of a coronary plaque is available in Figure 1.5: the higher resolution of the optical system is substantial.

Angiography or arteriography is a medical imaging technique used to visualize the inside, or lumen, of blood vessels and organs of the body

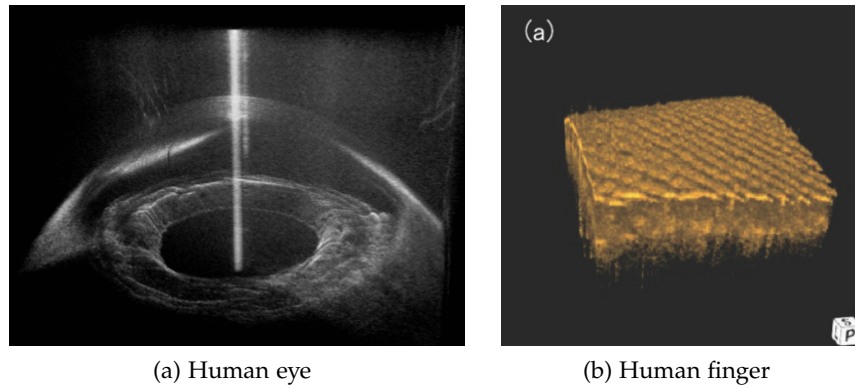


Figure 1.3: Example of 3D OCT data: human eye obtained with SS-OCT [14] (left) and human finger obtained with SD-OCT [10] (right).

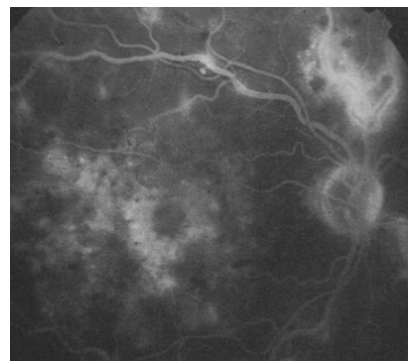


Figure 1.4: En-face view for the assessment of macular edema [32].

These applications are made possible by the small footprint of optical fibers (in the order of $200\text{ }\mu\text{m}$ of diameter) and the use of micro electro-mechanical systems (MEMS) mirrors, which can be easily embedded in endoscopes, catheters or other special probes [29, 42]. An example of a focus-adjustable probe is depicted in Figure 1.6.

Endoscopic Optical Coherence Tomography (EOCT) became an important tool for the detection of cancers affecting different parts of the human body, including bladder [46], cervix [17] and colon [22]. Other applications in the field of medicine include dermatology [21, 26] and dentistry [2, 30]. Low-delay, real-time OCT systems are also employed as a guidance tool for surgeries or tissue removal [4, 5], allowing micrometer-scale resolution and providing depth-resolved images which are unobtainable with other classical methods.

1.2.2 Industrial

OCT has also found widespread application in a variety of non-medical fields, especially where non-contact, high-precision measurements are needed. For example, real-time monitoring and thickness measurement of multi-layer structures are important tools in the manufac-

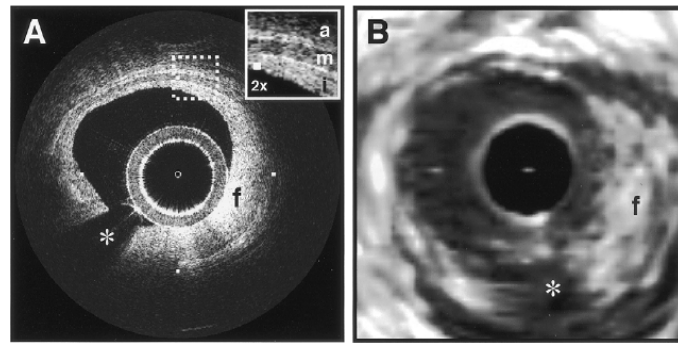


Figure 1.5: Coronary plaque imaged by OCT (left) and Intravascular Ultrasound (IVUS) (right) [24].

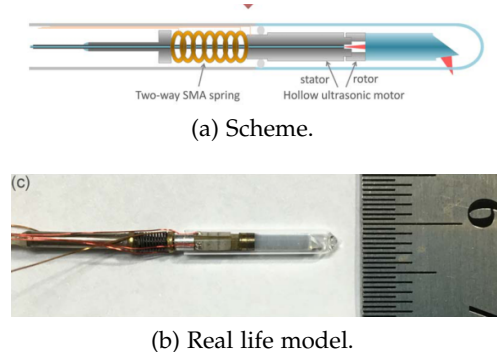


Figure 1.6: Probe for endoscopic OCT [29].

ing of microelectronics and optical devices. Industrial uses of OCT range from defect detection in ceramic and polymeric materials [40, 43] to quality evaluation of paper products [1, 34]. An interesting usage is found in [28], where the non-invasive examination of museum paintings was demonstrated, paving the way for OCT to the field of art conservation.

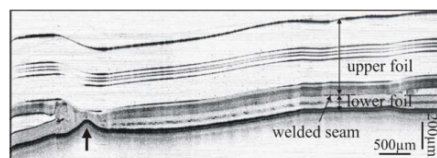


Figure 1.7: Cross-sectional OCT image of a multi-layered plastic foil used in the food packaging industry [43].

1.2.3 *In vivo monitoring of biological specimen*

We've seen that non-destructive measurements are essential in human medical diagnostic, but *in vivo* cross-sectional analysis is suited for a wide range of other biological samples. OCT has been used for growth monitoring of seeds [35], virus detection in plants [11],

and even quality assessment of egg quality in the poultry industry [36]. Alternative methods such as histology, Scanning Electron Microscope (SEM) imaging, Magnetic Resonance Imaging (MRI) and X-Ray radiography are either destructive or can not guarantee the possibility of continuous monitoring with a comparable image resolution.

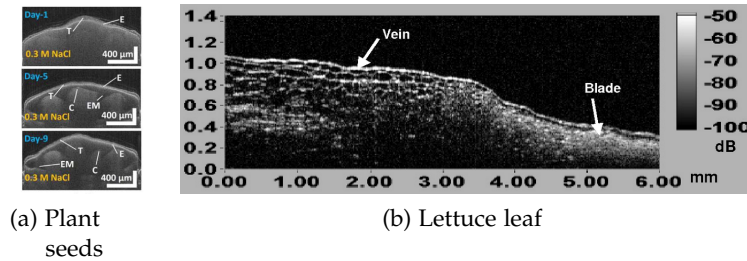


Figure 1.8: Growth monitoring of *Capsicum annuum* seeds [35] (left) and lettuce leaf [20] (right).

1.2.4 Functional imaging

Apart from the structural imaging of biological tissue, OCT can also be utilized to perform *functional* imaging, giving the user insights on the different properties of the material under analysis. PS-OCT schemes can measure properties such as birefringence, dichroism and optic axis orientation of the sample [3], while Doppler OCT (DOCT) and svOCT are able to estimate the direction and velocity of the blood flow in vessels [31]. Birefringence measurement has found use in dentistry, specifically in the monitoring of caries lesions and their progression, enabling early detection and preventing the need for surgical intervention [18].

1.3 OBJECTIVES

The study conducted in this thesis is based on a previous thesis [9] developed in the Photonic and Electromagnetic Group (PEG) Laboratory at the Department of Information Engineering (DEI) of the University of Padova. It consisted in the preliminary characterization of the main components of a high speed Swept-Source OCT (ss-OCT) system working in the 1300 nm range and the experimental determination of different parameters of the device, such as the source coherence length, the achievable scanning speed and the transversal resolution permitted by the focusing optics.

The primary objectives of this thesis are the following:

1. Designing and testing the optical circuitry needed for a stable SS-OCT system.

2. Developing a data acquisition (DAQ) application capable of continuous and low-delay video stream.
3. Control and synchronization of the Galvanometric System with the optical source and the DAQ board.
4. Acquiring cross-sectional and volumetric data of different samples.

1.4 THESIS STRUCTURE

The structure of this document is organized in the following manner:

- Chapter 2 consists of the theoretical background on the electro-magnetic phenomena of interference and temporal coherence. The basic operating principle of different OCT schemes will be thoroughly detailed.
- In Chapter 3 I will give a description of the optical and electrical devices that were used for the implementation of the final SS-OCT system. Additionally, the methods that were employed for its design and for the characterization of its performance will be reviewed.
- Chapter 4 is dedicated to a comprehensive explanation of the OCT software that was created to acquire and visualize OCT images in real-time. It will also showcase a series of cross-sectional images and basic volume renderings obtained from a variety of different samples.
- Chapter 5 concludes the thesis, illustrating possible future developments and further improvements of the presented work.

2

BASIC THEORY OF OPTICAL COHERENCE TOMOGRAPHY

In this chapter I will report the basic theoretical background needed to comprehend the working mechanisms behind the OCT technique, introduce the different schemes and compare them in terms of performance. The content of this chapter is partially adapted from [6, 33, 38].

2.1 PRINCIPLES OF COHERENCE AND INTERFERENCE

A solution to a generic electromagnetic problem is completely determined by the vector couple $\mathcal{S} = \{\mathbf{E}(\mathbf{r}, t), \mathbf{H}(\mathbf{r}, t)\}$, whose components represent the time-varying electric and magnetic field at a specific point \mathbf{r} in space. The electromagnetic field determined by \mathcal{S} is considered a valid solution if it satisfies both Maxwell's Equations and the boundary conditions specific to the problem.

For monochromatic waves, i.e. fields oscillating at a single frequency ω , we can use Steinmetz notation and write

$$\mathbf{E}(\mathbf{r}, t) = \Re[\tilde{\mathbf{E}}(\mathbf{r})e^{j\omega t}] \quad \mathbf{H}(\mathbf{r}, t) = \Re[\tilde{\mathbf{H}}(\mathbf{r})e^{j\omega t}], \quad (2.1)$$

where $\tilde{\mathbf{E}}$ and $\tilde{\mathbf{H}}$ are complex 3D vectors and $\Re[\cdot]$ is the real value operator. In a linear, homogeneous, isotropic, and current-free medium, Maxwell's equations can be written in the frequency domain in the following way

$$\nabla \times \tilde{\mathbf{E}} = -j\omega\mu\tilde{\mathbf{H}} \quad (2.2a)$$

$$\nabla \times \tilde{\mathbf{H}} = j\omega\epsilon_c\tilde{\mathbf{E}} \quad (2.2b)$$

where μ is the magnetic permeability of the medium, $\epsilon_c = \epsilon - \sigma/\omega$ is the complex dielectric permittivity and σ is the conductivity. The simplest solution of Equation 2.2 is given by the *homogeneous plane wave*. Using a cartesian coordinate system, the electric field can be expressed as

$$\tilde{\mathbf{E}}(\mathbf{r}) = \sum_{i=1}^3 A_i \cdot \hat{\mathbf{x}}_i = \sum_{i=1}^3 a_i \exp[jg_i(\mathbf{r})] \cdot \hat{\mathbf{x}}_i \quad (2.3)$$

where the amplitudes a_i are constant and $g_i(\mathbf{r}) = \mathbf{k} \cdot \mathbf{r} - \delta_i$ represent the phase functions of the electric field components. The propagation vector \mathbf{k} is given as a function of the wavelength λ as follows

$$|\mathbf{k}| = \frac{2\pi}{\lambda}, \quad (2.4)$$

while the δ_i 's are the phase differences which determine the state of polarization of the electromagnetic field. The magnetic field is instead obtained by applying Equation 2.2a to Equation 2.3.

The intensity of an electromagnetic field is given by the average amount of energy which crosses in a unit time a unit area perpendicular to the direction of the energy flow. In the case of homogenous plane waves, it is expressed as

$$I \propto \langle \mathbf{E}^2 \rangle \quad (2.5)$$

Using Equation 2.1, we can express the electric field as

$$\mathbf{E}(\mathbf{r}, t) = \frac{1}{2} [\tilde{\mathbf{E}}(\mathbf{r}) e^{-j\omega t} + \tilde{\mathbf{E}}^*(\mathbf{r}) e^{j\omega t}], \quad (2.6)$$

so that Equation 2.5 can be written as

$$\langle \mathbf{E}^2 \rangle = \frac{1}{4} \left\langle \tilde{\mathbf{E}}^2 e^{-2j\omega t} + \tilde{\mathbf{E}}^{*2} e^{2j\omega t} + 2\tilde{\mathbf{E}} \cdot \tilde{\mathbf{E}}^* \right\rangle. \quad (2.7)$$

Averaging over a time interval sufficiently larger than the period $T = 2\pi/\omega$, we obtain

$$\langle \mathbf{E}^2 \rangle = \frac{1}{2} \tilde{\mathbf{E}} \cdot \tilde{\mathbf{E}}^* = \frac{1}{2} (a_1^2 + a_2^2 + a_3^2) = \text{constant}, \quad (2.8)$$

as the high frequency terms at 2ω are canceled by the detector.

Suppose now that the field \mathbf{E} is split in two components \mathbf{E}_1 and \mathbf{E}_2 which are then superimposed in a certain point \mathbf{r}' in space, then

$$\mathbf{E}(\mathbf{r}') = \mathbf{E}_1(\mathbf{r}') + \mathbf{E}_2(\mathbf{r}'), \quad (2.9)$$

which implies that

$$\mathbf{E}^2(\mathbf{r}') = \mathbf{E}_1^2(\mathbf{r}') + \mathbf{E}_2^2(\mathbf{r}') + 2\mathbf{E}_1(\mathbf{r}') \cdot \mathbf{E}_2(\mathbf{r}') \quad (2.10)$$

The field intensity is thus

$$I = I_1 + I_2 + J_{12} = \langle \mathbf{E}_1^2 \rangle + \langle \mathbf{E}_2^2 \rangle + 2\langle \mathbf{E}_1 \cdot \mathbf{E}_2 \rangle. \quad (2.11)$$

The last term in Equation 2.11 is called *interference*. Depending on the phase difference between the two fields, the total intensity can assume different values. If the difference between the optical paths traveled by the two components is Δz , the phase difference will be $\delta = \Delta z \cdot 2\pi/\lambda$, and the interference term will be equal to

$$J_{12} = 2\langle \mathbf{E}_1 \cdot \mathbf{E}_2 \rangle = (a_1^2 + a_2^2 + a_3^2) \cos \delta. \quad (2.12)$$

In the simple case in which the two fields are linearly polarized along the x_1 direction, we have that $a_2 = a_3 = 0$, and $I_1 = I_2 = 1/2 a_1^2$, while the interference is given by $J_{12} = a_1^2 \cos \delta = 2\sqrt{I_1 I_2} \cos \delta$. The total intensity is then

$$I = I_1 + I_2 + 2\sqrt{I_1 I_2} \cos \delta = 2I_1 + 2I_1 \cos \delta \in [0, 4I_1]. \quad (2.13)$$

The intensity profile is displayed in Figure 2.1. In this first approximation of perfectly monochromatic waves there are no constraint on the phase offset δ or on the optical path difference Δz for the presence of interference.

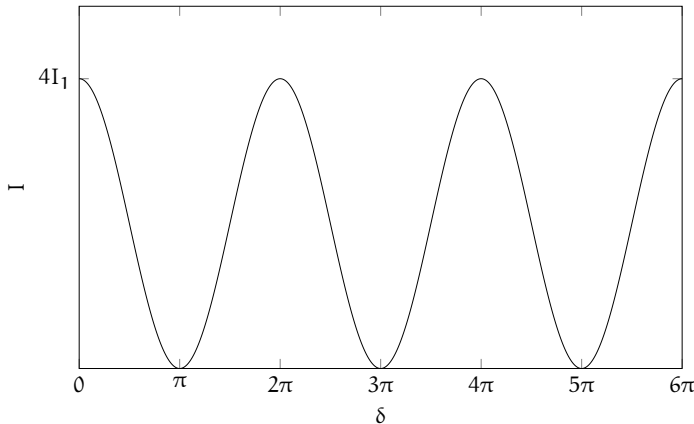


Figure 2.1: Interference fringes created by two beams of equal intensity.

2.1.1 Michelson interferometer

A classical example of the application of interference is given by the scheme called *Michelson interferometer*, whose schematic diagram is available in Figure 2.2. A light source emits an electric field \mathbf{E}_0 which is then split in two by a semitransparent mirror. The two replicas, \mathbf{E}_1 and \mathbf{E}_2 , travel along the two *arms* of the interferometer, of length l_1 and l_2 , are reflected by two mirrors and finally recombined. The intensity of the superposition of two fields is then measured by a photodetector. The two replicas arrive at the detector with a time difference given by

$$\tau = 2 \frac{l_2 - l_1}{c}, \quad (2.14)$$

where c is the speed of light in the considered medium. From Equation 2.11 we then obtain

$$I = I_1 + I_2 + 2\langle \mathbf{E}_1(t) \cdot \mathbf{E}_2(t) \rangle = 2[I_1 + \langle \mathbf{E}_1(t)\mathbf{E}_1(t-\tau) \rangle] \quad (2.15)$$

$$= 2I_1 \left\{ 1 + \cos \left[\frac{2\pi}{\lambda} 2(l_2 - l_1) \right] \right\}. \quad (2.16)$$

This type of interferometer can be used to perform high-precision measurements of distances by making one of the arms mobile and maintaining the other fixed as a reference. Counting the number of "peaks" and "valleys" of the intensity profile as the mobile arm is translated, an estimate of path length difference is given with a precision of $\lambda/2$.

2.1.2 Fringe visibility

We can define a useful parameter called *fringe visibility* as follows

$$v = \frac{I_{\max} - I_{\min}}{I_{\max} + I_{\min}}. \quad (2.17)$$

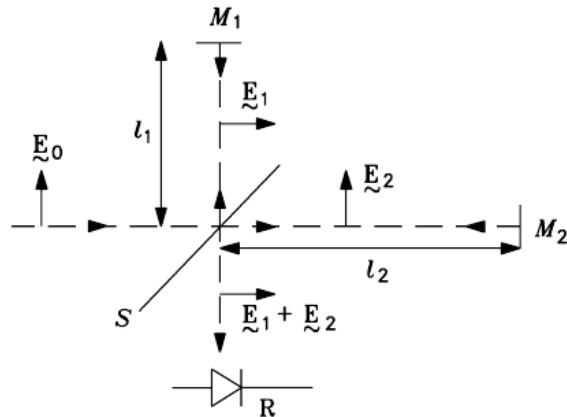


Figure 2.2: Diagram of a Michelson interferometer [38].

For a perfectly monochromatic source, v will always be constant. In particular, in the case when $I_1 = I_2$ v is equal to 1, as $I_{\min} = 0$. Real-life optical sources however will always have a bandwidth Δf greater than 0 due to random fluctuations of the electromagnetic radiation. In these cases v is a monotonically decreasing function of the time delay τ . The *coherence time* of a source is defined as the value τ_c such that $v(\tau_c) = 1/e$ (Figure 2.3).

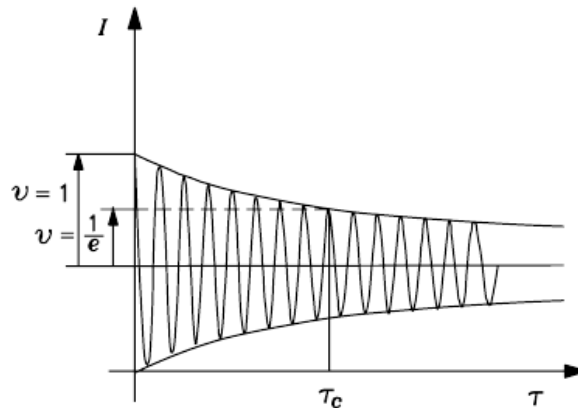


Figure 2.3: Effect of the coherence time of a source on the interference fringes at the output of a Michelson interferometer [38].

Intuitively, we may think of the coherence time as the time slot after which the optical source loses memory of what it was at the beginning. In fact, after this time slot has passed, some properties of the source randomly change due to the stochastic nature of photon emission. A perfectly coherent source emits a sinusoidal field with a well defined and constant phase relation. Similarly, two electromagnetic fields are perfectly coherent if the phase difference between the two is maintained constant for an infinite amount of time. This property is

however impossible to obtain in real life, as every source has a finite coherence time.

2.1.3 The coherence function

Another way to describe the coherence property of light other than the fringe visibility parameter, is through the so-called *mutual coherence function*. It is defined for polychromatic, i.e., non-monochromatic fields as follows [6]:

$$\Gamma_{12}(\tau) = \langle \mathbf{E}_1(t + \tau) \mathbf{E}_2^*(t) \rangle, \quad (2.18)$$

If $\mathbf{E}_1 = \mathbf{E}_2$, it is called *self-coherence function*, and it's written as $\Gamma_{11}(\tau)$. Notice that when $\tau = 0$ it reduces to the field intensity:

$$\Gamma_{ii}(0) = I_i. \quad (2.19)$$

It is then useful to apply the following normalization

$$\gamma_{ij}(\tau) = \frac{\Gamma_{ij}(\tau)}{\sqrt{\Gamma_{ii}(0)} \sqrt{\Gamma_{jj}(0)}}, \quad (2.20)$$

so that the function assumes values in the $[0, 1]$ interval. This normalized function is called *complex degree of coherence*, and it allows the following definitions:

1. Completely incoherent fields: $|\gamma_{ij}| = 0$, no interference fringes are visible.
2. Completely coherent fields: $|\gamma_{ij}| = 1$, the total intensity includes the interference term.
3. Partially coherent fields: $0 < |\gamma_{ij}| < 1$, interference fringes are present, and assume a visibility parameter equal to

$$v = \frac{2\sqrt{I_i I_j}}{I_i + I_j} |\gamma_{ij}|. \quad (2.21)$$

When the two fields have equal intensity the two parameters coincide.

Using this notation, the equation for the intensity of two partially-coherent beams is then

$$I = I_1 + I_2 + 2\sqrt{I_1 I_2} |\gamma_{12}(\tau)| \cos(\delta + \angle \gamma_{12}(\tau)) \quad (2.22)$$

where we can clearly see the effect of coherence on the shaping of the interference fringes. Using the coherence function instead of the fringe visibility as a measure of coherence, the coherence time of a

source, τ_c , is defined as the full-width half-maximum (FWHM) parameter of its self-coherence function, that is, the value of τ such that

$$|\gamma(\tau)| = \frac{|\gamma(0)|}{2}. \quad (2.23)$$

The shape of the coherence function of an optical source is completely determined by its spectrum $I(k)$ through the Wiener-Khintchine theorem, which states that the autocorrelation function and the power spectral density (PSD) of a random process are connected through their Fourier Transform.

2.1.4 Coherence length

Starting from the coherence time of the source, τ_c , we can also define its coherence length as follows

$$l_c = c_0 \tau_c, \quad (2.24)$$

where $c_0 \simeq 3 \cdot 10^8$ m/s is the speed of light in vacuum. Using a light source with a coherence length l_c in the Michelson interferometer previously presented, we would observe an interference pattern at the photoreceiver only if the difference in length of the two arms is such that

$$\Delta l = |l_2 - l_1| \leq l_c/2, \quad (2.25)$$

or, equivalently, if the total Optical Path Difference (OPD) is matched to within the coherence length of the source.

While we just defined the coherence *length* of a source, it's important to note that it is a parameter that is directly related to the time coherence and does not describe the phenomenon of spatial coherence.

2.2 OCT TERMINOLOGY

Before introducing the different OCT techniques it is useful to introduce some terminology that will be used throughout this thesis. The most basic OCT measure is called A-scan (Axial-scan), which is a signal that represents the reflectivity of a sample as a function of depth. The amount of information carried by these measurements is limited, but can be used to perform thickness measurements if the structure of the sample is known a priori.

If multiple consecutive A-scans are acquired along a transverse direction on the sample, a cross-sectional image, called B-scan, is generated. They are the most direct way to determine the anatomy of an unknown sample and are often sufficient for diagnostic purposes,

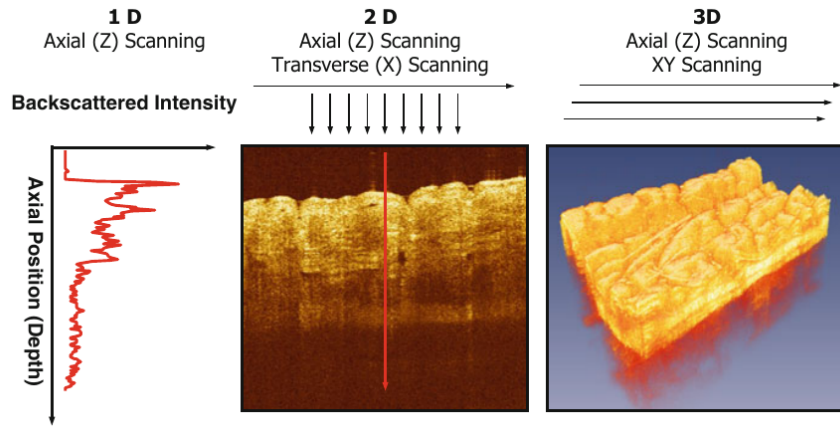


Figure 2.4: Diffent types of OCT measurements. [15]

especially in Ophthalmology. Their visualization does not require advanced techniques, but if a real-time high-resolution video stream is desired then careful design choices have to be made.

Finally, 3D volumetric data can be generated by acquiring consecutive B-scans along a second direction on the transverse plane. Intuitively, they are called C-scans. Contrary to B-scans, volume rendering requires sophisticated and efficient algorithms for a correct data interpretation and visualization [8, 16, 27]. Starting from 3D data its also possible to obtain frontal projections of the sample, called *en-face* views (Figure 2.5), or to generate cross-sections along an arbitrary plane.

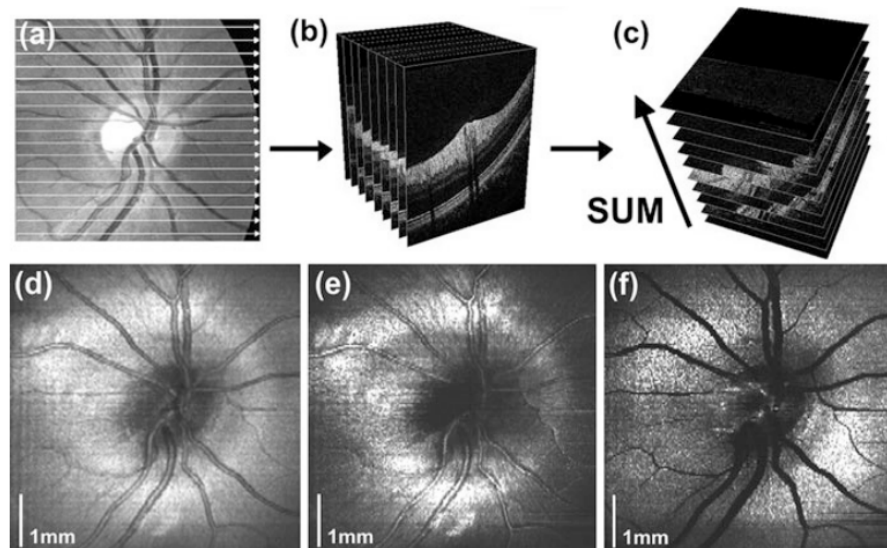


Figure 2.5: *En-face* view reconstructed from volumetric data[15]

2.3 TIME DOMAIN OCT

Time-Domain OCT (TD-OCT) is the first OCT technique that was demonstrated in the literature [23]. The basic setup is that of a Michelson Interferometer in which one of the two mirrors is translatable and the other is replaced by the sample that we wish to analyze. The two arms are called respectively *Reference arm* and *Sample arm*. As explained in Section 2.1.1, the two beams arriving at the photodetector generate interference fringes if the OPD is less than the coherence length l_c of the source. A diagram of this setup is available in Figure 2.6.

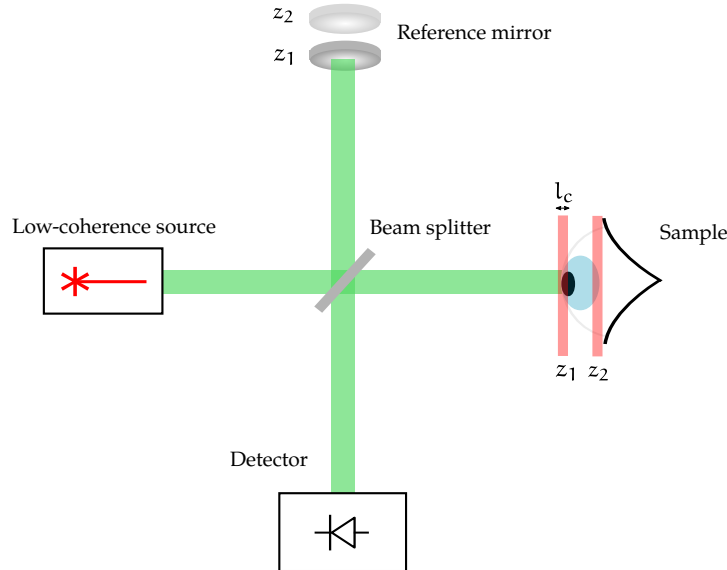


Figure 2.6: Diagram of the basic TD-OCT setup using a Michelson interferometer.

The light beam reflected by the reference mirror while in position z_1 will interfere with all the reflections occurring in the sample at depths $z \in [z_1 - l_c/2, z_1 + l_c/2]$. By measuring the intensity of the fringes it is then possible to obtain an estimate of the sample reflectivity at those depths. The whole axial measurement of the sample can be acquired by moving the translatable mirror along an adequate interval of positions. Since a single mirror position is mapped to an interval of length l_c of axial positions in the sample, the coherence length of the source can be considered to be the axial resolution of the system. As a consequence short coherence lengths are preferred, meaning that broadband sources are more widely employed.

If the light source was perfectly monochromatic, the reference signal would interfere with an infinite number of reflected replicas generated at every depth in the sample, as there would be no constraint on the OPD.

To better understand this concept, suppose that the sample is an ideal reflector with a reflection coefficient ρ_s is positioned in such a

way that the OPD is 0. The intensity measured by the detector when a OPD equal to Δz is introduced is then

$$I(\Delta z) \propto |\rho_s|^2 |E_i|^2 + |\rho_r|^2 |E_i|^2 + |\rho_s \rho_r|^2 |E_i|^2 |\gamma(\Delta z)| \cos\left(\frac{2\pi}{\lambda_0} \Delta z\right) \quad (2.26)$$

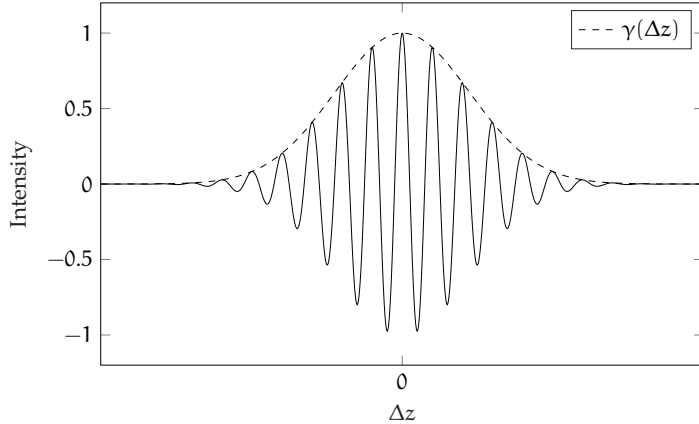


Figure 2.7: Diagram of the basic TD-OCT setup using a Michelson interferometer used in [23].

Apart from the DC offset given by the intensity of the two signals there is an oscillating term with period equal to λ_0 , which is the central wavelength of the source. Figure 2.7 illustrates the oscillating term and its envelope, which is dictated by the coherence function γ and the sample reflectivity ρ_s (set equal to 1). With a perfectly coherent source γ would be equal to 1 for all values of Δz and we would not be able to identify the reflector. On the other hand, with an increasingly sharper γ , the ideal reflector would be more and more defined.

Since the difference between the arm lengths is $\Delta l = \Delta z/2$, when scanning the reference arm, interference fringes will be generated as a function of time with periodicity equal to $(\lambda/2)/\sigma$ where σ is the mirror scanning speed.

A setup similar to Figure 2.6 can be created using fiber optics components and lenses to focus the optical beam on the sample and collect the reflections, as in Figure 2.8 [23]. The role of splitting and recombining the signals is assigned to a fiber coupler, while a piezoelectric transducer (PZT) is used to frequency-modulate the interference signal and shift it inside the photodetector's bandwidth. The generated electrical signal is then filtered, demodulated and acquired by an Analog-to-Digital Converter (ADC).

This imaging technique is also called *Optical Ranging*, and was demonstrated by Fujimoto et al.[19] in 1986. An A-scan of the cornea of a rabbit's eye was performed *in vivo*, and is available in Figure 2.9b.

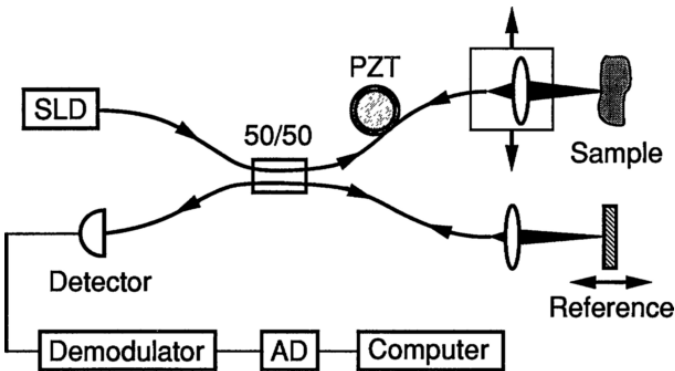


Figure 2.8: Diagram of the basic TD-OCT setup using a Michelson interferometer used in [23].

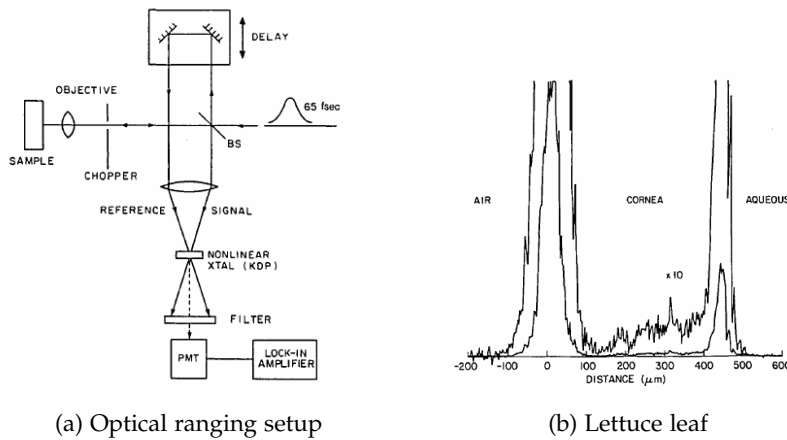


Figure 2.9: Optical ranging setup (left) and measurement (right) of the cornea of the rabbit eye [19].

The peaks in signal intensity located at $l = 0$ and $l \sim 450 \mu\text{m}$ are due to the strong reflection occurring at the interface between two different media. Inbetween these two peaks it's also possible to notice the effect of light scattered by the cornea, which is not present in the air and aqueous regions.

To acquire B-scans and C-scans, axial measurements can be repeatedly performed while moving the sample on the orthogonal plane or by deflecting the impinging optical beam by means of galvanometric mirrors.

The main disadvantage of this scheme is the slow acquisition rate, as it requires the mechanical movement of the reference arm. Consequently, *in vivo* imaging is difficult to achieve since the movement of the sample could introduce heavy distortions on both B-scans and C-scans.

2.4 FOURIER DOMAIN OCT

Fourier-Domain OCT (FD-OCT) is a group of OCT techniques that encode the depth information of a sample in the frequency content of the interference signal and decode it through a Fourier transform operation. As opposed to TD-OCT, an axial scan is obtained without the need of a scanning mirror in the reference arm. This results in a much faster acquisition speed and higher quality measurements, since the distortions caused by the mechanical vibrations and uncertainty on the position of the mirror are removed. On the other hand, FD-OCT systems require more advanced laser sources and detection schemes, other than some numerical compensation and high speed ADCs.

The two main FD-OCT schemes are called Spectral-Domain OCT (SD-OCT) and Swept-Source OCT (ss-OCT), and will be presented in the next sections.

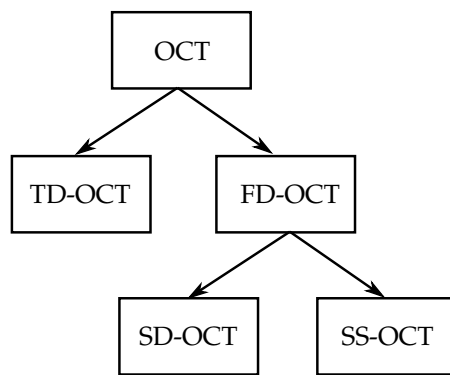


Figure 2.10: Diagram illustrating the different types of OCT modalities.

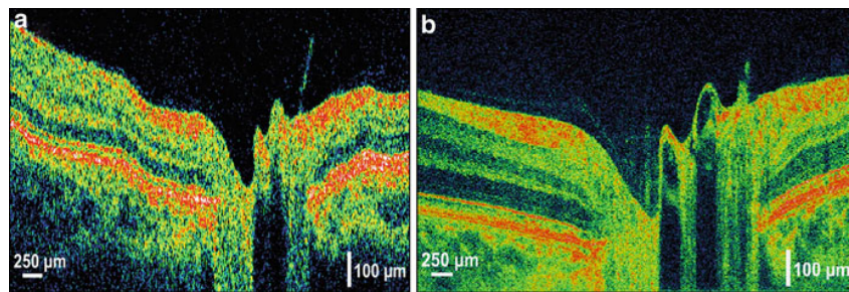


Figure 2.11: Comparison between images of the human retina obtained with standard TD-OCT (left) and high-speed, high-resolution FD-OCT (right).

2.4.1 Spectral Domain OCT

SD-OCT was the first type of FD-OCT to be implemented, and was proposed by Wojtkowski et al. in 2002 [45]. This technique uses a Superluminescent Diode (SLD) as a broadband optical source, a Michel-

son interferometer similar to that in Figure 2.6 and a detector consisting of a spectrometer. A diagram of the setup is available in Figure 2.12. As already mentioned in Section 2.4, SD-OCT can acquire an A-scan with a single optical pulse, without the need to select the imaging depth through a scanning reference mirror. This comes at the price of a more complex detection scheme and the need for computationally intensive post-processing solutions. In order to achieve real-time performances, SD-OCT schemes typically require the use of fast GPUs.

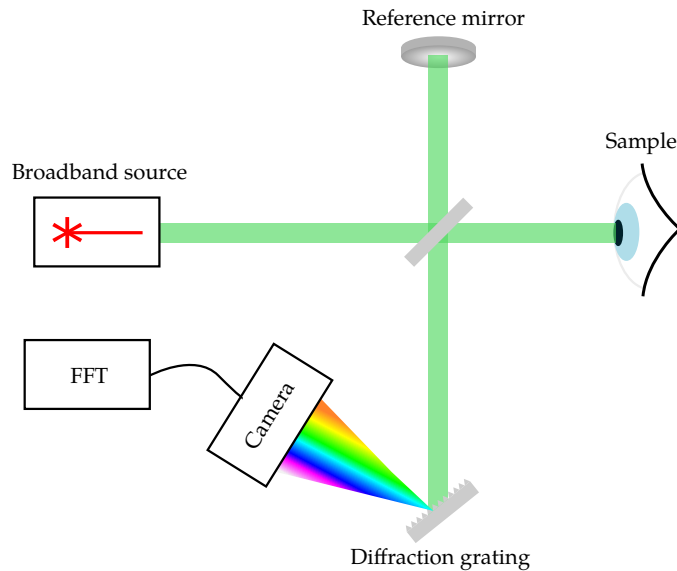


Figure 2.12: Diagram of a typical SD-OCT scheme.

To gain insight on the working principle of SD-OCT, we can rewrite Equation 2.26 as a function of the wavenumber $k = 2\pi/\lambda$ and fixing the OPD:

$$I(k) \propto I_{\text{source}}(k) \cos(k\Delta z) \quad (2.27)$$

This means that a reflector placed at a depth $d = \Delta z/2$ will frequency modulate the source spectrum with a frequency that is linearly dependant on d . This effect is illustrated in Figure 2.13 for a broadband source centered at 1310 nanometers, with ideal reflectors positioned at $d_1 = \Delta z/2 = 12.5 \mu\text{m}$ and $d_2 = \Delta z/2 = 25 \mu\text{m}$.

Using a diffraction grating or a prism, the spectrum of the interference signal is spatially separated and acquired through a linear photodetector, typically a charged coupled device (CCD) or complementary metal-oxide semiconductor (CMOS) camera. The corresponding A-scan is then computed using an inverse Fourier Transform operation, mapping modulation frequency to axial position. The depth of the various layers of the sample are encoded in the modulation frequency of the spectrum, while their reflectivity is encoded in the fringe visibility.

A key observation has to be made regarding the role of the coherence function γ . In fact, the spectrum modulation induced by a reflec-

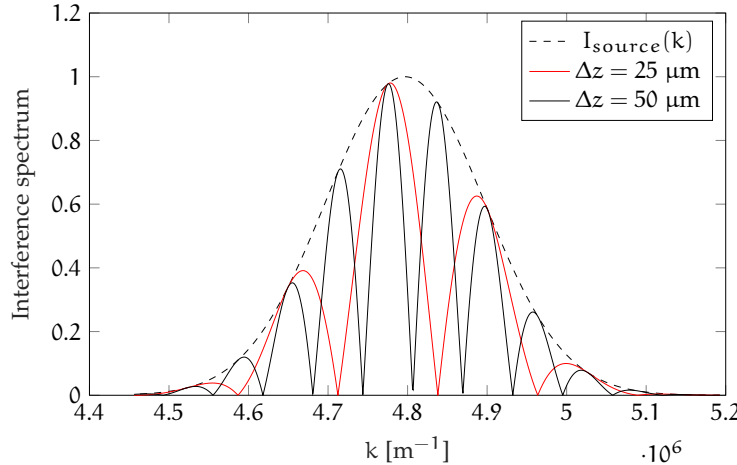


Figure 2.13: SD-OCT interference spectrum generated by two reflective surfaces.

tion at depth $d = \Delta z/2$ can only be detected if $\gamma(d/2)$ is non-zero, that is, only the portion of the sample that is within the coherence length of the source can be imaged. This is the main disadvantage compared to TD-OCT schemes, in which the depth of focus in the sample was selected with the mechanical movement of the reference mirror.

2.4.1.1 Drawbacks

SAMPLING DISTORTION One of the major problems concerning this detection technique is that the interference spectrum is usually detected linearly in the wavelength domain. For example, a diffraction grating spatially separates the different wavelengths at an angle β_m with respect to the axis normal to the grating such that

$$\sin \beta_m = m \frac{\lambda}{\Lambda} + \sin \alpha, \quad (2.28)$$

where Λ is the spacing between each line of the grating, α is the angle of the inpinging wave and m is the order of diffraction. This behaviour requires a re-sampling of the acquired spectrum before computing the Fourier Transform in order to obtain a signal which is linearly spaced in frequency instead of wavelength. If this post-processing step is ignored, an oscillating term with a fixed frequency $\propto \Delta z$ in the interference spectrum will result in a broadened peak in the Fourier domain, as can be observed in Figure 2.14. The linear sampling in the λ domain will induce a chirp on the spectrum (red). Such behaviour has a detrimental effect on the axial resolution of the system.

SENSITIVITY FALLOFF A second harmful effect on the performance of this type of FD-OCT devices is the so-called *Sensitivity falloff*. Sensitivity is defined as the signal-to-noise ratio (SNR) when the sample

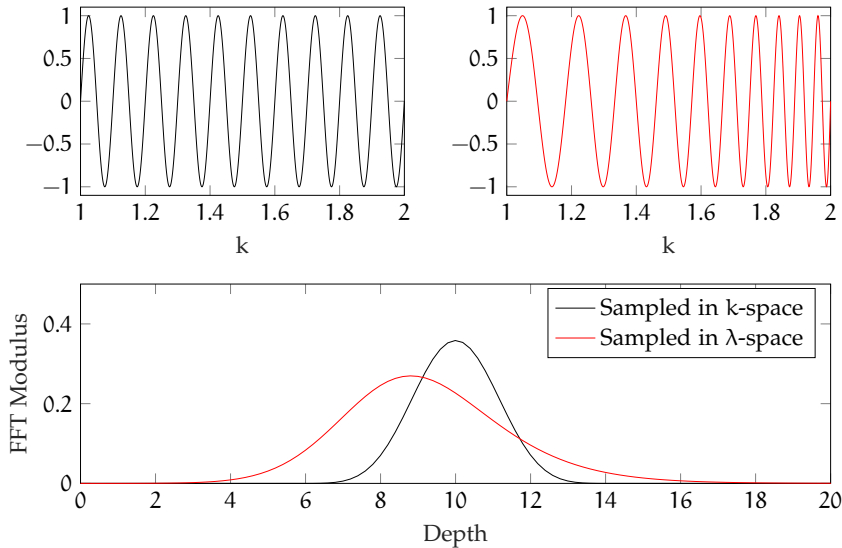


Figure 2.14: Interference distortion induced by linear sampling in the λ space.

is an ideal reflector. It's been experimentally demonstrated that for increasing imaging depths, the sensitivity value drops. Such effect is illustrated in Figure 2.15. This behaviour is due to the fact that when increasing the OPD between reference and sample arm, the coherence function $\gamma(\Delta z)$ decreases as the two reflected signals only partially overlap, resulting in a lower signal intensity.

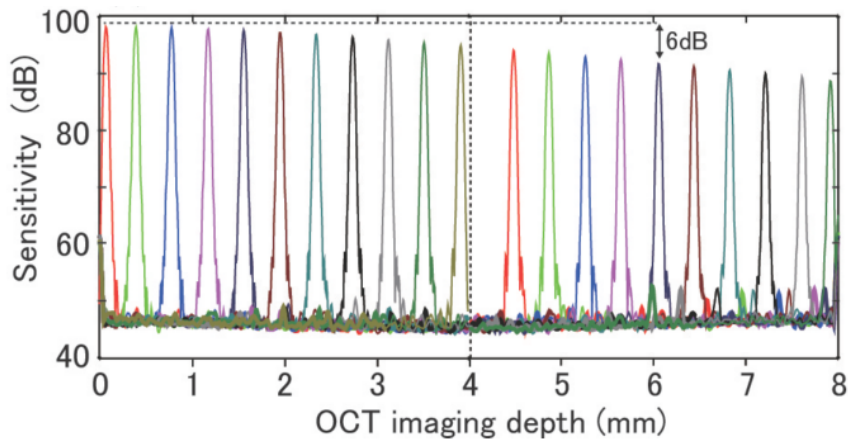


Figure 2.15: Sensitivity falloff in FD-OCT systems [10].

An additional factor that contributes to this detrimental effect is the resolution of the photodetector arrays used to acquire the interference signal. As previously explained, higher imaging depths correspond to higher spectrum modulation frequencies. If the number of pixel N of, e.g., a CCD camera is not sufficiently high, the higher frequency components will be undersampled, reducing the range of visibility. Beam diameter and camera's pixel size also influence the loss of sensitivity.

IMAGING ARTIFACTS The massive gain in acquisition rate that comes from detecting the whole imaging range in a single shot is offset by the introduction of different artifacts in the reconstructed A-scans. The interference pattern acquired by the photodetectors array comprises three terms:

1. *DC component.* All the reflected replicas of the impinging signal coming from the sample contribute to a constant DC offset in the interference signal. These are equivalent to the non-interfering terms in the Michelson interferometer formula. When Fourier-transformed, they will appear as a reflector positioned at the very start of the imaging range, where the OPD is close to zero. A simple solution to this problem is to compute and subtract the average value of the spectrum before applying the Fourier Transform.
2. *Cross-Correlation terms.* These are the interference terms that arise from the correlation between the reference signal and the reflections coming from the sample arm. As previously discussed, they contain the information required to reconstruct the reflectivity profile of the sample.
3. *Auto-Correlation terms.* They result from the interference between reflectors in the sample that are less than a coherence length apart.

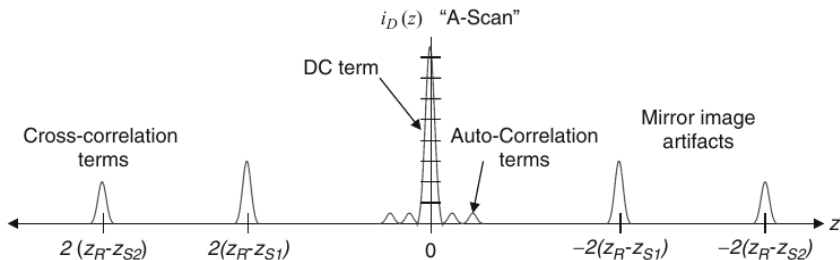


Figure 2.16: Artifacts contained in the FD-OCT A-scans[15]

These components are visible in Figure 2.16, who depicts the Fourier Transform of the interference signal generated by two reflectors. A further issue that is highlighted by this plot is the presence of the so called *complex conjugate artifacts*, or mirror image artifacts. This phenomenon arises from the Fourier Transformation of a real signal, which will have the property of Hermitian symmetry (even magnitude and odd phase). This means that FD-OCT techniques cannot differentiate between positive and negative frequencies, or equivalently, between a sample placed before or after the zero OPD position.

The easiest way to deal with this problem is to simply drop one half of the acquired A-scan, effectively halving the maximum imaging

depth of the system. Mirror artifacts will still appear in the image if the sample is too close to the scanning lens and crosses the zero OPD position, which is fixed by the reference mirror. The part of the sample which is in the "negative" OPD range will appear flipped and superimposed to the other part of the sample. This effect is illustrated in Figure 2.17, in which the scanning lens is progressively moved forward, closer to the patient's retina.

Different methods to solve this issue and restore the full imaging range have been proposed, including complex-signal detection schemes using 3×3 fiber couplers [37], heterodyne detection [13] and phase-shifting techniques [41] using either PZTs or electro-optic modulators (EOMs).

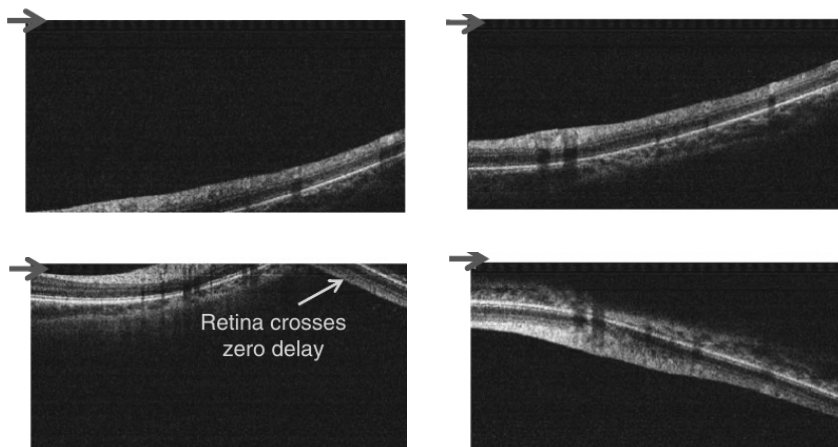


Figure 2.17: Complex conjugate artifacts in SD-OCT.

2.4.2 Swept-Source OCT

Swept-Source OCT (ss-OCT), also known as optical frequency domain interferometry (OFDI), is a FD-OCT technique that employs a narrow-bandwidth frequency-swept laser as an optical source. The introduction of tunable sources simplifies the detection scheme, removing the need for diffraction gratings and photodetector arrays. Ideally, a swept-source laser for SS-OCT should present a frequency sweep that is linear, i.e., the instantaneous optical frequency should be expressed as

$$f(t) = f_0 + \sigma_f \cdot t, \quad (2.29)$$

where σ_f , typically measured in Terahertz per microsecond, is the sweep speed of the source. If this requirement is satisfied, the intensity at the output of the interferometer when the sample is a single reflector positioned at the depth $d = \Delta z/2$, can be expressed as

$$I(t) = I_1 + I_2 + 2\sqrt{I_1 I_2} \cos(2\pi\Delta ft) \quad (2.30)$$

where

$$\Delta f = \sigma_f \cdot \Delta t = \sigma_f \cdot \frac{\Delta z}{c} = \sigma_f \cdot \frac{d}{2c}, \quad (2.31)$$

called the *beat frequency*, is linearly dependant on the depth of the reflector. When the reflector is replaced by a real sample, multiple beat frequencies arise in the photodetector's current and the reflectivity profile can be reconstructed with a Fourier Transform. This technique is equivalent to SD-OCT, with the key difference that the frequency sweep enables the detection as a function of time through a simple photodetector, while the diffraction grating spatially separates the different wavelengths and directs over a photodetector array.

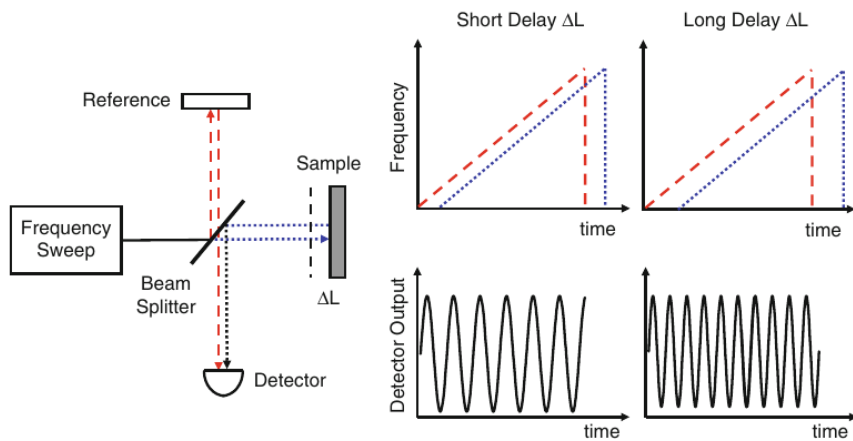


Figure 2.18: Diagram of a typical SS-OCT scheme [15]

2.4.2.1 Sweep nonlinearity

A tunable laser generally consists of a gain medium, typically a semiconductor optical amplifier (SOA), a tunable wavelength filter and a laser cavity that supports a large bandwidth. The frequency-sweep is achieved by controlling the tunable filter through electrical signals to select the desired wavelength. Figure 2.19 shows the diagram of an Axsun swept source in which frequency tuning is achieved by tilting a MEMS mirror at the end of a Fabry-Perot filter. Rapidly changing the selected wavelength can affect the linearity frequency sweep, contributing to a nonlinear term in Equation 2.29, which then becomes

$$f(t) = f_0 + \sigma_f \cdot t + \eta(t), \quad (2.32)$$

where $\eta(t)$ contains the aforementioned nonlinearities. If the detector's output is digitized with a uniform clock rate, a similar effect to that described for SD-OCT systems can arise (Figure 2.14), resulting in a non-linear sampling in the k-space. Consequently, distortions in the acquired A-scans can appear, hindering the image quality. A resampling of the acquired signal is then required in order to linearize the

frequency sweep, adding to the total computational cost and possibly reducing the acquisition rate of the system.

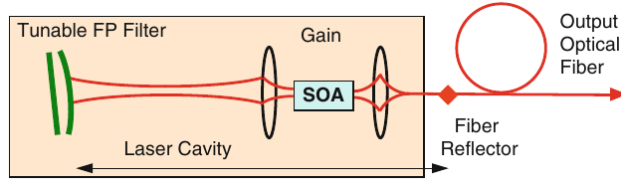


Figure 2.19: Frequency-swept optical source by Axsun [15].

2.4.2.2 *k-clocking*

While in SD-OCT the resampling step is the only possible solution for this issue, SS-OCT enables a hardware approach through a non-uniform clocking of the DAQ device. This is accomplished by extracting a clock signal, called *k-clock*, by means of an unbalanced Mach-Zender interferometer (MZI) which detects the frequency-sweep and generates a sinusoidal signal with a variable frequency. This approach removes the need for the computationally-intensive resampling step, but requires special DAQ devices that can handle external clocks with a wide range of frequencies and duty cycles.

2.4.2.3 *Acquisition rate*

The acquisition speed of SS-OCT systems is dictated by the source sweep repetition rate, that is, the frequency at which the source is able to sweep the entire bandwidth. This parameter is determined by the laser cavity length. In fact, for a given frequency, the spontaneous emission has to build up in order to reach a saturation limit to be correctly amplified by the active region. Shorter cavities with a smaller round-trip generally guarantee higher repetition rates than longer cavities. Novel swept-source designs enable acquisition speeds in the order of 100,000 A-scans per second, with Fourier domain mode locking (FDML) and vertical cavity surface-emitting lasers (VCSELs) reaching repetition rates above 500 kHz. These unprecedented values make SS-OCT the primary candidate for real-time 3D visualization of *in vivo* samples, where motion artifacts could hinder image quality. This is possible because the detection scheme is no longer the bottleneck like in SD-OCT, where slow camera response times limited the overall rate of the system.

2.4.2.4 *Axial resolution*

Just like in the case of SD-OCT, the axial resolution depends on the tuning range of the source, $\Delta\lambda$, which is defined as the FWHM of the spectrum. In the case of a Gaussian spectrum, the axial resolution,

defined as the FWHM of the reflection peak generated by a perfect reflector, is given by

$$\delta z \simeq 0.75 \cdot \frac{\lambda_0^2}{\Delta\lambda}, \quad (2.33)$$

where λ_0 is the central wavelength of operation, which is chosen based on the application (1060 nm for Ophthalmology, 1300 nm for tissue imaging).

2.4.2.5 Imaging range

Imaging range of SS-OCT systems is, like other FD-OCT schemes, limited by the coherence length of the source, which we have previously defined as the OPD at which the visibility of the interference fringes drops to half of its maximum. This parameter is controlled by the instantaneous linewidth of the source $\delta\lambda$ by the following equation:

$$l_c \approx 0.44 \frac{\lambda_0^2}{\delta\lambda}. \quad (2.34)$$

As with SD-OCT, complex conjugate artifacts typically limit the imaging range to be half of the coherence length.

When using a k-clock to acquire A-scans, the imaging range is also dependant on the path difference of the MZI's arms, which has to be 4 times the maximum imaging depth, d_{max} . A factor of 2 is needed because a reflector positioned at d_{max} will have OPD equal to $\Delta z = 2d_{max}$ with respect to the reference mirror. The other factor of 2 is needed to satisfy Nyquist's criterion, so that the k-clock will have a maximum frequency that is 2 times the beat frequency generated by the reflector at d_{max} .

2.4.2.6 Balanced detection

The use of simple photodetectors instead of more complex setups involving diffraction gratings and prisms allows for a dual balanced detection scheme. By collecting the reference and sample signals through a circulator and feeding them to a 3 dB fiber coupler, two interference signals can be obtained. A balanced detector can then subtract the common DC component and excess noise, while at the same time summing the interference term. This detection scheme has been proved to be more efficient than a simple Michelson interferometer. A complete SS-OCT scheme with dual balanced detection and external k-clock is illustrated in Figure 2.20.

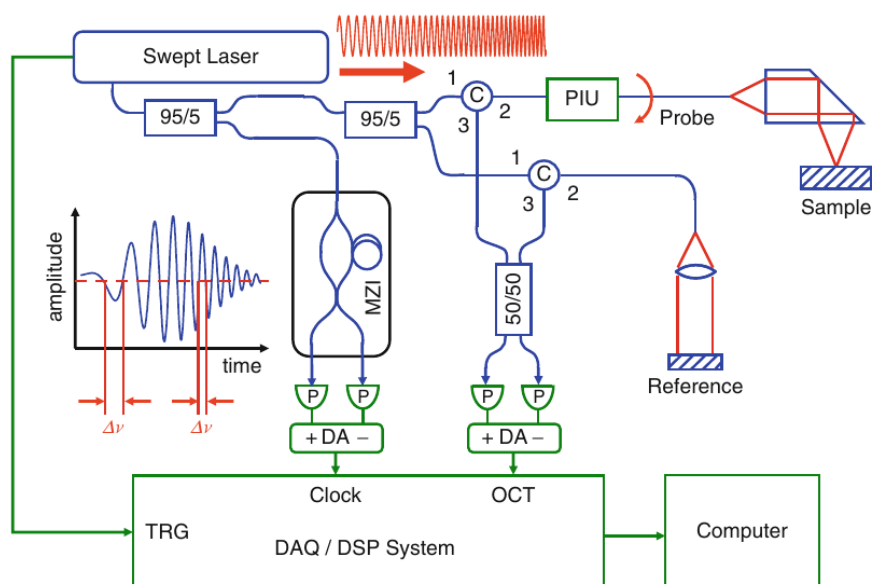


Figure 2.20: Complete fiber optic SS-OCT scheme using an external clock source and balanced detection [15].

DESCRIPTION OF THE SETUP

This chapter details the setup that was used in the design of a Swept Source OCT system developed for this thesis work, describing the optical and electrical components that were employed, and assessing their performance.

Additionally, two different fiber optic interferometer schemes are tested in order to obtain a working OCT device.

3.1 OPTICAL SOURCE

As already discussed in Chapter 2, SS-OCT systems employ a narrow-bandwidth tunable laser to enable a simple detection scheme. It is one of the most critical components of the entire system, as several parameters such as axial resolution and imaging depth are directly related to its characteristics. The source that was used in this thesis is a SSOCT-1310 by Axsun Technologies, which is a class 3 laser that uses a MEMS tunable filter to sweep wavelengths in the 1300 nm range.

The two most important features of this laser are the fast sweep rate, which enables high speed imaging, and the presence of the k-clock signal used in the equalization of the nonlinear frequency sweep. An photo of the device is available in Figure 3.1.



Figure 3.1: The Axsun SSOCT-1310 swept source.

3.1.1 *Optical Spectrum*

A critical parameter in swept sources for OCT applications is the wavelength interval over which the laser is able to tune. From Ta-

PARAMETER	UNITS	VALUE
Sweep Rate	kHz	100.2
Center Wavelength	nm	1305
Wavelength Tuning Range	nm	140.38
Average Power	mW	25.7
Duty Cycle	%	77.3
Sampled Duty Cycle	%	50.5
External Clock Min Frequency	MHz	183.1
External Clock Average Frequency	MHz	307.0
External Clock Max Frequency	MHz	332.1
Sampling Clocks	-	1536

Table 3.1: Axsun laser datasheet.

ble 3.1, we can see that the Axsun SSOCT-1310 is centered at $\lambda_0 = 1305$ nm with a bandwidth of $\Delta\lambda = 140.38$ nm. These values were verified by connecting the laser output directly to an Optical Spectrum Analyzer (OSA), measuring its spectrum.

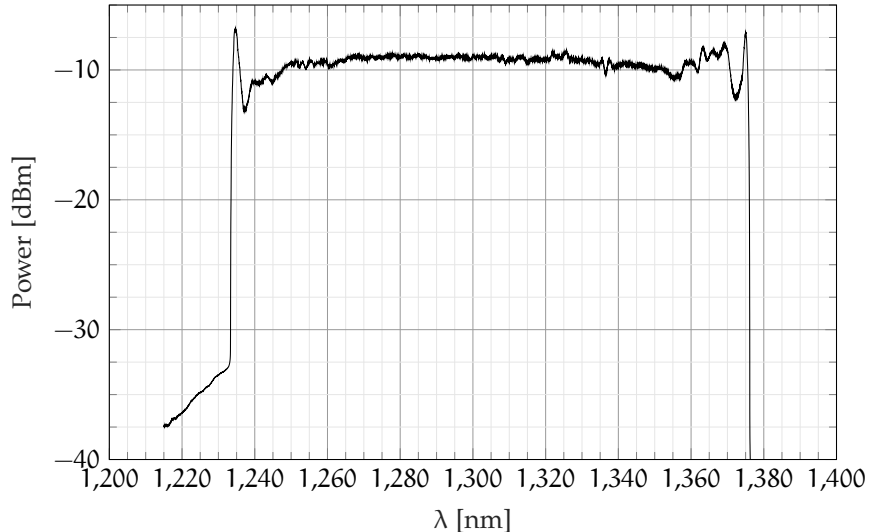


Figure 3.2: Spectrum of the Axsun SSOCT-1310 laser, obtained with a 1 nm resolution.

The measurement was performed with a resolution of 1 nanometer, resulting in the spectrum visible in Figure 3.2. The edge wavelengths turned out to be $\lambda_1 \approx 1237$ nm and $\lambda_2 \approx 1376$ nm, which result in a bandwidth of $\Delta\lambda \approx 139$ nm and central wavelength of $\lambda_0 \approx 1307$ nm. These values slightly differ from those reported in the datasheet, but not enough to compromise the performance of the laser.

The bandwidth is swept at a frequency $f_a = 100.2$ kHz and with a duty cycle $d_c = 0.505$, meaning that the average wavelength sweep speed is

$$\sigma_\lambda = \frac{\Delta\lambda f_c}{d_c} \approx 27.8 \text{ nm}/\mu\text{s}. \quad (3.1)$$

Since the goal of SS-OCT sources is to perform a linear frequency sweep, it is more useful to define this parameter in the following manner

$$\sigma_f = c_0 \left(\frac{1}{\lambda_0 - \Delta\lambda/2} - \frac{1}{\lambda_0 + \Delta\lambda/2} \right) \frac{f_a}{d_c} \approx 4.9 \text{ THz}/\mu\text{s} \quad (3.2)$$

The instantaneous frequency, after linearization, is thus expressed by

$$f(t) = f_0 + \sigma_f t \quad (3.3)$$

where the starting frequency is determined by

$$f_0 = \frac{c_0}{\lambda_0 + \Delta\lambda/2} \approx 218.2 \text{ THz}. \quad (3.4)$$

3.1.2 Axial Resolution

Using Equation 2.33 and the data provided by Table 3.1 it is possible to obtain an estimate of the axial resolution provided by the employed optical source. The axial resolution is found to be

$$\delta z \simeq 0.75 \frac{\lambda_0^2}{\Delta\lambda} \approx 9.2 \text{ }\mu\text{m}. \quad (3.5)$$

This approximation is valid for sources with a Gaussian spectrum, and can lead to an overestimation of the real axial resolution of the system in case this condition is not met.

3.1.3 Sweep trigger

The Axsun laser provides a square-wave signal that determines the start of the frequency sweep and that is used to trigger the acquisition of A-scans. This signal is acquired with a high-speed oscilloscope and illustrated in Figure 3.3. The voltage range was measured as $V_{range} \approx [0, 1.48]$ V, while the duty cycle is found to be

$$d_c = \frac{t_{high}}{t_{high} + t_{low}} \approx 0.97. \quad (3.6)$$

For a correct acquisition of A-scans, the datasheet recommends to trigger the acquisition device when the signal level reaches the value of $V_{trig} = 0.71$ V, pictured in Figure 3.3 with a dashed line.

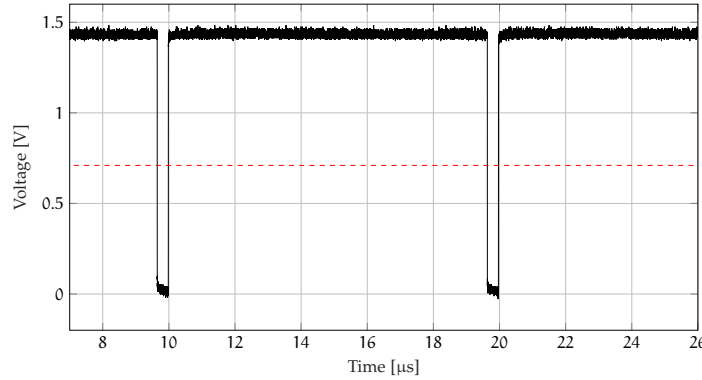


Figure 3.3: Sweep trigger of the SSOCT-1310 laser.

3.1.4 Power profile

Using a photodiode it's possible to measure the instantaneous power profile of the laser emission. The photodiode generates an electrical current which is proportional to the power of the detected electromagnetic field:

$$I_{ph} = \mathcal{R} \cdot P \quad (3.7)$$

The constant \mathcal{R} is called *responsivity* [A/W] and is specific to the detector used. The current can then be measured with an oscilloscope. In order to avoid the saturation of the receiver, a 3 dB coupler was inserted between the source and the photodiode. The obtained power profile is depicted in Figure 3.4 along with the sweep trigger. We can observe that in the first $\sim 5 \mu\text{s}$ after the positive edge of the trigger, the instantaneous power behaves like a typical laser pulse while outside of this interval it assumes an irregular profile.

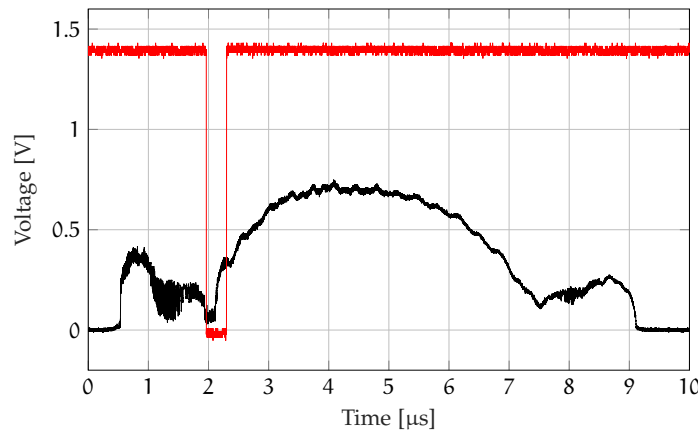


Figure 3.4: Power profile of the SSOCT-1310 laser.

3.1.5 *k-clock*

As already stated, this particular SS-OCT laser is equipped with an internal MZI which generates the variable-frequency clock, called *k-clock*, used to sample the A-scan signal at a variable rate and equalize the nonlinear terms in the frequency sweep. As we can see in Figure 3.5, this signal assumes values in the [0, 900] mV range with an average value of about 460 mV. This sinusoidal signal will be used to drive the acquisition board for the first 5 μ seconds of the sweep and from this point forward will be referred to as *useful clock*. As per Table 3.1, the total number of samples that can be acquired using this clock is $N_s = 1536$. In the last 5 μ seconds the clock is called "dummy" because of its undefined behaviour that could lead to issues in the clocking of the DAQ devices.

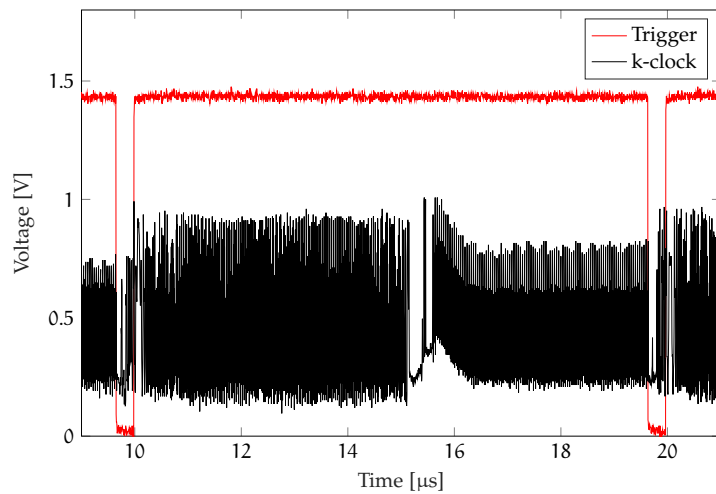


Figure 3.5: Estimate of the instantaneous frequency of the *k-clock*.

In Figure 3.6 are depicted two 50 nanoseconds windows at the start (left) and in the middle (right) of the useful clock, where the variable frequency of signal is clearly visible. Also worth noting is that at the start of the sweep the signal appears much more distorted than in the middle of the sweep. Fortunately, this behaviour did not compromise the performance of the system.

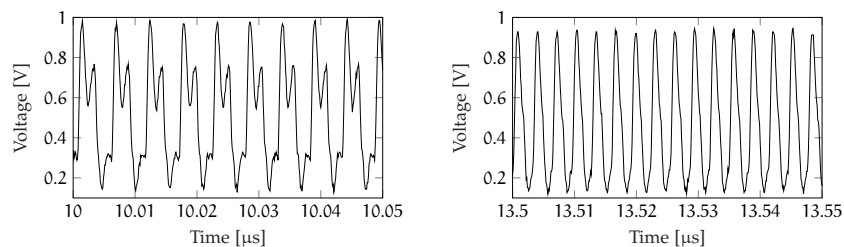


Figure 3.6: Behaviour of the useful *k-clock* at different time instants.

To gain further insights on the nature of the frequency sweep, it is interesting to estimate the instantaneous frequency of the k-clock. A method to perform this estimate is the following

1. Subtract the average value from the signal
2. Interpolate the signal (t, y) to obtain (\hat{t}, \hat{y})
3. Determine the time instants \hat{t}_i at which the signal \hat{y} crosses 0, from which a vector $\mathcal{I} = [\hat{t}_{i_1}, \hat{t}_{i_2}, \dots, \hat{t}_{i_N}]$ is built.
4. Compute the difference between the adjacent elements of \mathcal{I} and obtain $\mathcal{T} = [\hat{t}_{i_1}, \hat{t}_{i_2}, \dots, \hat{t}_{i_{N-1}}]$,
5. The instantaneous frequency of the signal is then estimated as $\hat{f}_i = 1/2\hat{t}_i$.

The result of this method is illustrated in Figure 3.7. Since the estimate is rather noisy, a low pass filter was applied to the \hat{f}_i signal, resulting in a much cleaner estimation (depicted in red). As we can observe, the instantaneous frequency rapidly changes at the start and at the end of the sweep, while in the middle it stabilizes at about 320 MHz. Since a constant k-clock frequency implies a linear frequency sweep, we can infer that the sweep nonlinearities are much more prevalent at the edge of the sampling interval.

The maximum estimated frequency is $\hat{f}_{clk}^{\max} = 339$ MHz, as opposed to the value that was reported in Table 3.1 of $f_{clk}^{\max} = 332.2$ MHz. This slight overestimation is also visible in Figure 3.7, where we can see that the low-pass filtered signal is slightly higher than the average value of the non filtered one.

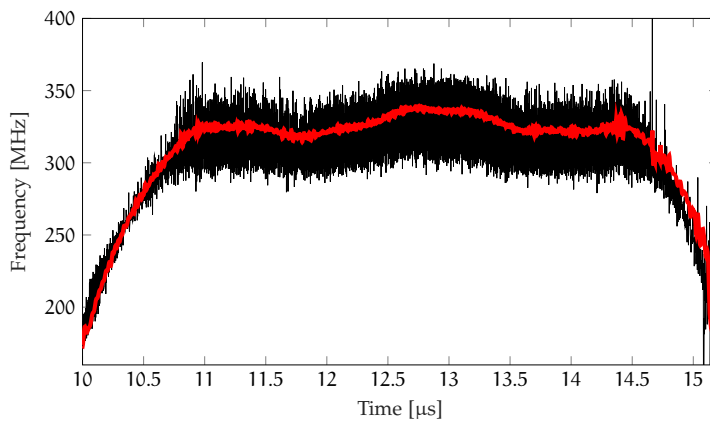


Figure 3.7: Estimate of the instantaneous frequency of the k-clock.

From the maximum frequency of the k-clock signal we can measure the maximum imaging depth obtainable by the system.

Two replicas of the pulse overlapping with a relative time delay τ will generate a beat frequency f_b given by

$$f_b = \sigma_f \tau \quad (3.8)$$

where σ_f , the sweep speed, was determined in Equation 3.2. In a OCT setup, the time delay τ is related to the path mismatch of reference and sample arm, which in turn depends on the depth of the layer of the sample that generates the reflection. In this way

$$\tau = \frac{2dn}{c_0}, \quad (3.9)$$

where c_0 is the speed of light in vacuum, n is the refractive index of the sample and d is the depth. By the Nyquist theorem, the maximum beat frequency that can be digitized using the k-clock is

$$f_b^{\max} = \frac{f_{\text{clk}}^{\max}}{2}, \quad (3.10)$$

which results in a maximum depth in air ($n = 1$) of

$$d_{\max} = \frac{c_0 f_b^{\max}}{2\sigma_f} = \frac{c_0 f_{\text{clk}}^{\max}}{4\sigma_f} \simeq 5.1 \text{ mm}. \quad (3.11)$$

3.1.6 Coherence length

In Chapter 2 we have seen that the coherence length of a source is one of the most important parameters of optical sources, independently of the type of OCT system. In TD-OCT, this parameter determines the axial resolution of the system, while FD-OCT schemes it also affects the imaging range, as the reference arm is fixed. For this reason, the coherence length of a swept source has to satisfy the following inequality

$$l_c \geq 2 \cdot d_{\max}, \quad (3.12)$$

where the factor 2 accounts for the total round-trip time. This implies that the coherence length of the SSOCT-1310 source is at least

$$l_c \geq 10.2 \text{ mm}. \quad (3.13)$$

The exact value was experimentally determined in [9], measuring the normalized coherence function $|\gamma(\Delta z)|$ by placing a mirror in the sample arm and acquiring the interference signal for different values of OPD. The path length difference was changed by moving the reference mirror mounted on a translatable structure. The intensity of the interference signal, normalized by its maximum value, is plotted in

Figure 3.8 as a function of the OPD. When the OPD increases above a certain value, the coherence function decays exponentially as

$$|\gamma(\Delta z)| \propto e^{-\alpha|\Delta z|}, \quad (3.14)$$

which corresponds to a linear decay in the logarithmic domain. The parameter α was estimated by fitting a line to the data points using a Linear Least Squares fit. The coherence length is finally determined as the value Δz such that $|\gamma(\Delta z)| = 1/2$, resulting in

$$l_c = 2 \cdot \frac{\ln 2}{\alpha} \approx 12.3 \text{ mm.} \quad (3.15)$$

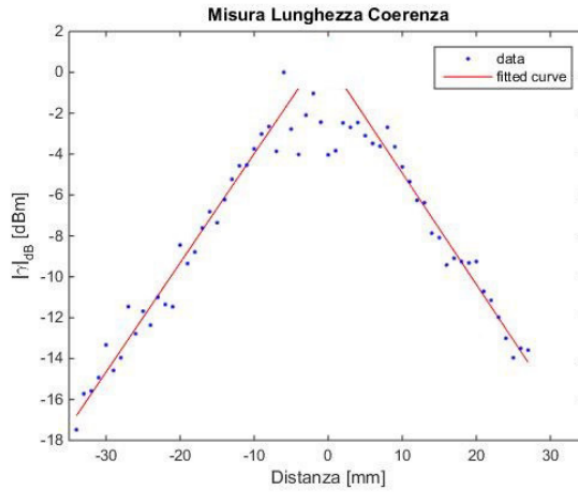


Figure 3.8: Experimental estimation of the normalized coherence function.

3.2 SCANNING SYSTEM

One of the most critical components of an OCT is the scanning system. Its role is to receive the light emitted by the source, focus it on a specific position on the sample under test, and collect the backreflections. A scanning system usually comprises of three different devices

1. Fiber collimator
2. Galvanometric Mirrors
3. Focusing lens

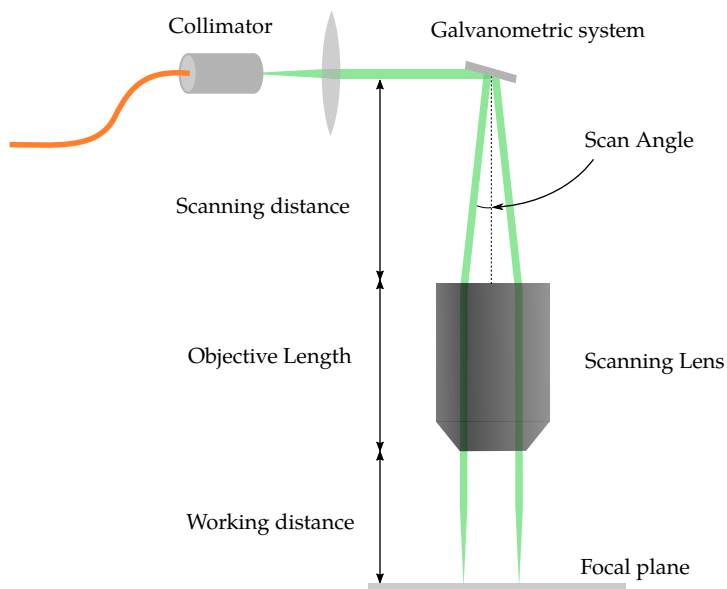


Figure 3.9: Diagram of a OCT scanning system.

A schematic of this system is depicted in Figure 3.9. Light coming from a single mode optical fiber is deflected by a system of galvanometric mirrors towards a lens which in turns focuses the radiation on the sample. By rotating the mirrors the light beam is focused on a different position on the sample. The reflected beam travels the same path in the opposite direction and is collected by the optical fiber. The correct design of these components is paramount in order to guarantee an optimal transversal resolutions and avoid focusing errors or other distortions.

3.2.1 Collimator

The role of the fiber collimator is to collect light coming from a single mode fiber and collimate the beam on the galvanometric mirrors. The divergence angle at the output of the collimator is approximated with

the following equation when the beams have a Gaussian intensity profile:

$$\theta \approx \frac{D}{f} \frac{180}{\pi}, \quad (3.16)$$

where D is the mode diameter and f is the focal length of the collimator. This approximation works well for single mode fibers, but will underestimate the real divergence angle in the case of multimode fibers, as the intensity profile has a non-Gaussian shape.

The collimator used in this setup is the Thorlabs F280APC-C¹, which is designed to work in the 1310 nm range. Its main specifications are summarized in Table 3.2.

PARAMETER	UNITS	VALUE
Central wavelength	nm	1310
Beam diameter	mm	3.4
Divergence angle	degrees	0.028
Lens numerical aperture (NA)	-	0.15
Focal length	mm	18.67

Table 3.2: Thorlabs F280APC-C datasheet.

3.2.2 Scanning lens

The light beam deviated by the galvanometric mirrors has to be focused on the sample under test in order to guarantee high resolution images. This is accomplished by a telecentric scanning lens. This type of lenses is characterized by flat image planes which are ideal for OCT applications.

The main parameters that characterize this device are the following:

- Entrance Pupil Size (EP): it specifies the diameter of the collimated laser beam that will maximize the resolution of the imaging system. When using a single galvanometric mirror, the EP is located at the pivot point of the mirror. When two mirrors are used, the EP is located between the two mirrors.
- Scanning Distance (SD): the distance between the EP and the base of the lens.
- Scan Angle (SA): the angle between the incoming light beam and the optical axis of the lens.

¹ <https://www.thorlabs.com/thorproduct.cfm?partnumber=F280APC-C>

- Working Distance (WD): the distance between the tip of the lens and the focal plane.
- Parfocal Distance (PD): the distance between the base of the lens and the focal plane. It is equal to the WD plus the objective length.
- Field of View (FOV): the area on the focal plane that can be imaged with a resolution equal or better than the one guaranteed by the lens.
- Depth of View (DOV): it corresponds to the distance between parallel planes on either side of the focal plane, where the beam spot diameter is $\sqrt{2}$ greater than it is at the focal plane. Using lenses with a high DOV value yields images with high lateral resolution in a larger interval of depths.
- Spot size: the diameter of the beam on the focal plane.

The lens used for the SS-OCT system developed in this thesis is the Thorlabs LSM04². Its main specifications are listed in Table 3.3. A simulation of the beam spot size on the focal plane is available in Figure 3.10, where we can see that it increases for bigger scan angles. This behaviour has the effect of reducing the lateral resolution at the edge of the FOV.

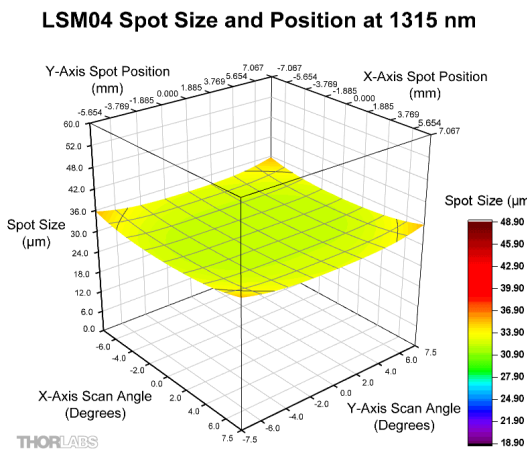


Figure 3.10: Simulation of the spot size at different scan angles.

3.2.2.1 Lateral resolution

Using the parameters listed in Table 3.3 it is also possible to obtain an estimate of the lateral resolution of the system, which is dictated

² <https://www.thorlabs.com/thorproduct.cfm?partnumber=LSM04>

PARAMETER	UNITS	VALUE
Wavelength range	nm	1250-1380
Effective Focal Length (EFL)	mm	54
Entrance Pupil size	mm	4
Working Distance	mm	42.3
Parfocal Distance	mm	80.8
Scan Distance	mm	18.9
Maximum Scan Angle	degrees	$\pm 7.5 \times \pm 7.5$
Field of View	mm ²	14.1 × 14.1
Depth of View	mm	0.61

Table 3.3: Thorlabs LSMo4 datasheet.

by the diffraction limited spot size of the focused optical beam. For Gaussian-shaped beams, it is approximated as [15]

$$\delta x \approx \frac{4\lambda_0}{\pi} \frac{f}{d} \quad (3.17)$$

where λ_0 is the central wavelength of operation, f is the focal length of the lens and d is the diameter of the beam at the entrance of the lens. The lateral resolution guaranteed by the LSMo4 is thus

$$\delta x \approx \frac{4\lambda_0}{\pi} \frac{\text{EFL}}{\text{EP}} \approx 22.5 \text{ } \mu\text{m}. \quad (3.18)$$

Since the diameter of the beam exiting the fiber collimator is slightly smaller ($d = 3.4$ mm) than the EP size, the resulting lateral resolution becomes

$$\delta x \approx 26.5 \text{ } \mu\text{m}. \quad (3.19)$$

The depth of view, also called confocal parameter, limits the imaging depth of the system. Due to diffraction, this parameter is also governed by the lateral resolution of the system through the following equation

$$b = \frac{2\delta x^2}{\lambda_0}. \quad (3.20)$$

This effect is illustrated in Figure 3.11, where we can see that using lenses with a high numerical aperture (NA), or small spot size, the depth of view is reduced. In OCT systems it is preferred to use low NA lenses to sacrifice lateral resolution in favor of a depth of view comparable to the coherence length of the source. Following this criterion the coherence length is fully exploited.

Using the EP size when calculating δx , the confocal parameter is $b \approx 0.61$ mm, equal to the value reported in Table 3.3, while using the beam size diameter $d = 3.4$ mm it becomes $b \approx 0.84$ mm.

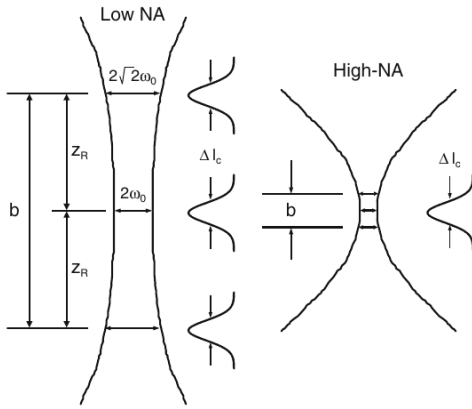


Figure 3.11: Effect of the scanning lens' numerical aperture on spot size and depth of view.

3.2.3 Galvanometric Mirrors

In order to acquire B-scans and C-scans it is necessary to direct the laser beam emitted from the swept laser over a specified area of the sample. This is accomplished by using a system of *galvanometric mirrors*, also called *galvo mirrors*. A cross-sectional image can be generated with a single 1D mirror, that is, a mirror which can rotate on a single axis, while volumetric data require the use of either a 2D mirror or a couple of 1D mirrors. In the second case, each mirror is responsible for the movement of the beam over a single direction on the focal plane, typically called X and Y.



Figure 3.12: The Thorlabs GVS002 galvo system.

The galvo system employed in this thesis work is the Thorlabs GVS002³, which consists in two 1D silver plated mirrors, the motors that drive them, a detector to measure the mirrors' position and the servo driver boards that interpret the error signals coming from the detector to correctly drive the motors to the demanded position. A photo of the dual axis motor/mirror assembly is available in Fig-

³ <https://www.thorlabs.com/thorproduct.cfm?partnumber=GVS002>

ure 3.12. A thorough analysis of the electrical circuitry of the system and its performance characterization is found in [9].

3.2.3.1 Controlling the mirrors

The position of each mirror is controlled by sending a voltage signal to the respective driver board which is proportional to the mechanical angle of the respective motor. The maximum mechanical scan angle that the GVSoo2 system can handle is $\pm 12.5^\circ$, but it can vary depending on the laser beam diameter and the voltage scaling factor. This particular galvo system offers three different scaling factors which also govern the maximum input voltage applied to the servo boards:

SCALING FACTOR	MAX. VOLTAGE	MAX. SCAN ANGLE
0.5 V/ $^\circ$	± 6.25 V	$\pm 12.5^\circ$
0.8 V/ $^\circ$	± 10 V	$\pm 12.5^\circ$
1 V/ $^\circ$	± 10 V	$\pm 10^\circ$

Through simple trigonometry, it can be shown that the scan angle seen by the focusing lens, called *optical scan angle*, θ_o , is twice the mechanical scan angle applied to the mirror, θ_m . Setting the scaling factor $\alpha = 1V/^\circ$, the maximum optical scan angle then becomes $\pm 20^\circ$, which allows us fully exploit the maximum angle supported by the lens. In this case, the full FOV is scanned if the applied voltage is $v_{max} = \pm 7.5^\circ/(2\alpha) = \pm 3.75$ V.

The beam spot position on the focal plane is related to the mechanical angle applied to the mirrors and the focal length of the lens through the following relation

$$x = EFL \tan(2\theta_{m,x}) \quad (3.21)$$

$$y = EFL \tan(2\theta_{m,y}) \quad (3.22)$$

With a scaling factor equal to α , the voltage signal $v_{x,y}(t)$ will therefore focus the beam at the following position

$$x(t) = EFL \tan\left[2\alpha v_x(t) \frac{\pi}{180}\right] \quad (3.23)$$

$$y(t) = EFL \tan\left[2\alpha v_y(t) \frac{\pi}{180}\right] \quad (3.24)$$

The two signals v_x and v_y are delivered to the driver boards as two pairs of positive voltage signals, (v_x^+, v_x^-) and (v_y^+, v_y^-) , where

$$v_i^+(t) = \begin{cases} v_i(t) & v_i(t) \geq 0 \\ 0 & v_i(t) < 0 \end{cases}, \quad v_i^-(t) = \begin{cases} -v_i(t) & v_i(t) < 0 \\ 0 & v_i(t) \geq 0 \end{cases} \quad (3.25)$$

3.2.3.2 Image distortion

When using a two-mirror system three different effects can appear

1. The arrangement of the mirrors leads to a distortion of the image field, which will be "pillow-shaped" instead of rectangular (fig:galvo-distortion). This is due to the fact that the distance between the two mirrors depends on the mechanical angle applied to the mirrors.

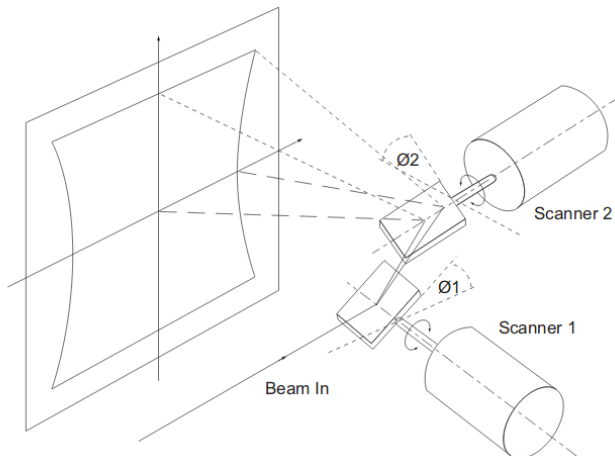


Figure 3.13: Field distortion using two mirrors.

2. From Equation 3.21 and Equation 3.22 we can notice that the distance on the image field is not directly proportional to the applied angle but to its tangent. This can result in an additional distortion effect.
3. If an ordinary lens is used for focusing the laser beam, the focus lies on a sphere. In a flat image field, a varying spot size results.

Galvo system, collimator and scanning lens are housed in a cage system mount⁴ and mounted on a movable vertical support. A photo of the final system is available in Figure 3.14.

⁴ <https://www.thorlabs.com/thorproduct.cfm?partnumber=GCM102/M>

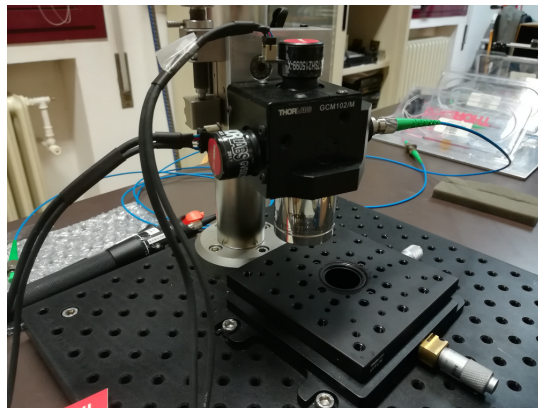


Figure 3.14: The final scanning system.

3.3 ACQUISITION BOARD

In order to digitize the interference signals generated by the OCT system and reconstruct images of the analyzed sample in real time, a specialized high speed data acquisition (DAQ) device is required. A desired feature in a DAQ board for SS-OCT applications is the ability to sample the signals at a variable rate using a supplied k-clock, avoiding the computationally heavy task of data resampling and allowing higher imaging speeds. The DAQ board used for this thesis is the AlazarTech ATS9350⁵, which is designed for OCT, ultrasonic and radar applications.



Figure 3.15: The acquisition board, AlazarTech ATS9350.

This device is an 8-lane PCI Express 2.0 (PCIe x8) card with the following characteristics:

- 12 bits sample resolution
- 250 MHz input bandwidth

⁵ <http://www.alazartech.com/product/ats9350>

- 2 input channels with a dedicated ADC chip and a user selectable sampling rate which ranges from 2 MHz up to 500 MHz. The raw throughput to the on-board memory is thus $T = 2 \text{ bytes per sample} \times 2 \text{ channels} \times 500\text{MHz} = 2 \text{ GB/s}$.
- User selectable input voltage range, from $\pm 40 \text{ mV}$ to $\pm 4 \text{ V}$ for a better utilization of the 12 bit resolution.
- External trigger support
- Variable frequency external clocking
- AUX (Auxiliary) connector that can be configured either as a trigger output or a "acquisition start" trigger.
- dual-port 128 Megasamples on-board memory
- On board Field Programmable Gate Array (FPGA) module for the computation of the Fast Fourier Transform (FFT) on one of the input channels.

The board also comes with the proprietary AlazarDSO software to configure the device, acquire and display signals. For custom applications, the board can be integrated using a supplied Software Development Kit (SDK) which includes libraries and headers for a variety of different programming languages, including C/C++, Python and MATLAB. The device was installed in a Dell Precision T5810⁶ workstation with the following specifications:

- Intel Xeon E5-1650 v4, 3.6 GHz, 6 cores, 12 threads
- 16 GB of DDR4 ECC RAM at 2400 MHz
- 256GB SATA SSD
- NVIDIA Quadro M4000 with 8 GB of DDR5 memory

3.3.1 Data Acquisition

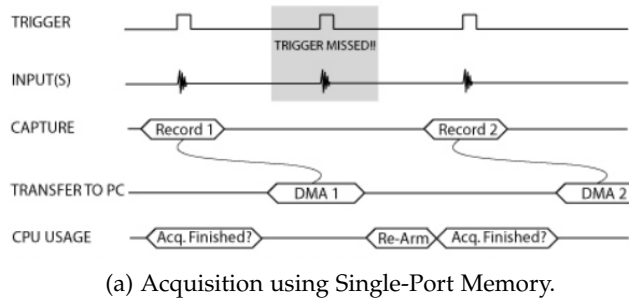
Data acquisition on the ATS9350 is organized in *records* and *buffers*. A record consists in a user defined number of samples acquired by the board for each trigger event. In OCT applications, a record typically corresponds to a single A-scan. A buffer instead is a collection of records and is the format in which data is returned to the user application. For our application, a buffer corresponds to a B-scan.

This DAQ board can be configured to acquire data in one of the following modes

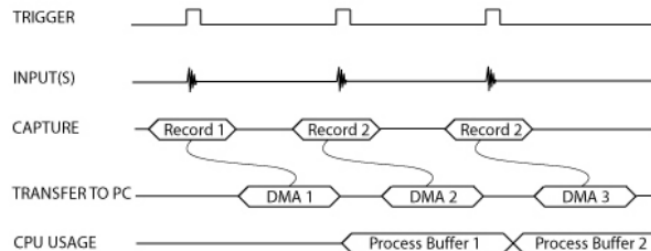
⁶ <https://www.dell.com/us/business/p/precision-t5810-workstation/fs>

1. Single-Port mode acquires data to the on-board memory and then, after the acquisition is complete, transfers data to the host PC memory. This mode can be used if the application can tolerate to miss trigger events that occur while data is being transferred.
2. Dual-Port mode, also called AutoDMA, acquires to on-board memory while, at the same time, transferring data from on-board memory to the host PC memory. This is the preferred acquisition method, as no trigger events are missed by the board while managing the data transfer, meaning that no B-scans are lost by the system. The on-board memory acts as a very long First-In First-Out (FIFO) structure that is able to stream data to the host memory at the rate supported by the motherboard.

The benchmarking tool integrated in the AlazarDSO software measured an average PCIe throughput of 1.735 GB/s, which is even higher than that advertised by AlazarTech.



(a) Acquisition using Single-Port Memory.



(b) Acquisition using Dual-Port Memory.

Figure 3.16: Diagram highlighting the differences between Single-Port acquisitions and Dual-Port acquisitions

In Figure 3.16 a comparison between the two acquisition techniques is available. For single-port acquisitions, in Figure 3.16a we can see that trigger events happening while the Direct Memory Access (DMA) transfer is ongoing are missed completely, and virtually all CPU cycles are used in managing the data acquisition. This leaves no room for data processing on the CPU. In Dual-port AutoDMA acquisition instead (Figure 3.16b) no trigger events are missed and over 95% of CPU time is available for data processing.

This is possible thanks to proprietary circuitry that allows for data transfers to be initiated by the hardware itself, without the need to waste CPU cycles. On the software side, an asynchronous driver is able to parallelize the tasks of setting up a DMA channel while handling data transmission on another channel.

The board supports different types of AutoDMA acquisitions which will be here shortly explained

3.3.1.1 Traditional AutoDMA

This method allows for the acquisition of both pre-trigger and post-trigger data, which will be returned to the user in form of buffers that contain from 1 to 8192 records, one for each trigger event. Each record can come with its own header containing a 40-bit timestamp. A DMA transfer is initiated after the acquisition of each record, copying the data from on-board to user supplied memory.

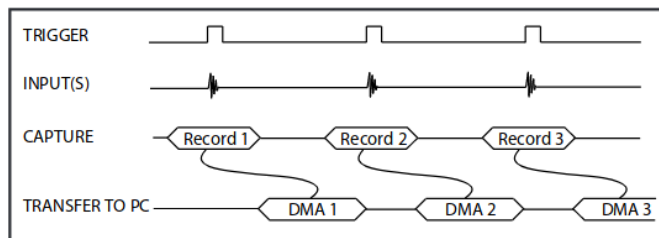


Figure 3.17: Time diagram of a Traditional AutoDMA acquisition.

Fast trigger repeat rates are not supported and can cause the board to overflow even if data transfer is happening at the maximum sustained rate and the on-board memory has not been completely filled.

3.3.1.2 NPT AutoDMA

No Pre-Trigger (NPT) AutoDMA is designed for applications that do not require the acquisition of data before a trigger event. By only storing post-trigger data, the memory bandwidth is optimized. Record headers are also not included, resulting in a more efficient memory utilization. For this reason NPT AutoDMA supports high trigger repeat rates resulting in an acquisition speed which is only limited by the PCIe transfer speed and the rate at which the user application consumes data.

Unlike Traditional AutoDMA, a DMA transfer is initiated only after an entire buffer consisting of multiple records is acquired. This data acquisition method has been specifically designed for ultrasonic scanning, radar and medical imaging applications such as OCT.

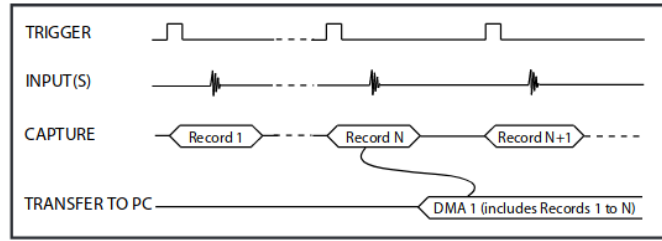


Figure 3.18: Time diagram of a NPT AutoDMA acquisition.

3.3.2 FFT module

The ATS9350 is equipped with a FPGA module that computes the FFT on data records acquired on the first of the two input channels. For OCT applications this means that a powerful GPU dedicated to data processing is not needed, simplifying the user application both on the design and efficiency standpoint. In Figure 3.19 the flow diagram of the FFT module is available: a data record is zero-padded to a power-of-2 length, multiplied by a complex windowing function and fed to the FFT module, whose output is then scaled and optionally converted in a logarithmic scale. At the end of the chain it is possible to obtain either FFT data, time-domain data or both.

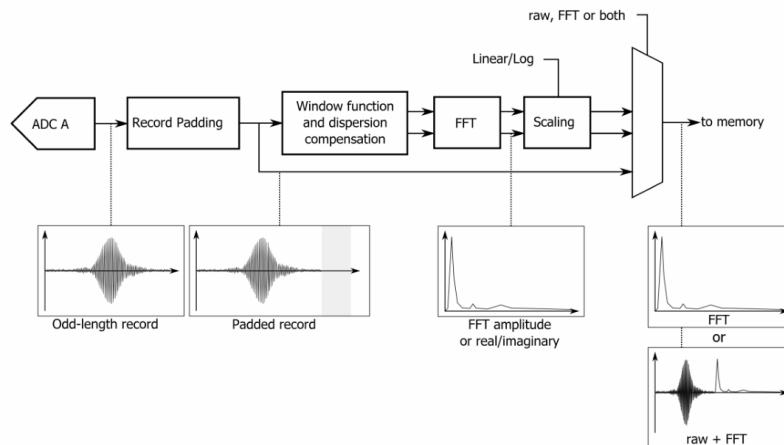


Figure 3.19: Diagram of the FPGA FFT module.

The format of frequency-domain data can be chosen between amplitude, real or imaginary part of the signal and can be converted in either single-precision floating point or unsigned integer.

3.3.3 External clocking

As previously stated, the ATS9350 provides an SMA input for external clocking. This connector supports both sinusoidal and Low-Voltage Transistor-Transistor-Logic (LVTTL) signals, sampling on each

rising edge of the supplied clock. The input impedance of the port is fixed at $50\ \Omega$ and AC coupling is used.

There are three types of supported external clock operations:

1. 10 MHz Reference Clock
2. Slow External Clock, 0 – 60 MHz
3. Fast External Clock, 2 – 500 MHz

Only the third mode is relevant for our application, as the k-clock provided by the Axsun SSOCT-1310 ranges from 180 to 340 MHz. A useful feature of the ATS9350 digitizer is the *dummy clock switchover*: inbetween frequency sweeps some SS-OCT sources generate unstable clocks that do not respect the specification of the board; such behaviour could lead to missed trigger events. In order to avoid this issue, the board can switch to an internally generated clock for a specified amount of time after each record, and switch back to the external source once a trigger signal is detected.

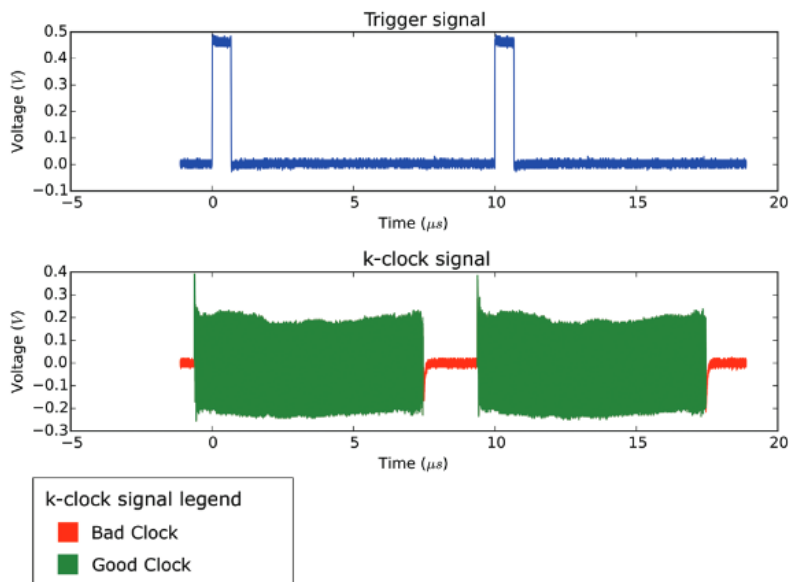


Figure 3.20: Example of bad k-clock that requires the use of the dummy clock switchover.

The use of this feature was not necessary in our case, as the installation of a k-clock deglitching firmware was enough to solve any problem related to bad clocks.

3.3.4 Triggering

The acquisition of A and B-scans requires the ATS9350 to be configured in the following way:

1. The acquisition mode must be set to NPT AutoDMA.
2. The laser sweep trigger, whose rising edge corresponds to the start of an A-scan, is connected to the External Trigger port of the board; as stated above, each record corresponds to an A-scan. The number of samples per A-scan should respect the following rules:
 - a) it should be a minimum of 256
 - b) it should be a multiple of 32
 - c) it should be less or equal to the number of sampling clocks of the k-clock, as specified by the manufacturer of the laser

In our case the number of useful clocks per A-scan is 1536 (Table 3.1), which also satisfies the first two rules. A conservative approach would require to set this number to $1536 - 32 = 1504$, as a minor instability in the laser-generated clock could lead to a number of sampling clocks which is slightly lower, requiring the board to wait for the following A-scan to fill the record and consequently miss a trigger event.

The number of records per buffer instead determines the width of the B-scan.

3. To start the acquisition of a B-scan, the Auxiliary port of the board must be configured as "Trigger Enable In" and a TTL pulse must be supplied to the connector. Once the board detects a rising edge on the AUX port, it will wait for a sufficient number of A-scan triggers to fill a buffer. Once the buffer has been filled a DMA transfer will be started and the image will be delivered to the user application. At the same time, the board waits for another pulse on the AUX port and start the acquisition of a new B-scan.

A more in-depth explanation of the programming of the board will be given in Chapter 4.

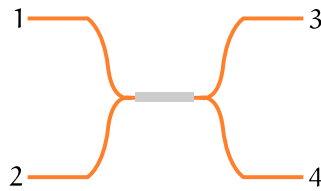
The first two rules are needed for a correct alignment of the samples in memory.

3.4 OPTICAL CIRCUIT

In this section I will detail the process of designing and balancing the fiber optic interferometer that was used to realize the OCT device. Additionally, some performance parameters will be assessed.

3.4.1 Fiber Couplers

In order to build a fiber optic interferometer, a device called *fiber coupler* must be used. A coupler is a 4-port passive device which typically consists in two optical fibers fused together in a common point. Generally it is used as a signal splitter/adder.



The two couples of ports (1,2) and (3,4) are isolated, meaning that a signal that enters the device from port 1 (2) will not exit from port 2 (1) (the same principle holds for ports 3 and 4). The "direct" paths ($1 \leftrightarrow 3, 2 \leftrightarrow 4$) only let through a fraction of optical power equal to ρ^2 with no phase shift while the "crossed" paths ($1 \leftrightarrow 4, 2 \leftrightarrow 3$) let through a fraction $1 - \rho^2$ with a $\pi/2$ phase shift. The scattering matrix of this device is thus easily computed:

$$S = \begin{bmatrix} 0 & 0 & \rho & j\sqrt{1-\rho^2} \\ 0 & 0 & j\sqrt{1-\rho^2} & \rho \\ \rho & j\sqrt{1-\rho^2} & 0 & 0 \\ j\sqrt{1-\rho^2} & \rho & 0 & 0 \end{bmatrix} \quad (3.26)$$

For a 50:50 fiber coupler, $\rho = 1/\sqrt{2}$ so that 50% of the optical power entering from e.g. port 1, will exit from port 3 and the other 50% from port 4.

For this thesis, three fiber couplers were used:

- 2 Thorlabs TW1300R5A2⁷ 50:50 fiber couplers
- 1 Thorlabs TW1300R2A2⁸ 90:10 fiber coupler

The arms of the couplers are color coded to easily distinguish the direct paths, which are White↔White and Blue↔Red.

⁷ <https://www.thorlabs.com/thorproduct.cfm?partnumber=TW1300R5A2>

⁸ <https://www.thorlabs.com/thorproduct.cfm?partnumber=TW1300R2A2>

PATH	Path length [mm]		
	50-50A	50-50B	90-10
White ↔ White	2102	2098.61	2112.58
White ↔ Red	2108.26	2119.47	2113.86
White ↔ Blue	2101.15	2095.97	2129.02
Blue ↔ Red	2107.40	2116.87	2130.3

Table 3.4: Length of the paths of the fiber couplers.

ARMS COUPLE	Path length difference [mm]		
	50-50A	50-50B	90-10
White-Blue	0.84	2.62	16.44
White-Red	6.25	20.85	1.28

Table 3.5: Path difference of each pair of adjacent ports of the couplers.

3.4.2 Measuring the couplers' length

For the design of the interferometer it is useful to determine the length of the coupler's arms with high precision. This was accomplished using an Optical Frequency-Domain Reflectometer (OFDR) and the setup in Figure 3.21.

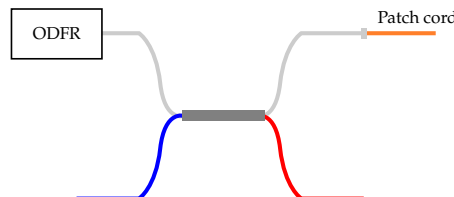


Figure 3.21: Diagram of setup for the measurement of fiber couplers' length.

For each input port, the OFDR trace will contain two peaks corresponding to the reflections generated by the fiber/air interface of the two non-isolated ports, which can be used to determine the length of the optical paths. In order to associate a specific port to its peak, a fiber patch cord was connected to the port, resulting in the reduction of the corresponding peak in the trace. For the same input port a second trace is acquired, switching the position of the patch cord. This procedure is repeated for each of the 4 input ports, for a total of 8 traces per coupler.

The resulting traces are available in Appendix A. The total length of each path and the difference in length between adjacent arms are summarized in Table 3.4 and Table 3.5 respectively.

3.4.3 Mach-Zender Interferometer

In order to test the DAQ device and to determine the effect of sampling an interference signal with laser-supplied k-clock, a simple unbalanced MZI was set up using two 50-50 fiber couplers. The diagram of the setup for this test is reported in Figure 3.22. In order to acquire a beat frequency with the ATS9350, two replicas of the laser pulse have to overlap with a relative delay τ that is less than the source coherence time. Additionally, the beat frequency has to fall in the electronic bandwidth of 1) the photodiodes and 2) the acquisition device. The delay element in the unbalanced interferometer arises from the difference in length of the couplers' arms.

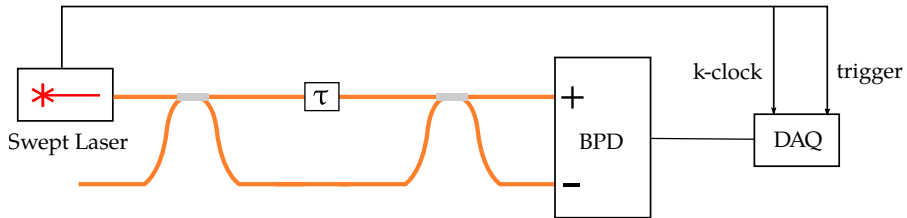


Figure 3.22: Diagram of an unbalanced Mach-Zender Interferometer.

The swept laser emits a signal with a time-varying frequency that can be described as follows

$$E_{ss} = E_{in} e^{j2\pi f(t)t} = E_{in} e^{j\phi(t)}, \quad (3.27)$$

hence the signals at the input ports of the second coupler will be respectively

$$E_1 = \frac{1}{\sqrt{2}} E_{in} e^{j\phi(t-\tau)} \quad E_2 = j \frac{1}{\sqrt{2}} E_{in} e^{j\phi(t)} \quad (3.28)$$

The + and - ports of the BPD will instead see two signals expressed by

$$E_+ = \frac{1}{2} E_{in} e^{j\phi(t-\tau)} - \frac{1}{2} E_{in} e^{j\phi(t)} \quad (3.29)$$

$$E_- = j \frac{1}{2} E_{in} e^{j\phi(t)} + j \frac{1}{2} E_{in} e^{j\phi(t-\tau)} \quad (3.30)$$

which will be converted by the photodiode in the following currents

$$I_+ \propto \langle E_+ E_+^* \rangle = \frac{1}{2} |E_{in}|^2 - \frac{1}{2} \cos [\phi(t) - \phi(t-\tau)] \quad (3.31)$$

$$I_- \propto \langle E_- E_-^* \rangle = \frac{1}{2} |E_{in}|^2 + \frac{1}{2} \cos [\phi(t) - \phi(t-\tau)] \quad (3.32)$$

The output of the BPD will then be the sum the two currents

$$I_{tot} = I_+ - I_- \propto \cos [\phi(t) - \phi(t-\tau)]. \quad (3.33)$$

We can observe that the DC term has been canceled out, leaving only an oscillating term that depends on the phase of the light source.

If the frequency sweep of the laser is assumed linear, the Balanced Photodiode (BPD) generates a sinusoidal current with frequency that is proportional to the OPD between the arms of the interferometer:

$$I_{\text{tot}} \propto \cos [2\pi\sigma_f \tau t + \phi_0]. \quad (3.34)$$

The beat frequency is determined by the OPD Δz through the following relation

$$f = \sigma_f \tau = \sigma_f \frac{n \Delta z}{c_0}, \quad (3.35)$$

where $n = 1.4674$ is the refractive index of the optical fiber used for the manufacturing of the couplers⁹ and c_0 is the speed of light in vacuum.

Connecting the White and Red ports of coupler A to the White and Blue ports of coupler B we obtain $\Delta z = 6.25 - 2.62 \approx 3.63$ mm (Table 3.5), which corresponds to a beat frequency $f \approx 87$ MHz. This frequency is sufficiently low to satisfy Nyquist's criterion and be sampled using the k-clock, as its maximum frequency is ≈ 330 MHz.

The total BPD current was acquired with the ATS9350 digitizer using the provided AlazarDSO software. Two acquisitions were made, first using the internal 500 MHz clock and then clocking the board with the k-clock. In order to synchronize the acquisition with the laser sweep, the board was externally triggered by the sweep-start signal supplied by the laser.

When acquiring with the internal clock, the number of useful samples to acquire was calculated as follows

$$N = F_s \frac{d_c}{f} = 2525, \quad (3.36)$$

where $F_s = 500$ MHz is the sampling frequency, $d_c = 0.505$ is the laser duty cycle and $f = 100$ kHz is the sweep repetition rate. In order to satisfy the bit alignment requirement of the board, the actual number of samples was set to the nearest multiple of 32, $\hat{N} = 2528$. Instead, when using the external clock option of the board, this number is determined by the number of useful sampling instants of the k-clock, 1536 (Table 3.1).

The acquired signals were multiplied by a Hamming window and then Fourier-transformed. The result of this procedure is illustrated in Figure 3.23, where the x-axis is mapped from frequency to OPD by inverting Equation 3.35. We can notice that when using the internal clock of the board, the frequency content of the signal is spread over a relatively wide band (left). In fact, since the frequency sweep is not linear, uniformly sampling the interference signal results in a distorted

⁹ https://www.corning.com/media/worldwide/coc/documents/PI1463_07-14_English.pdf

sinusoidal term. Thus, a precise estimation of the OPD between the MZI arms is not possible.

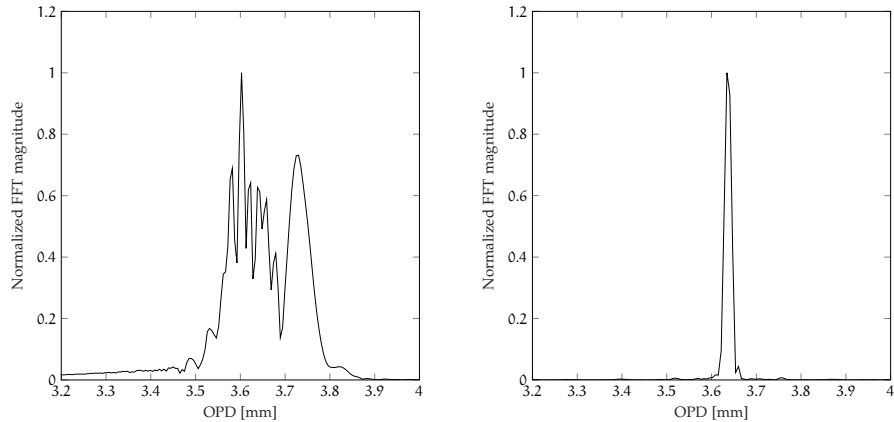


Figure 3.23: Comparison between the beat frequency acquired with the uniform clock (left) and the k-clock (right).

On the other hand, sampling with the provided k-clock produces a clearly defined peak in the frequency domain (right) and permits a precise evaluation of the OPD.

To better appreciate the effect of external clocking on the imaging quality of an OCT system, a sequence of $W = 1000$ consecutive A-scans was captured, from which an artificial B-scan was generated (Figure 3.24).

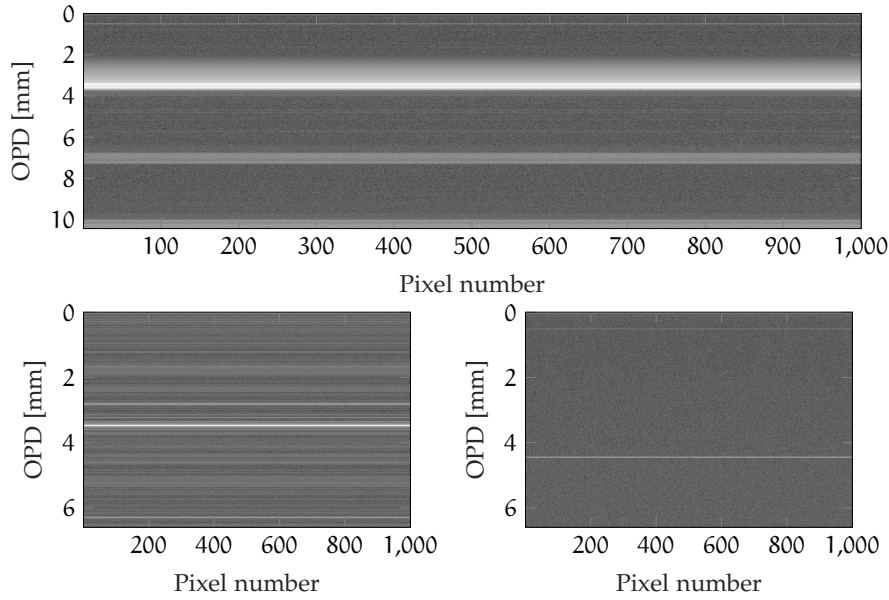


Figure 3.24: Simulated B-scans using the internal 500 MHz clock (top) and the k-clock (bottom).

Using the internal clock and a logarithmic color scale (top), the width of the peak is significantly more pronounced: in this case a

perfect reflector would take up a considerable portion of the imaging range. Moreover, the axial resolution of the OCT would not be acceptable for a functioning system. In this image it is also possible to notice two feeble peaks at ~ 7 mm and ~ 10 mm. These are due to reflections accumulating a delay which is a multiple of the OPD between the arms of the interferometer.

As expected, the improvement when sampling with the k-clock is remarkable (bottom left). We can also notice that since the frequency of the k-clock is smaller than 500 MHz, the second of the two peaks generated by reflections is undersampled and appears at ~ 2.5 mm. When using a real OCT system, this phenomenon will cause artifacts that degrade the overall quality of the final B-scans. Similarly to the complex conjugate artifacts discussed in Chapter 2, portion of the sample will be flipped and superimposed to the part of the sample that lies in the imaging range. A possible solution to this issue consists in the use of an electronic low-pass filter placed after the photodetector, removing the frequency content above the Nyquist frequency of the k-clock.

The third image (bottom right) was captured after distancing the APC connectors on one of the arms of the MZI, introducing a ~ 1 mm layer of air ($n = 1$) which corresponds to an additional ~ 0.68 mm of OPD in the fiber. The reflection peaks in this case do not appear as the received power is too low.

3.4.4 *Fiber Michelson interferometer*

The first OCT circuit that was tested was a simple Michelson interferometer realized with a 50-50 fiber coupler. The schematic diagram of this setup is illustrated in Figure 3.25. The reference arm consists in a cage system with a silver mirror mounted on a translatable support and an adjustable FiberPort collimator (Figure 3.26). This collimator permits a fine alignment with five degrees of freedom to easily maximize the amount of power that is coupled back in the optical fiber after being reflected by the mirror. Through a careful alignment procedure, the attenuation of the reference arm is minimized, reaching a value of ~ 4 dB.

This setup, while fairly simple, gave rise to two different issues:

1. a balanced detection scheme could not be implemented.
2. the output of the optical source experienced instability, as half of the power reflected by the two arms is coupled back in the laser output port. This behaviour was tested by replacing the reference arm with a photodiode and monitoring its current. In Figure 3.27 we can see that the power profile of the source is substantially distorted when a high-reflectivity object such as a mirror is placed under the scanning lens of the sample arm.

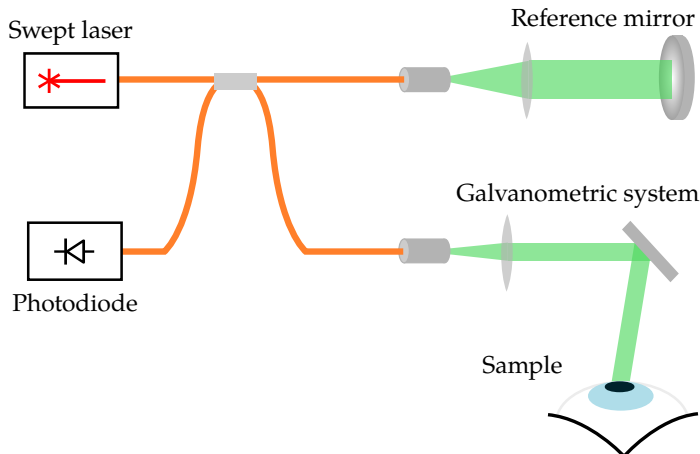


Figure 3.25: SS-OCT setup using a fiber coupler as a Michelson interferometer.

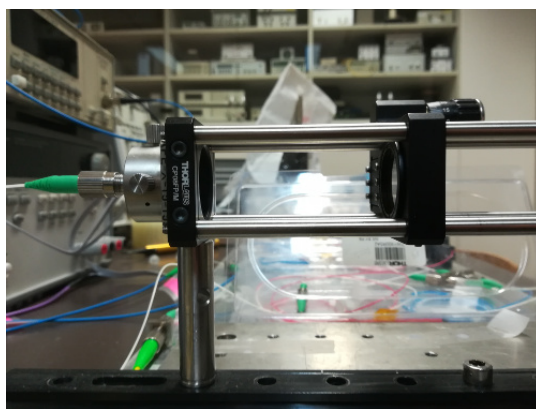


Figure 3.26: The reference arm used for this setup. The adjustable fiber collimator (left) and translatable mirror (right) are visible.

With the additional power reflected by the reference mirror this behaviour can only worsen.

3.4.5 Second scheme

In order to limit the amount of power returning to the laser and avoid permanent damage, the setup in Figure 3.28 has been designed. Connecting the source to the 90-10 coupler, only 10% of the total output power is directed to the sample and only 10% of the reflected power is directed back to the laser, reducing the total power returning to the input port by a factor of 25. The power profile of the source was measured by connecting a photodiode to connector D and monitoring its current. Unlike before, placing a mirror in the sample arm did not alter the shape of the laser pulse.

With respect to the previous scheme, the power returning to the laser from the reference arm is attenuated by ~ 2 dB thanks to the 90-

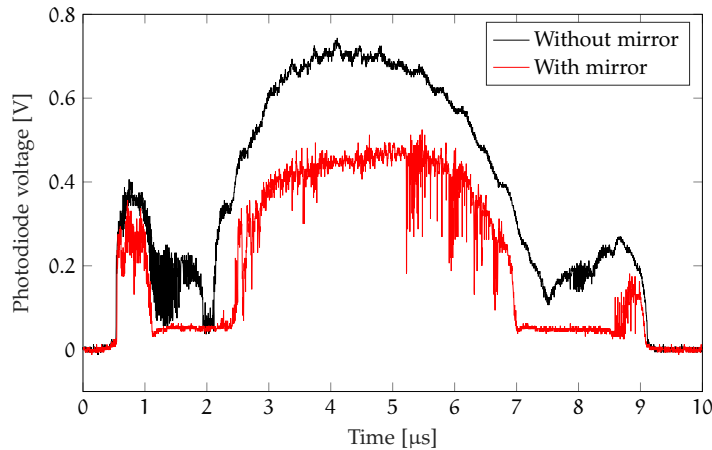


Figure 3.27: Instability of the laser output power.

10 coupler. The effect of the reference arm on the stability of the laser output was tested in a similar way, connecting the photodiode to connector I. With the silver mirror stilll on the sample arm, the FiberPort collimator was slightly mis-aligned until the measured power profile did not exhibit any distortion.

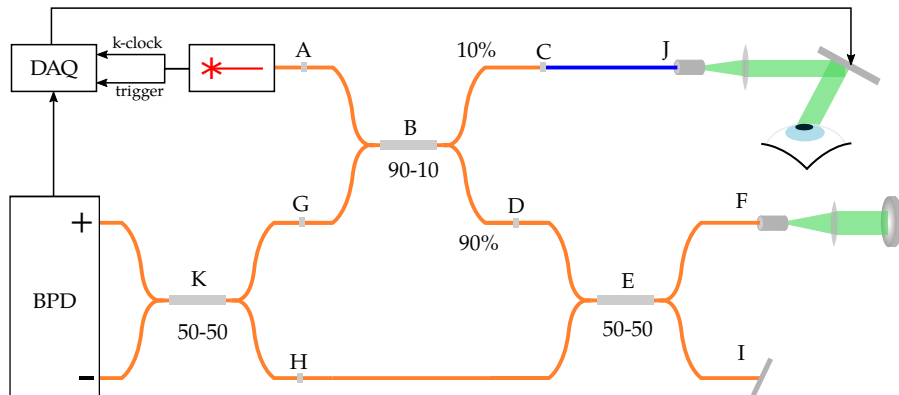


Figure 3.28: Final SS-OCT setup.

3.4.5.1 Balancing the interferometer

As already explained, interference fringes are only visible if the mismatch between the length of sample and reference arm is less than the coherence length of the source.

With reference to Figure 3.28, the length of the sample arm, defined by the letters ABCJCBGK is

$$L_{\text{sample}} = \overline{ABCJCBGK} = 5L_{\text{arm}} + 2L_{\text{patch}}, \quad (3.37)$$

where L_{arm} is the length of the couplers' arm and L_{patch} is the length of the fiber patch cord connecting the first coupler to the scanning

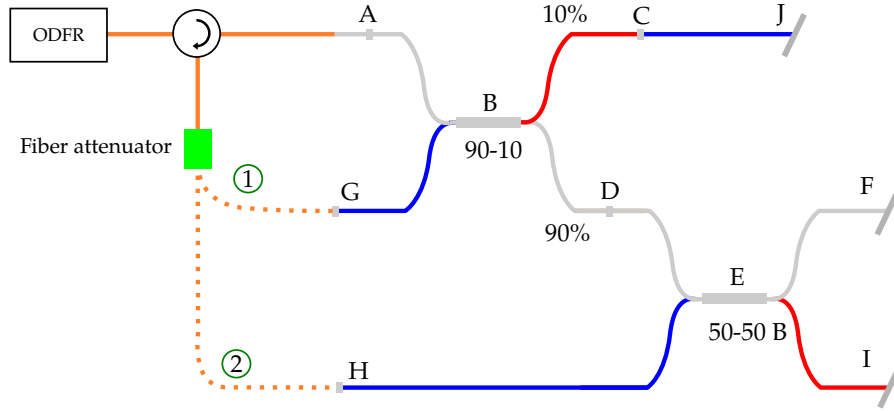


Figure 3.29: Time signal when the optical path difference is close to 0.

system (illustrated in blue). The reference arm is instead defined by the path ABDEFEHK, whose length is

$$L_{\text{ref}} = \overline{ABDEFEHK} = 7L_{\text{arm}}, \quad (3.38)$$

meaning that, ideally

$$|L_{\text{ref}} - L_{\text{sample}}| = 0 \implies L_{\text{patch}} = L_{\text{arm}}, \quad (3.39)$$

Since $L_{\text{arm}} \sim 1 \text{ m}$, a patch cord of the same length has to be used. Potentially, light travelling the path ABDEFEDBGK could cause unwanted interference, but since

$$|L_{\text{ref}} - \overline{ABDEFEDBGK}| = 2L_{\text{arm}} \approx 2 \text{ m}, \quad (3.40)$$

the mismatch is far greater than the coherence length of the source, $l_c \approx 12 \text{ mm}$, meaning that no interference will be generated.

This setup is therefore able to protect the laser source from damage caused by strong reflections, removes unwanted coherent noise and enables balanced detection. In order to minimize distortions due to the detection scheme, the BPD is connected to the fiber coupler with the smallest mismatch between adjacent ports: looking at Table 3.5, the Blue and White arms of coupler 50-50 A are the optimal choice.

3.4.5.2 OFDR measurement

For a more precise analysis on the balancing of sample and reference arm, the difference between the two optical paths is measured with an OFDR using the setup in Figure 3.29. The optical circulator enables us to select the path to measure, obtaining traces that are easier to interpret, while the fiber attenuator is used as a safety measure to protect the OFDR receiver.

The acquired traces are illustrated in Figure 3.30. From left to right we can observe:

- The reflection coming from connector C, when no patch cord is connected.
- The reflection coming from connector J, corresponding to the end of the fiber patch cord.
- The two reflections coming from connectors F and I. As we can see, the two are distanced by ~ 2 centimeters, confirming the measurements reported in Table 3.5.

Using connector F to connect the reference system, the path length difference becomes $\Delta L \approx 35$ mm. Since the interference between the two signals occurs in the fused section of coupler 50-50 A (point K in Figure 3.28), the length mismatch of its White and Red arms (≈ 6.2 mm) can be exploited to bring the total OPD down to $\Delta L \approx 29$ mm. These 3 centimeters can then be compensated with the translatable mirror in the reference arm. It is important to closely match the space travelled by the two arms in the same medium to minimize the effect of chromatic dispersion, which can hinder the axial resolution of the final system.

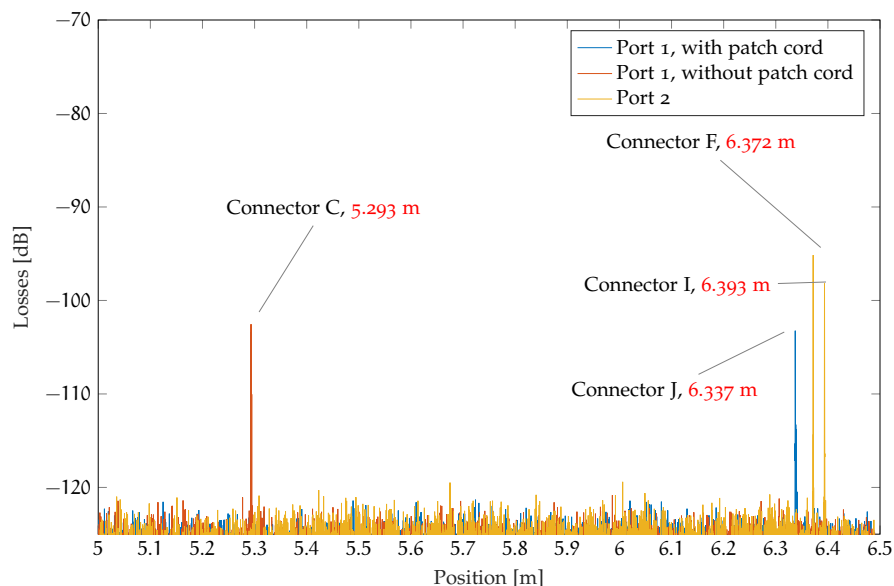


Figure 3.30: OFDR traces used to balance the interferometer.

After connecting the scanning system and the reference arm, a silver mirror was placed on the focal plane of the focusing lens and the interference signal detected by the photodiode was monitored with a high-speed oscilloscope. The reference mirror was translated until the beat frequency was close to 0. In Figure 3.31 we can see the signal captured at three different instants and observe the low-frequency oscillation.

Finally, with the aid of the spectrum analyzer feature of the AlazarDSO software, the reference mirror was further adjusted in order to position the focal plane of the lens in the middle of the imaging range. An

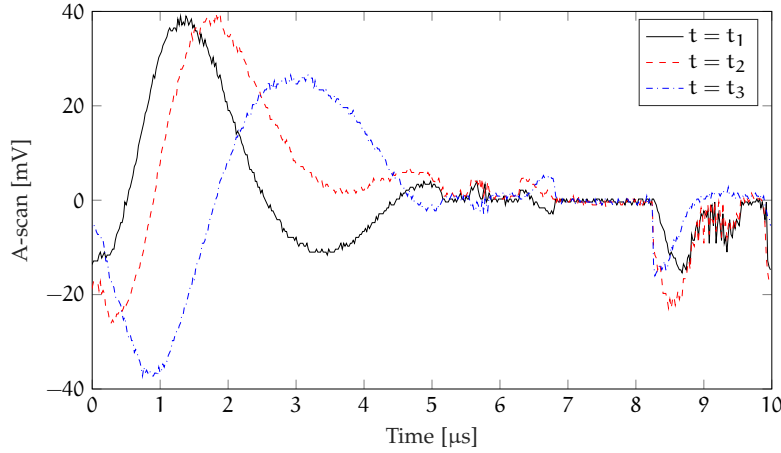


Figure 3.31: Time signal when the optical path difference is close to 0.

A-scan of the silver mirror was acquired using the external clock and a Hamming apodization window, resulting in the plot in Figure 3.32.

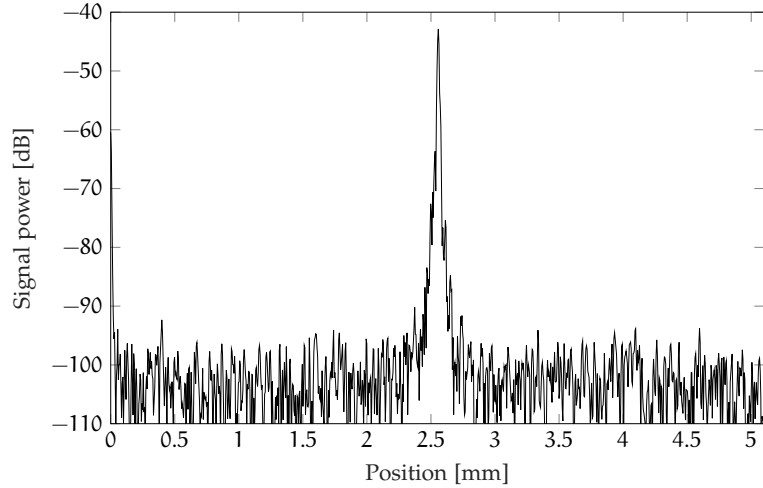


Figure 3.32: Time signal when the optical path difference is close to 0.

3.4.6 Signal-to-noise ratio profile

In order to test the combined effect of sensitivity falloff and the limited DOV of the lens, multiple A-scans were acquired while placing the mirror at different imaging depths. This was accomplished by translating the scanning system on a vertical support with the help of a micrometer screw. The whole imaging range was covered with 11 acquisitions at multiples of $\sim 500 \mu\text{m}$, resulting in Figure 3.33. An additional acquisition has been acquired without placing the silver mirror on the sample arm to obtain the noise level of the system.

The signal-to-noise ratio (SNR) profile was then measured by subtracting the average noise level from the peak power of each A-scan,

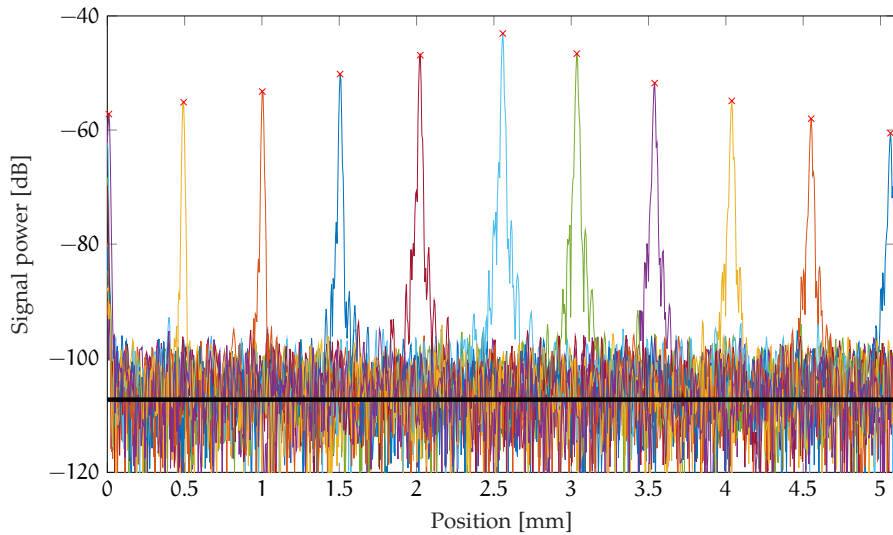


Figure 3.33: A-scans of a silver mirror at various imaging depths.

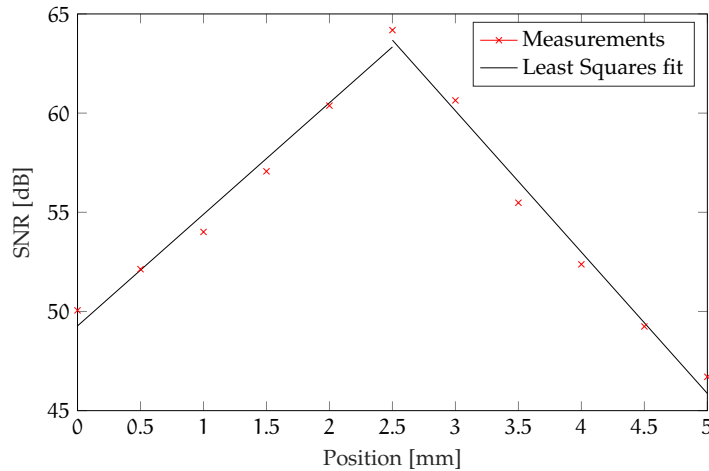


Figure 3.34: Signal-to-noise ratio falloff.

obtaining the graph in Figure 3.34. The SNR dropoff factor was determined by fitting the data points to two lines using the Linear Least Squares method, obtaining $\alpha' = 5.6 \text{ dB/mm}$ for the first half of the imaging range and $\alpha'' = 7.1 \text{ dB/mm}$ for the second half, guaranteeing a 6 dB range of $\sim 1.86 \text{ mm}$.

3.4.7 Axial Resolution

The axial resolution of a OCT system is arguably its most important parameter. As discussed in Chapter 2, the resolution of an SS-OCT

can be estimated in the case of a Gaussian source with Equation 2.33. For our source, this value is found to be

$$\delta z = 0.75 \frac{\lambda_0^2}{\Delta\lambda} = 0.75 \frac{(1305 \times 10^{-9})^2}{140 \times 10^{-9}} \approx 9.12 \text{ } \mu\text{m}. \quad (3.41)$$

Since the spectrum of the laser is not Gaussian, the axial resolution has to be determined experimentally by measuring the FWHM of the A-scan generated by a mirror. This measurement will also take into account all the dispersion introduced by the optical components of the system. The acquired A-scans will first be spline-interpolated and then fit to a Lorentzian function of the form

$$L(x) = L_0 + \frac{A}{\pi} \frac{\frac{1}{2}\gamma}{(x - x_0)^2 + (\frac{1}{2}\gamma)^2}, \quad (3.42)$$

to determine the FWHM parameter $\gamma/2$. Figure 3.35 pictures the results of this method when using four different apodization functions. The Blackman-Harris window guarantees the worst result of the four, while the Hanning and Hamming windows improve the resolution by about 3 μm . The best result is instead achieved by the Kaiser window, which is just 2 μm short from reaching the theoretical value. A side effect of using the Kaiser window is the introduction of more pronounced side lobes which can result in distorted images. Further improvements to the axial resolution could be achieved by replacing the fiber patch cord connecting the interferometer to the scanning system. In fact, this patch cord is a SMF centered at 1550 nm which is not designed to work in the 1300 nm range used by the laser, meaning that modal dispersion could impact the system's performance.

The same method was tested for different mirror depths in order to estimate the behaviour of the resolution over the whole imaging range. The obtained profile is presented in Figure 3.36, A few observations can be made

- The resolution worsens at higher imaging depths. This can be explained by the fact that light has to travel for longer distance in air, therefore enhancing the dispersion mismatch between the sample and reference arm.
- The Kaiser window exhibits a more irregular trend compared to the other three windows while still generally guaranteeing the best axial resolution.
- The variation in axial resolution is in the order of 2-3 μm over the entire imaging range for all four windows.

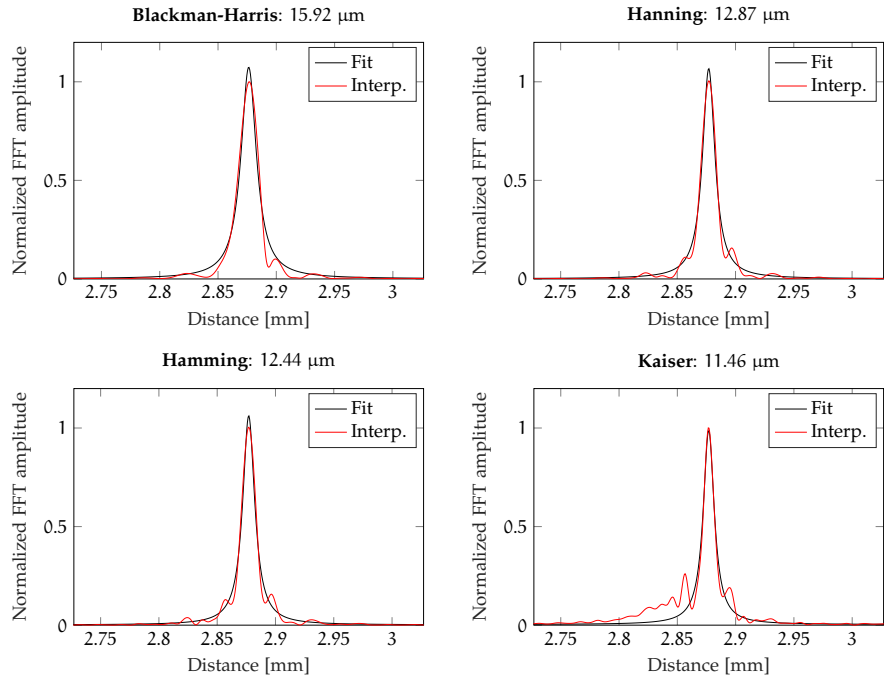


Figure 3.35: Experimental determination of the axial resolution of the system fitting the A-scan of a silver mirror to a Lorentzian function using a Nonlinear Least Squares method.

3.4.8 Thickness measurements

The simplest type of measurement that can be performed with an OCT system consists in the estimation of the thickness of various layers of a sample. This technique, also called *axial ranging*, was the first example of OCT imaging demonstrated in the literature [19].

The first sample we measured is a Thorlabs R1L1S1N¹⁰, which is a test target designed for the calibration and the determination of the resolution of imaging systems (Figure 3.37). It consists in a $18 \times 18 \times 1.5$ mm³ soda lime glass substrate with the top surface coated with a reflective chrome layer apart from a clear pattern that lets light penetrate.

Positioning the target in such a way that the light beam exiting the scanning lens hits the clear pattern, the A-scan in Figure 3.38 is produced. The two peaks correspond to the top and bottom surface of the glass substrate. Dividing the z-axis by the refractive index of soda lime glass ($n \sim 1.51^{11}$), we measure the thickness as the distance between the two peaks, obtaining

$$\Delta z \approx 1.58 \text{ mm}, \quad (3.43)$$

¹⁰ <https://www.thorlabs.com/thorproduct.cfm?partnumber=R1L1S1N>

¹¹ <https://refractiveindex.info/?shelf=glass&book=soda-lime&page=Rubin-clear>

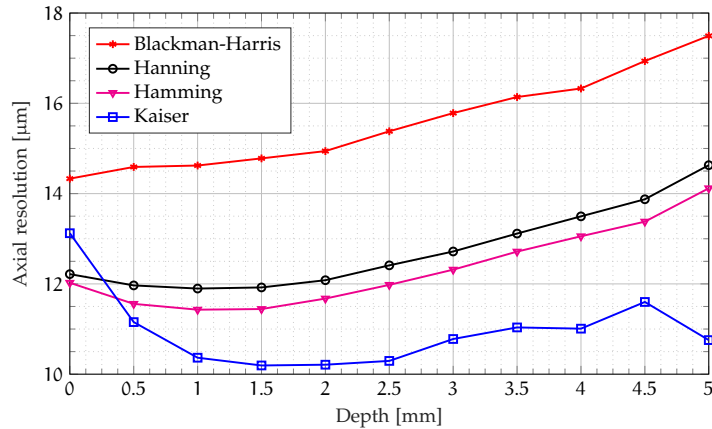


Figure 3.36: Axial resolution profile on the entire imaging range using four different apodization windows.



Figure 3.37: Image of the R1L1S1N target.

which is acceptable considering the uncertainty on the refractive index and the real thickness of the target.

A second thickness measurement was performed on a single mode optical fiber using a refractive index of $n = 1.46$. From the A-scan in Figure 3.39, the diameter of the fiber is measured as

$$\Delta z = 0.249 \text{ mm}, \quad (3.44)$$

which is typical for a SMF with the external acrylic coating and no plastic casing.

REMARK In both of the A-scans in Figure 3.38 and Figure 3.38 only the reflections generated by the interface between two different materials is detected by the photodiode, while no scattering coming from the glass itself is visible. The cause of this issue is identified in the lack of transimpedance amplifier in the balanced photodiode circuitry, meaning that the power scattered by the internal structure of the material is drowned by the noise of both photodetector and acquisition board. Several other samples were tested with this setup, but only plastic and metallic objects were able to reflect a sufficient amount of power. This issue is addressed in the following chapter.

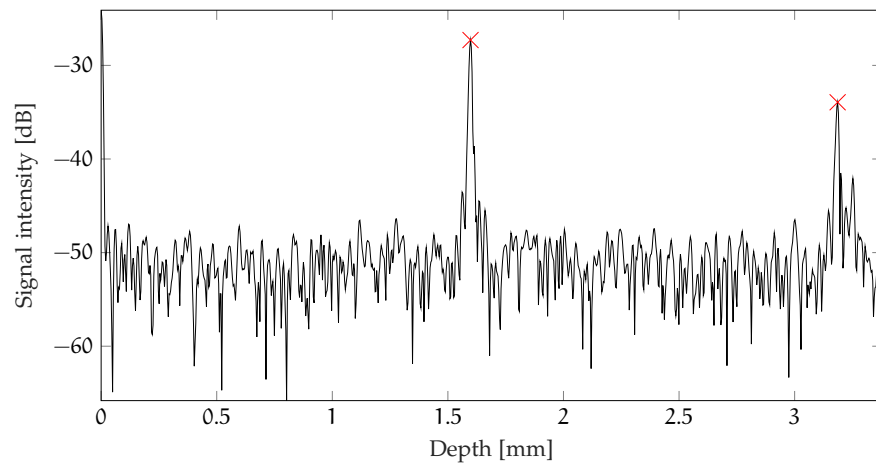


Figure 3.38: Axial measurement of the R1L1S1N target.

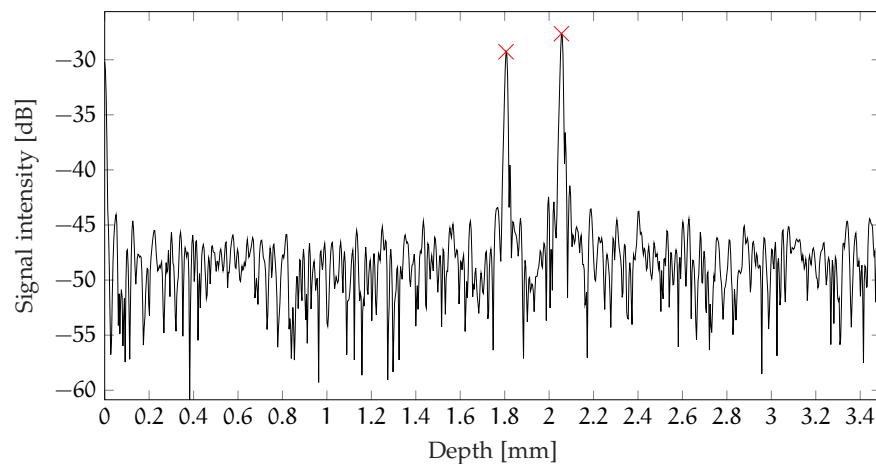


Figure 3.39: Axial measurement of a SMF with its acrylic coating.

4

RESULTS

This chapter is dedicated to the description of the OCT software that was developed for this thesis. This application handles the data acquisition task, controls the galvanometric system and performs real-time processing and visualization of the acquired OCT data.

The transversal resolution of the system described in Chapter 3 is also evaluated using the test resolution target introduced in the same chapter.

Finally, a series of B-scans, C-scans and *en-face* images of a variety of different samples is presented. A subset of these images were acquired using a second SS-OCT system designed to work in the 1060 nm range.

4.1 DATA ACQUISITION SOFTWARE

The final component that is needed to obtain a working SS-OCT system is a computer application that handles data acquisition and image visualization. This program should be able to achieve real-time performances, enabling a low-delay video stream of cross-sectional OCT data. Ideally, the total acquisition rate of the system in terms of B-scan/s should be limited by the scanning speed of the galvanometric mirrors and not by the OCT software. In fact, given the transversal resolution of the system, the FOV of the scanning lens and the spot size on the focal plane, there exists a maximum frequency at which the mirrors can be driven in order to obtain distortion-free images. An extensive analysis on this matter is carried out in [9].

The application is developed for the Windows 10 Operating System using the Object-Oriented C++ programming language, which is the only one that allows low-level memory management among those supported by the ATS9350 acquisition board. Additionally, it permits the native integration of the high performance graphics library called OpenGL¹.

The code is built using the Qt application framework², which consists in a set of tools for event handling and the design of GUIs. In Qt, asynchronous code can be easily written using the Signals and Slots

¹ <https://www.opengl.org/>

² <https://www.qt.io/>

paradigm: when a particular event occurs, an object *emits* a signal; objects that are connected to this signal will execute the appropriate slot, which is a function that takes the parameters passed by the connected signals and perform some actions. For example, the object dealing with OCT data acquisition can emit a signal with a newly acquire B-scan, while a data visualization object connected to this signal can retrieve this data and display it without blocking the acquisition task.

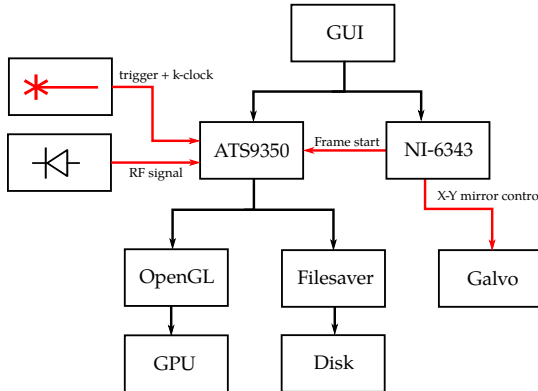


Figure 4.1: Data flow of the OCT application.

The data flow of the application is illustrated in Figure 4.1. The GUI initiates an acquisition by communicating with the ATS9350 board and an additional DAQ board dedicated to the control of the galvo mirrors and to supply a "frame start" signal. This device is the National Instruments USB-6343³, which is a USB board equipped with 4 analog outputs, 32 analog inputs and 48 digital I/O ports capable of 900 kilosamples/s. Once the ATS9350 receives the "frame start" signal, it will listen for A-scan triggers provided by the Axsun laser and start sampling the interference signal using the k-clock. After the acquisition of a B-scan is complete, the board returns a memory block containing the acquired data to the application, that will then process it and send it to two objects which asynchronously display it using OpenGL and save it to disk.

4.1.1 Controlling the galvanometric mirrors

In order to control the galvo system, voltage signals that are proportional to the scan angle have to be sent to its driver boards. As explained in Chapter 3, two separate signals are needed for each mirror: one for positive and one for negative angles. This requires the use of a DAQ board with at least 4 analog output ports, explaining the choice of the USB-6343.

To scan an area of the sample, the X motor is driven with a triangle wave of frequency f_b while the Y motor is controlled with a "staircase"

³ <http://www.ni.com/it-it/support/model.usb-6343.html>

signal with a number of "steps" equal to the number of frames in the volume. At the start of each rising edge of the triangle wave, a TTL pulse will also be generated and sent to the AUX port of the ATS9350 board to signal the start of a B-scan. An example is available in Figure 4.2, where the B-scan frequency is $f_b = 20$ Hz, and the number of frames per volume is equal to 4. Using these voltages, the area that will be scanned is equal to

$$A = \left[2EFL \tan \left(2 \times 2V \times 1^\circ / V \times \frac{\pi}{180} \right) \right]^2 \approx 7.55 \times 7.55 \text{ mm}^2. \quad (4.1)$$

If only cross-sectional images are required, the Y motor will be controlled with a constant voltage.

During the falling edge of the triangle wave the X mirror will return to its initial position, meaning that the data generated in this time interval is not useful. Hence, the number of A-scans to acquire in order to scan the entire space covered by this mirror is

$$N = \frac{1}{2} \frac{f_a}{f_b}, \quad (4.2)$$

where $f_a = 100$ kHz is the sweep repetition rate of the laser.

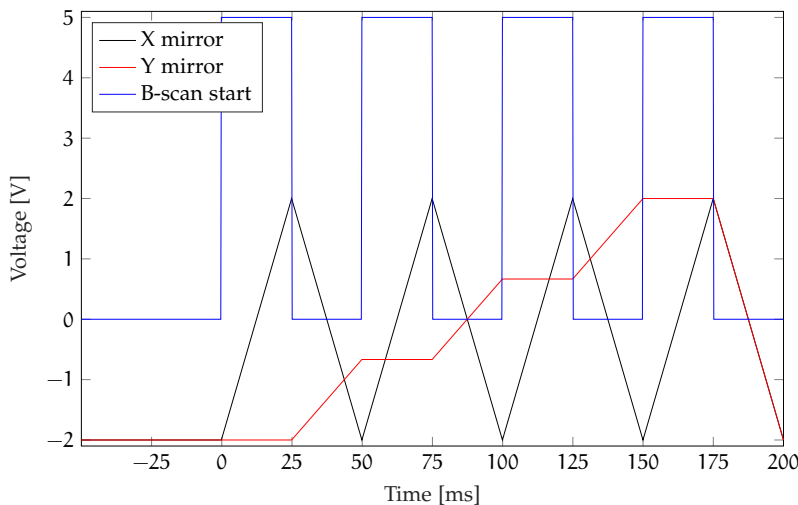


Figure 4.2: Signals used to control the galvanometric mirrors.

Recalling that the each signal must be split in its positive and negative parts as in Equation 3.25, the actual signals that will be sent to the galvo driver boards will look like those in Figure 4.2.

Configuring the NI-6343 board

The control of the USB-6343 board is integrated in the OCT application using the DAQmx drivers developed by National Instruments.

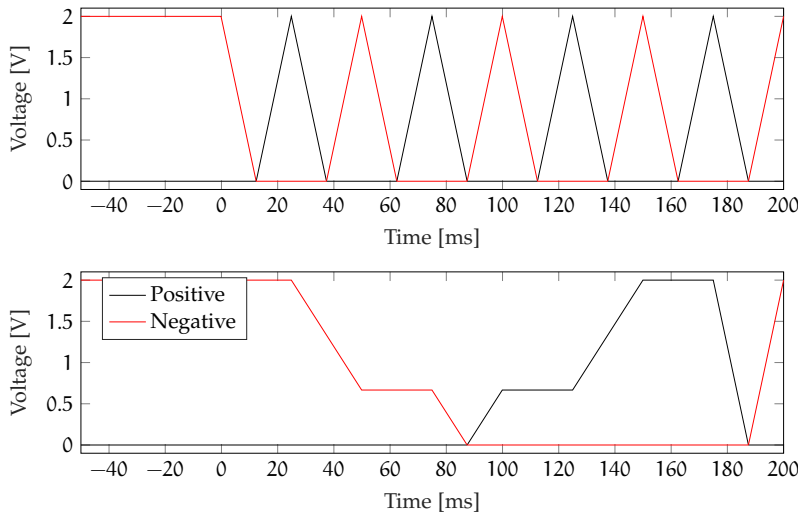


Figure 4.3: Signals used to control the galvanometric mirrors.

The program is organized in *tasks*; each task is a collection of channels which corresponds to a measurement or generation to perform and that can be configured independently to other tasks, specifying triggering, timing and other properties.

In our case two tasks are created:

1. Digital Task: handles the generation of the "Frame start" signal. It consists in a single digital channel which can be configured as a "digital pulse" with the `DAQmxCreateCOPulseChanFreq` function, specifying the output port of the board, the frequency of the pulse and its duty cycle. In order to generate a sequence of pulses instead of just a single one, the function `DAQmxConfigImplicitTiming` must be called to configure the task as "continuous generation".
2. Analog Task: drives the galvo system with the aforementioned signals. This task is a collection of four analog channels, which can be added with the `DAQmxCreateAOVoltageChan` command, specifying the output ports and a maximum expected voltage.

The signals are computed and stored in an array of floating point samples which will be uploaded to a buffer on the board and converted into a continuous signal by a Digital-to-Analog Converter (DAC). The length of each signal is determined by the selected generation rate R_{clk} , the B-scan rate f_B and the number of frames per volume N_v as

$$N_{samples} = R_{clk} \cdot \frac{1}{f_B} \cdot N_v, \quad (4.3)$$

meaning that the buffer uploaded to the board has length $4 \cdot N_{samples}$, as two analog signals are required for each mirror. Just

like before, "continuous generation" must be configured, otherwise a single volume (or a single frame in case of 2D acquisition) will be scanned. To synchronize the two tasks, analog data generation is triggered by the digital pulse train created above using the `DAQmxCfgDigEdgeStartTrig` function.

4.1.2 Programming the ATS9350

In Chapter 3, the different acquisition modes supported by the ATS9350 board were introduced. In particular, for OCT applications No-Pre-Trigger AutoDMA must be used, as it is the only method which supports high trigger repeat rates.

Data is organized in records and buffers: records correspond to a series of samples acquired for each trigger event, while buffers are a collection of 1 or more records. In OCT, records correspond to A-scans while buffers contain a complete B-scan.

The data transfer between the board and the software works as follows:

1. A list of data buffers are allocated on the PC and assigned to the board
2. The board will acquire the number of records necessary to fill a buffer into its main memory.
3. Once the records have been acquired, an AutoDMA transfer will start copying the records from the on-board memory to the application buffer. At the same time, the board is acquiring new records to fill the next buffer, so no trigger events are missed while copying data to the PC.
4. After the DMA transfer is complete, the board generates an interrupt, causing an event message to be sent to the application so it can start consuming data.
5. Once the buffer has been processed by the application, it must be returned to the board. The processing time must be sufficiently low so that the board will always have one buffer available, otherwise the acquisition will fail with a *buffer overflow* error.

4.1.2.1 Triggering and Clocking

Using the C++ library and headers supplied by AlazarTech, the board can be integrated in the OCT application and configured as needed. To start the acquisition of a B-scan, the AUX connector of the board is configured as "Trigger Enable In", meaning that every time a positive edge is detected on this connector the board will begin capturing a set amount of A-scans. This can be done with the following command:

```
AlazarConfigureAuxIO(boardHandle, AUX_IN_TRIGGER_ENABLE,
    TRIGGER_SLOPE_POSITIVE);
```

To trigger the acquisition of an A-scan instead, the sweep trigger provided by the laser is connected to the external trigger port. The board provides an advanced triggering system with two separate trigger engines, called J and K, that can either be used independently or combined to generate complex trigger events. In our case, engine K is disabled and engine J is configured to generate a trigger event when the signal connected to the external port reaches $V_{\text{trig}} = 0.71$ V. This value is passed to the board as an 8-bit integer code, calculated as

$$\text{trigger code} = 128 + 127 \times \frac{\text{trigger voltage}}{\text{input range}} \quad (4.4)$$

$$= 128 + 127 \times \frac{0.71}{5} = 146. \quad (4.5)$$

```
AlazarSetTriggerOperation(
    boardHandle,
    TRIG_ENGINE_OP_J,
    TRIG_ENGINE_J,
    TRIG_EXTERNAL,
    TRIGGER_SLOPE_POSITIVE,
    triggerCode,
    TRIG_ENGINE_K,
    TRIG_DISABLE,
    TRIGGER_SLOPE_POSITIVE,
    128);
```

Similarly, clocking the board with the k-clock is achieved by using the `AlazarSetCaptureClock` function to select the clock source and the `AlazarSetExternalClockLevel` function to select the voltage level at which samples are captured.

4.1.2.2 FFT module configuration

Achieving real-time performance without the use of GPGPU is possible only with the use of the onboard FPGA module that computes the FFT of acquired records. To configure this module, the following code snippet is used

```
AlazarFFTSetup( fftHandle,
    CHANNEL_A,
    samplesPerAscan,
    fftLength,
    FFT_OUTPUT_FORMAT_U16_LOG,
    fftFooter,
    0,
    &bytesPerOutputRecord
);
```

where

- CHANNEL_A is the channel used for data acquisition,
- samplesPerAscan = 1536 is the number of useful sampling clocks of the k-clock (Table 3.1).
- fftLength = 2048 is the length of the computed FFT.
- FFT_OUTPUT_FORMAT_U16_LOG is the format in which FFT data is returned to the application, meaning that an FFT sample is computed in logarithmic scale and stored in an unsigned 16-bit integer.
- bytesPerOutputRecord is the size of an FFT record, which in this case is equal to $2 \times \text{fftLength} = 4096$ bytes.

This means that setting a B-scan frequency f_b , the size of a buffer is given by

$$\text{bytesPerBuffer} = \frac{1}{2} \frac{f_a}{f_b} \cdot 4096 \text{ bytes}, \quad (4.6)$$

which for $f_b = 20$ Hz is equal to 10.24 Megabytes, corresponding to 2500 A-scans per B-scan.

Additionally, the FFT module can be configured to zero-pad and multiply time domain records by a windowing function:

```
AlazarDSPGenerateWindowFunction(
    windowType, // type of window to generate
    window, // memory to store window
    samplesPerAscan, // length of the fft input
    fftLength - samplesPerAscan // zero-padding
);

AlazarFFTSetWindowFunction(
    fftHandle,
    fftLength,
    window,
    NULL // reserved
);
```

4.1.2.3 The acquisition loop

After determining the width of each B-scan, and consequently the buffer size, a list of buffers has to be allocated on the PC and posted to the board to be used for AutoDMA transfers.

```
for (unsigned int i = 0; i < bufferCount; i++)
{
    U16 *buffer = (U16*)VirtualAlloc(NULL, bytesPerBuffer,
        MEM_COMMIT, PAGE_READWRITE);
```

```
    AlazarPostAsyncBuffer(boardHandle, buffer, bytesPerBuffer);
}
```

The application will wait for the board to fill these buffers with a B-scan by using the `AlazarDSPGetBuffer` function, which returns when a DMA transfer has completed. Once this happens, the B-scan will be converted to floating point values, copied to a new buffer to be stored on disk, and then converted to suitable format to be uploaded to the GPU and be visualized on screen. After these operations are completed, the buffer is returned to the board.

In order to keep the GUI responsive, the following loop has to be run on a separate thread:

```
unsigned int acquiredBuffers = 0;
while (acquiredBuffers < totalBscans)
{
    int bufferIndex = acquiredBuffers % bufferCount;
    U16* buffer = bufferArray[bufferIndex];

    // wait for the buffer to be filled
    AlazarDSPGetBuffer(boardHandle, buffer, timeout)

    // process B-scan
    float *floatBscan = convertToFloat(buffer);
    byte *Bscan = convertToImage(floatBscan);

    emit saveToDisk(floatBscan);
    emit uploadToGPU(Bscan);

    // return buffer to the board
    AlazarPostAsyncBuffer(boardHandle, buffer, bytesPerBuffer)
}
```

To remove the complex conjugate artifacts introduced in Chapter 2, half of the data points are dropped, reducing the number of samples of each B-scan to

$$N_{\text{samples}}^{\text{B-scan}} = \frac{1}{2} \frac{f_a}{f_b} \cdot 1024 \quad (4.7)$$

B-scans are processed using a multi-processing approach enabled by the OpenMP⁴ Application Programming Interface (API), reducing the processing time needed and minimizing the total delay.

The floating point values from which the image is computed are first clipped in an interval $[I_{\min}, I_{\max}]$ controlled through the GUI and then mapped to a 1-byte integer with values in $[0, 255]$, enabling the user to filter out the noise floor and improve the contrast of the image.

⁴ <http://www.openmp.org/>

```

...
    if (sample > Imax)
        sample = Imax;
    if (sample < Imin)
        sample = Imin;
    float range = Imax-Imin;
    byte pixelValue = 255*(sample - Imin)/range;
...

```

Finally, the raw floating point data are sent to an object that asynchronously saves it to disk, while the computed image is displayed with OpenGL.

4.1.3 Processing time and delay

Real-time data acquisition and visualization is achieved if the mean processing time of a B-scan is smaller than the time between two consecutive "frame start" signals:

$$\mathbb{E}[T_p] < T_b = \frac{1}{f_b}. \quad (4.8)$$

If this inequality is not respected the delay will grow indefinitely, regardless of the amount of buffers posted to the board. In fact, if T_p is constant and smaller than T_b , two buffers would be sufficient, but given that the processing time is a stochastic process, allocating more buffers can prevent the board from overflowing due to external factors temporarily slowing down the processing speed, like processes with higher priority in non-real time Operating Systems.

The average processing times were measured varying the B-scan frequency f_b and the number of CPU cores used in the acquisition loop, acquiring 1000 B-scans for each scenario. As can be observed in Figure 4.4, the application can comfortably sustain the processing load for the entire range of framerates that was tested using just a single core.

Even though a single core is enough to satisfy Equation 4.8, using two or more is useful to reduce the total delay between the end of the acquisition of the B-scan and its visualization. This delay is computed as

$$T_{\text{delay}} = T_{\text{DMA}} + T_p + T_{\text{GPU}}, \quad (4.9)$$

where T_{DMA} is the time to transfer a B-scan from the ATS9350 to the application and T_{GPU} is the time needed to upload the final image to the GPU and display it. Using Figure 4.6, the DMA transfer time is computed as

$$T_{\text{DMA}} = \frac{\text{bytes per DMA buffer}}{\text{PCIe 2.0 throughput}} = \frac{\frac{1}{2} f_a \times 4096}{1.735 \text{ GB/s}}, \quad (4.10)$$

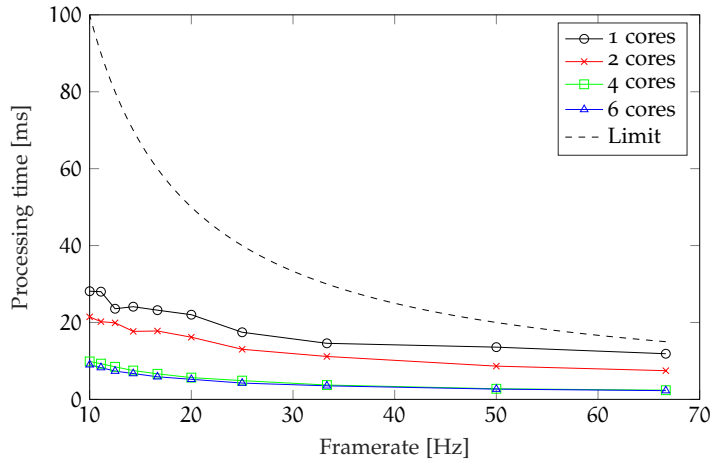


Figure 4.4: Processing time at different framerates and varying the number of CPU cores utilized.

where the PCIe throughput was measured in Section 3.3 using the AlazarDSO software. T_{GPU} was instead measured directly inside the application. The result is visible in Figure 4.5: using 4 cores, delays lower than 10 milliseconds are achievable even for large B-scans.

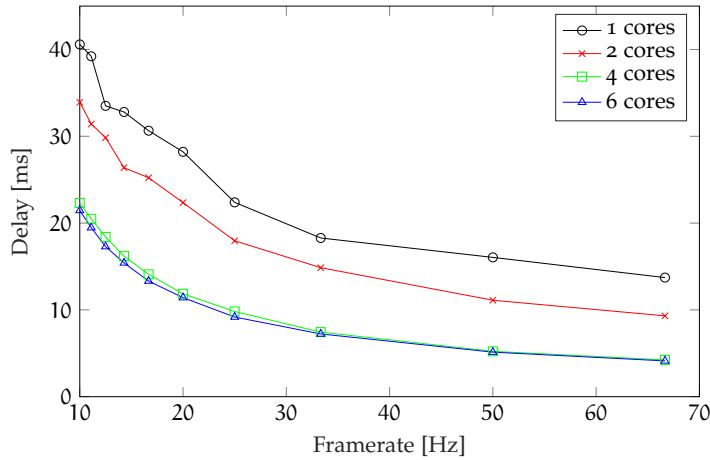


Figure 4.5: Total delay due to DMA transfer, CPU processing and GPU upload time.

Finally, the GPU throughput is estimated as

$$\eta_{GPU} = \frac{\text{bytes per image}}{\text{image upload time}} = \frac{\frac{1}{2} f_a \times 1024}{T_{GPU}}, \quad (4.11)$$

and illustrated in Figure 4.6. The maximum throughput achieved by OpenGL is ≈ 9.8 GB/s at 50 frames per second, corresponding to an image size of 1.024 MB. For lower framerates, and hence for bigger image sizes, the throughput decreases down to 7.7 GB/s, which is about half the maximum theoretical throughput supported by the PCIe 3.0 bus.

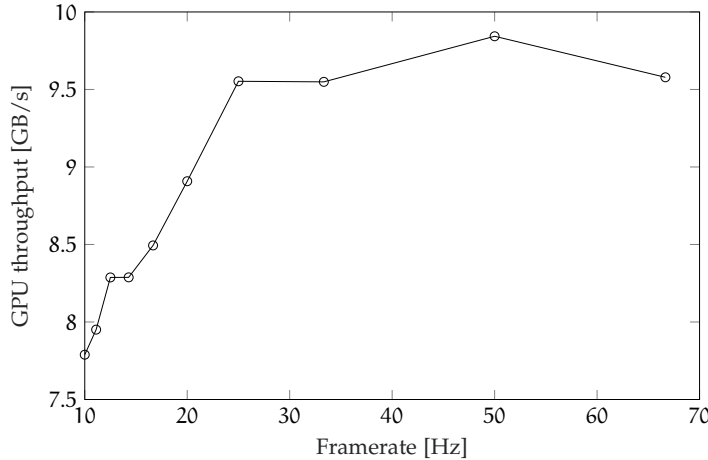


Figure 4.6: GPU throughput using OpenGL.

4.1.4 Saving data to disk

A desirable feature for a OCT software is the ability to save the acquired data to disk so that further post-processing can be performed. In Section 4.1.2.3 it was explained that each buffer returned by the board to the user application is duplicated, converted to floating point format and emitted using a Qt signal. A filesaving object connects to this signal and appends the received buffer to a dynamic FIFO queue. This structure is then emptied in an asynchronous loop running on a separate thread, writing each buffer to file in a binary format using standard C++ I/O operations. If the writing speed is not sufficiently high, the buffer fills up until the amount of Random Access Memory (RAM) available on the workstation is completely used or the acquisition stops.

Considering that the size of each buffer is

$$S = \frac{1}{2} \frac{f_a}{f_b} \times 1024 \times 4 \text{ bytes}, \quad (4.12)$$

the queue fills up at a rate of

$$\eta_q = S \cdot f_b = f_a \times 2048 \text{ bytes/s} = 204.8 \text{ Megabytes/s}, \quad (4.13)$$

meaning that a Solid State Drive (SSD) is needed for long acquisitions as regular Hard Disk Drives (HDDs) usually do not exceed write speeds of ~ 150 MB/s. In fact, the write speed of the HDD installed in the OCT workstation was benchmarked with the AlazarDSO software, resulting in 141.3 MB/s while the SSD averaged 348.7 MB/s.

4.1.4.1 The SSD write cliff

Even though this value is higher than η_q , for long acquisition sessions (tens of Gigabytes of data), the write speed of the SSD drops

significantly, the queue fills up and the application exhibits lags and unresponsiveness. This behaviour is due to the *SSD write cliff*. In flash-based SSDs, the memory consists in a number of blocks, each of which contains a number of pages. Blocks are the smallest erasable units whereas pages are the smallest writable units. After an SSD is filled with data, unused pages must be erased before new data is written. Since a block is the smallest erasable unit, in order to erase the unused pages the SSD must erase all pages on the block, regardless if they are active or unused. This means that active pages must be rewritten into another block with free cells. Writing a single page can result in multiple corresponding re-write operations, which can then trigger additional erase operations, causing a *write amplification*⁵.

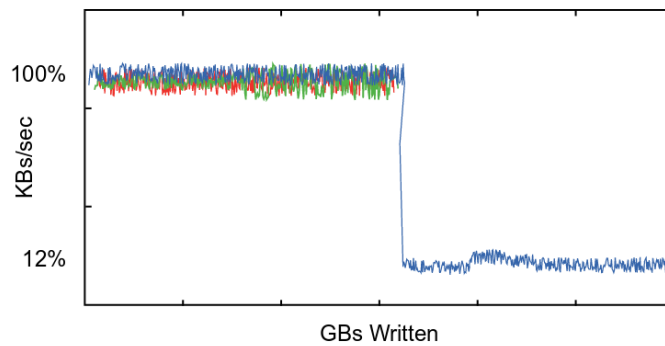


Figure 4.7: The SSD write cliff.

Solutions to mitigate this effect could not be investigated in detail and will be addressed in future works.

⁵ http://crestingwave.com/sites/default/files/collateral/velobit_whitepaper_ssdpfomancetips.pdf

4.2 ACQUISITIONS

In this section I will showcase a series of acquisitions made with the SS-OCT system that was described in the previous chapters and the custom-made OCT software.

4.2.1 *B-scans*

The first sample that was imaged is the Thorlabs test target introduced in Section 3.4.8. In Figure 4.8 we can see the highly reflective chrome coating on the top, while the bottom surface is only visible where the clear pattern is present.

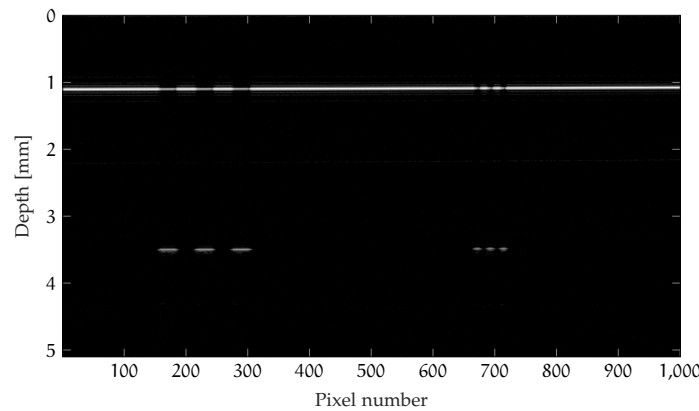


Figure 4.8: B-scan of the Thorlabs test target.

As explained in Section 3.4.8, the BPD utilized up until now does not amplify the received signal, meaning that the scattering generated by the analyzed samples could not be detected. To solve this issue, the BPD was replaced with another photodiode available in our laboratory, the Exalos EBR370010-02⁶, which is equipped with a 50 dB transimpedance amplifier. A few comments have to be made in this regard:

- Even though this receiver is designed to work in the 900-1200 nm range, acquisitions in the 1300 nm window were still possible.
- The nominal bandwidth of 100 MHz will theoretically limit the imaging depth of the system, but in practice this effect was not appreciable.
- The saturation power of -13 dBm required a slight adjustment of the reference arm: the collimator was misaligned until the received power was sufficiently low.

⁶ <http://www.exalos.com/balanced-receivers/>

The use of this receiver enabled the imaging of a lot of different samples. In Figure 4.9 a few are presented:

- Scotch tape (Figure 4.9a): the various layers of tape are clearly distinguishable. Each layer is measured at $\sim 60 \mu\text{m}$ of thickness using $n = 1$.
- A fiber optic ribbon cable consisting of 12 SMFs (Figure 4.9b).
- A dry orange peel (Figure 4.9c).

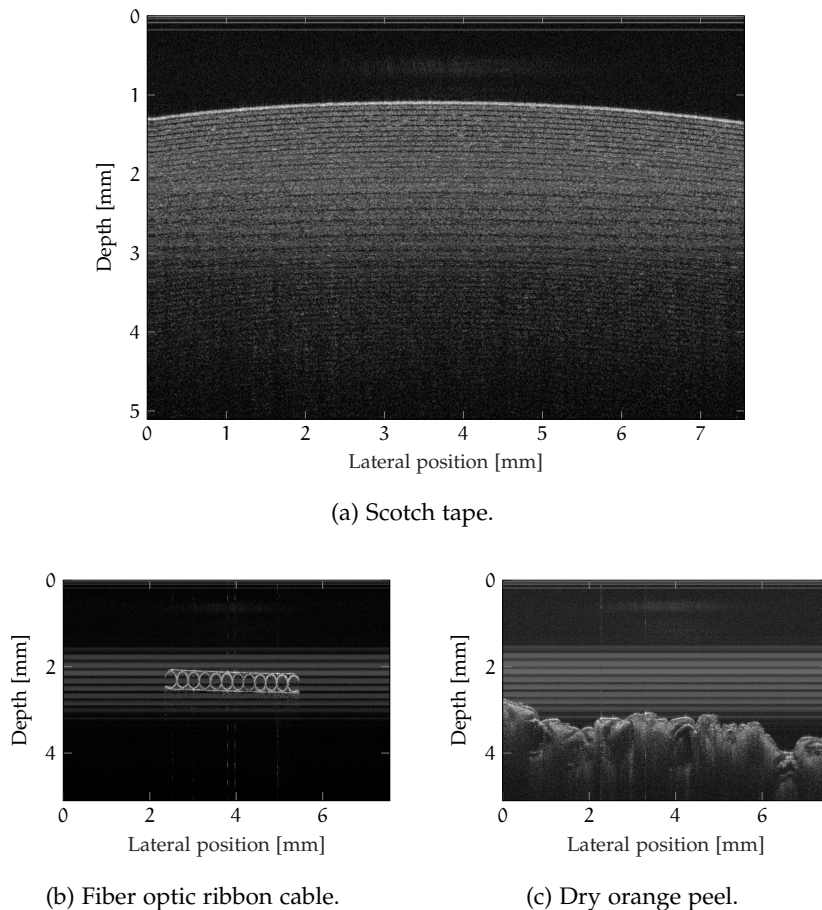


Figure 4.9: B-scans of various samples afflicted by striped artifacts.

In these images a series of horizontal bands occupy the middle of the imaging range. The cause of this effect has not yet been determined, but it has been observed that placing a polarization controller after the reference arm reduces the visibility of these artifacts.

This can be seen in the following images, representing:

- a fresh orange peel (Figure 4.10): the glans containing the natural oil are visible.
- a sliced cherry tomato (Figure 4.11). Notice the highly scattering seeds and the reticular structure of the pulp;

- a strawberry (Figure 4.12);
- an onion (Figure 4.13);
- human fingernail (Figure 4.14a) and fingertip (Figure 4.14b): fingerprints, epidermis and dermis layers are all clearly recognizable.
- a piece of beef steak (Figure 4.15): Figure 4.15a represents the various layers of muscle of a lean part of the steak, while in Figure 4.15b a section of fat tissue is illustrated.

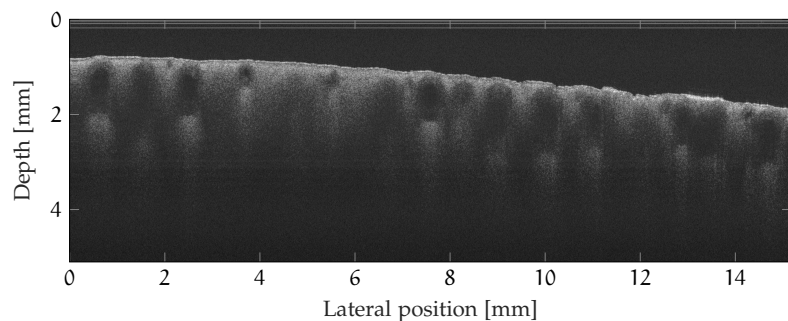


Figure 4.10: B-scan of an orange peel.

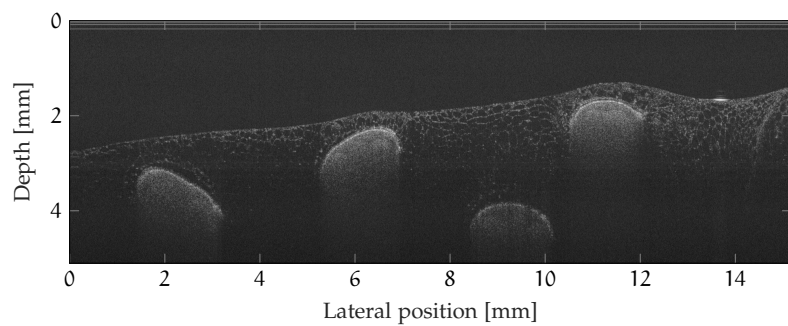


Figure 4.11: B-scan of a cherry tomato.

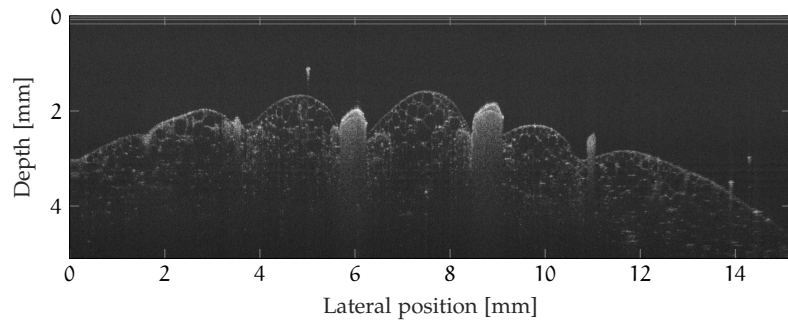


Figure 4.12: B-scan of a strawberry.

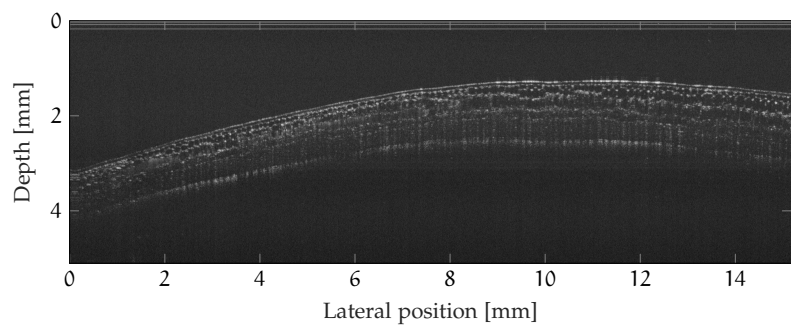


Figure 4.13: B-scan of an onion.

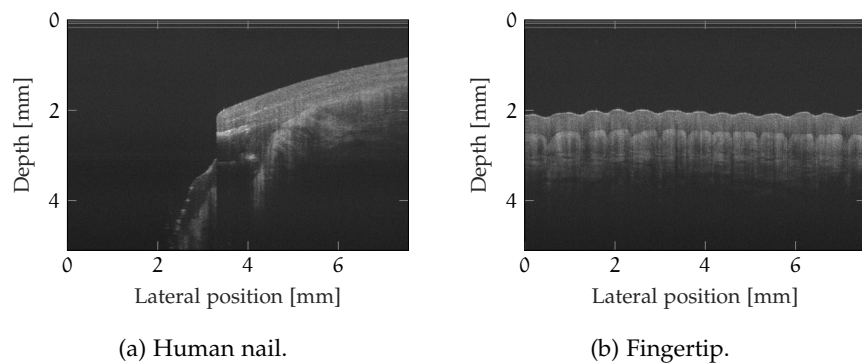


Figure 4.14: B-scans of a human finger.

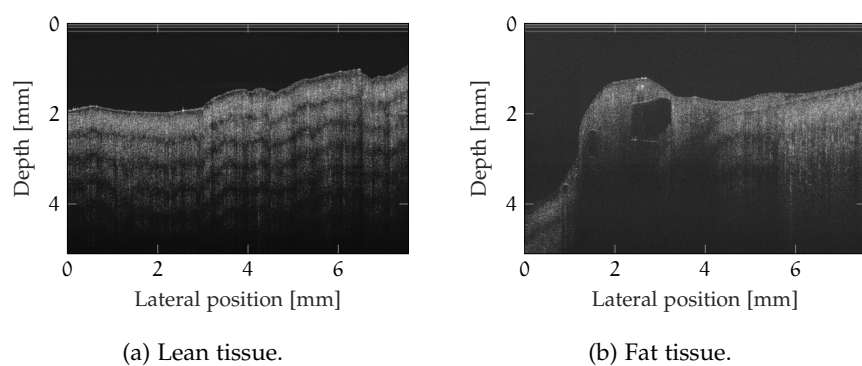


Figure 4.15: B-scans of a beef steak.

4.2.2 SS-OCT at 1060 nm

A second SS-OCT system working in the 1060 nm range and based on the design presented in this thesis was also tested. The setup is available in Figure 4.16: using a fixed fiber reflector in the reference arm requires a Variable Optical Attenuator (VOA) to limit the power received by the BPD and a more complicated calibration of the sample arm. In fact, after measuring the length of the reference arm with a OFDR, a fiber patch cord of the appropriate length was built by cutting and splicing two separate patch cords.

Optical components such as scanning lens and collimators are equivalent to those introduced in Chapter 3. The laser is instead a Santec HSL, capable of a selectable sweep rate and maximum imaging depth of ~ 9 mm.

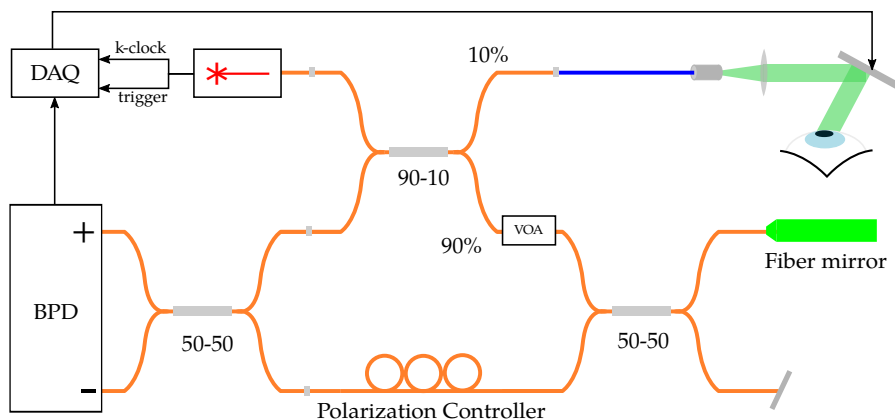


Figure 4.16: Setup of the SS-OCT system working in the 1060 nm range.

4.2.2.1 B-scans

Two B-scans acquired with this system are available in Figure 4.17: the juice vesicles of an orange slice are reported Figure 4.17a, while a scotch tape roll covering the entire imaging range is visible in Figure 4.17b.

By changing the state of polarization of the field reflected by the reference arm with the polarization controller, some birefringence-induced effects can be observed. An example is provided in Figure 4.18, where B-scans of a roll of scotch tape are acquired with the polarization controller in two different positions. We can see that in the right image a black band appears in the middle of the tape. The birefringence of the material at that specific depth causes a reflection with a state of polarization that is almost-orthogonal to that imposed by the polarization controller, resulting in a lower intensity interference.

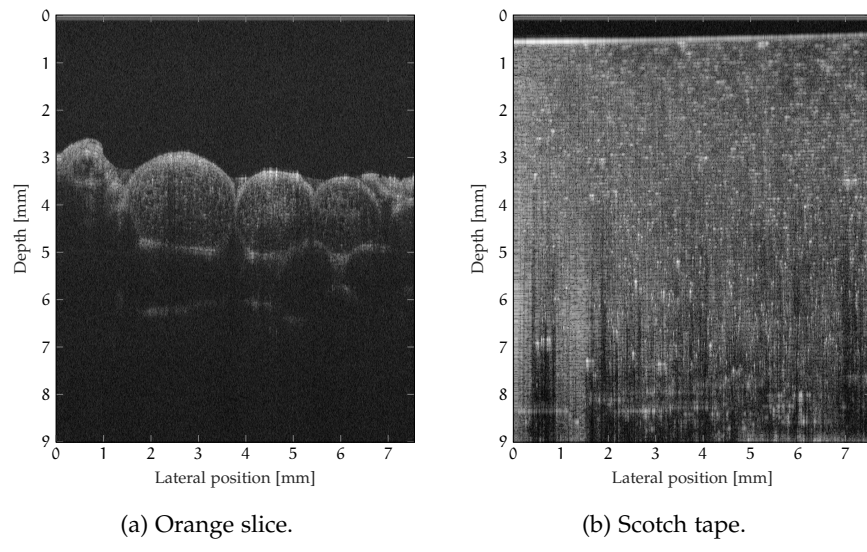


Figure 4.17: B-scans acquired with the 1060 nm system.

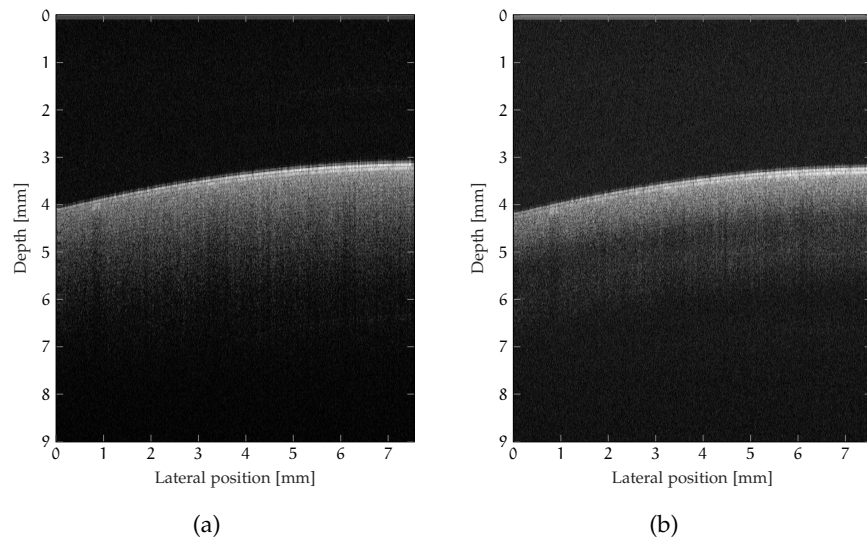


Figure 4.18: Birefringence effect on the B-scan of a scotch tape roll.

4.2.2.2 Imaging of dynamic samples

In order to test the OCT software with a dynamic sample, vinegar was poured in a microscope slide containing a small quantity of sodium bicarbonate. The two components cause a small reaction resulting in the generation of foam and bubbles. A few frames of the acquired

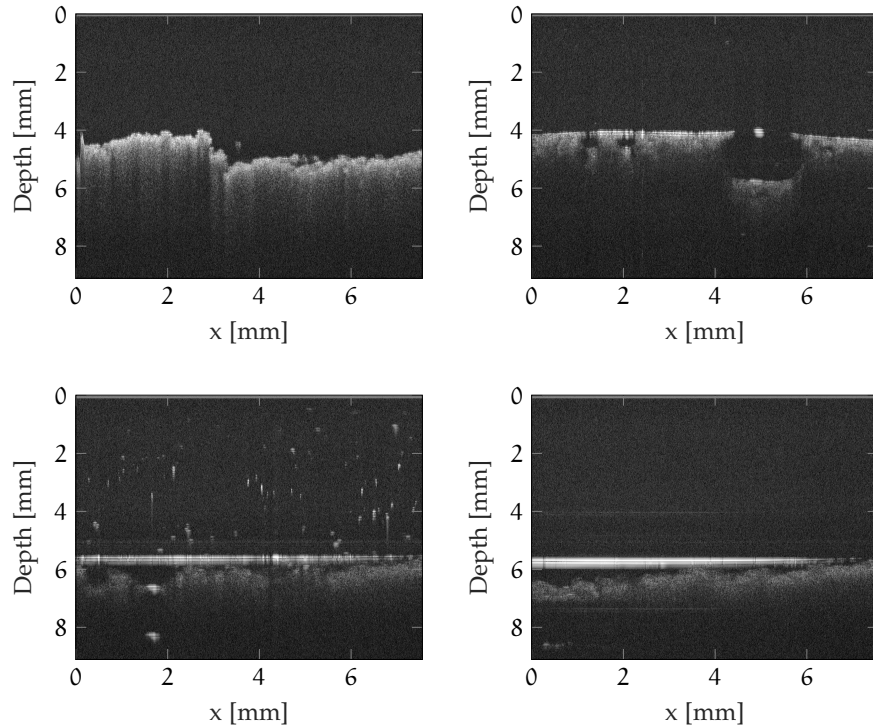


Figure 4.19: Reaction between sodium bicarbonate and vinegar.

video are presented in Figure 4.19: in the top left the bicarbonate is in its resting state; after pouring vinegar with a syringe, bubbles start forming (top right); a few seconds later the reaction slows down and the bicarbonate begins to settle on the bottom surface (bottom left) while a few particles jump out of the slide; finally the reaction halts (bottom right) with the particles completely sedimented on the bottom of the slide.

4.2.3 En-face images

In the introductory chapters of this thesis the concept of *en-face* images was explained: a frontal view of the imaged sample can be reconstructed from a series of B-scans acquired at slightly different positions on the transverse plane.

Usually, each pixel of the *en-face* image is obtained from the corresponding A-scan by summing its values: in this way parts of the sample that are beneath the surface are represented in the frontal view. A second method that can be used to build the image is selecting the maximum value of each A-scan. Since the reflection coming from the surface of the sample is often the most intense, the resulting image is essentially a magnified version of the sample.

The two processing methods are compared in the following figures, where the images on the left are generated with the *max* method, while those on the right are the result of the traditional *sum* method.

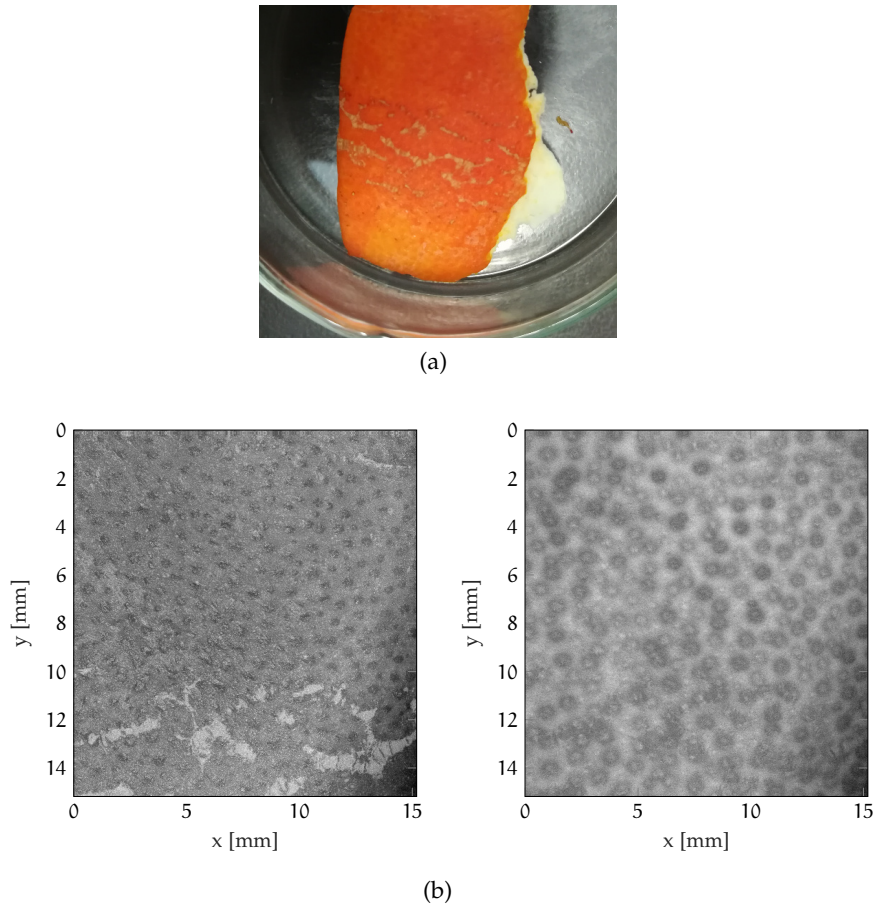


Figure 4.20: *En-face* view of an orange peel.

The difference between the two procedures is clearly observable in Figure 4.20, where the *en-face* view of an orange peel is presented. In the left image we can see the top portion of the glans and a defect

mark on the lower part of the picture, while on the right the glans are entirely represented and the defect is not visible.

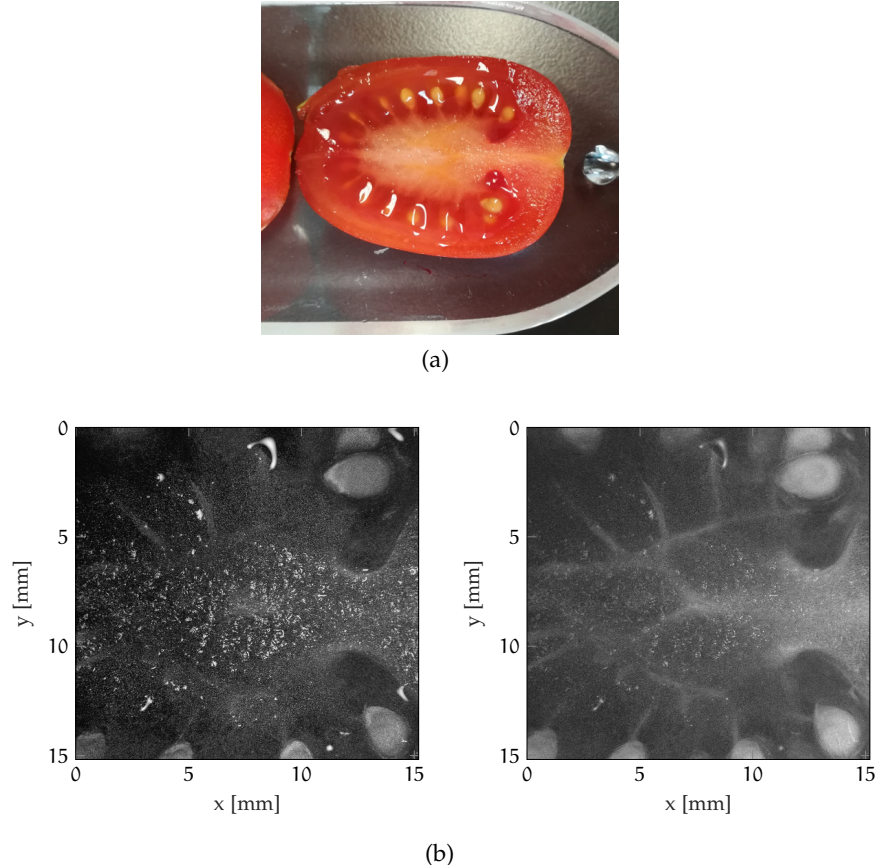


Figure 4.21: *En-face* view of sliced cherry tomato.

A similar effect is observable in the *en-face* projections of a cherry tomato presented in Figure 4.21, where the veins located underneath the top surface are only detected by the *sum* method.

Other examples are available in Figure 4.22 which includes, from top to bottom: a sliced onion, a human fingertip, a strawberry, and an orange slice. As can be seen from these figures, the *sum* method generally produces smoother images.

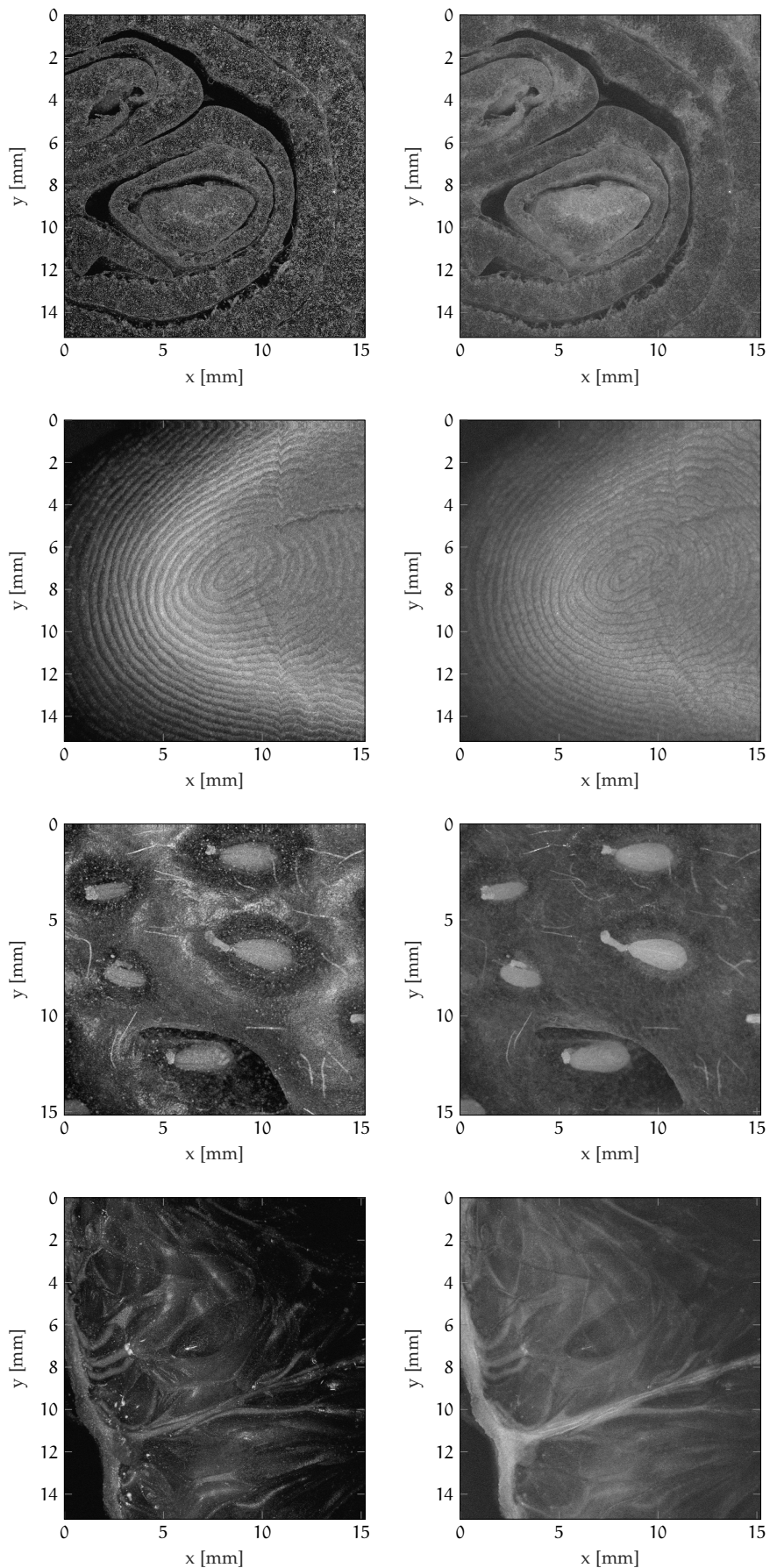


Figure 4.22: *En-face* images generated using the *max* (left) and *sum* (right) methods. From top to bottom: sliced onion, human fingertip, strawberry, orange slice.

4.2.4 Measuring the transversal resolution

The transversal resolution of the SS-OCT is experimentally determined by generating *en-face* images of the Thorlabs resolution test target introduced in Section 3.4.8. The resolution of an imaging system is often specified in *line pairs per millimeter* (lp/mm), whose value represents the smallest distance between two objects that can be registered by the system. The R1L1S1N test target is composed of five different patterns that will be presented in the following sections. Every acquisition has been performed by placing the top surface of the target on the focal plane of the scanning lens and with a sufficient number of points to guarantee a step size smaller than 1 μm in each direction.

4.2.4.1 Grids

This pattern consists in three grid patterns of different sizes: 10 μm , 50 μm and 100 μm . The 10 μm grid is a 20×20 array with 1.5 μm wide lines and a 10 μm pitch in the x and y directions. The 50 μm grid is a 20×20 array with 1.5 μm wide lines and a 50 μm pitch in the x and y directions. The 100 μm grid is a 20×20 array with 5 μm wide lines and a 100 μm pitch in the x and y directions.

The grid arrays are used to determine the distortion of a system, as the horizontal and vertical lines of the grid should be perpendicular to each other. A distorted image will show the lines as bent. The acquired image of this pattern is available in Figure 4.23: the 50 and 100 μm grids (center and right) are clearly visible and do not present any distortion. The 10 μm is instead completely blurred, with the lines appearing as a unique block. The resolution of the system is then necessarily worse than 10 μm .

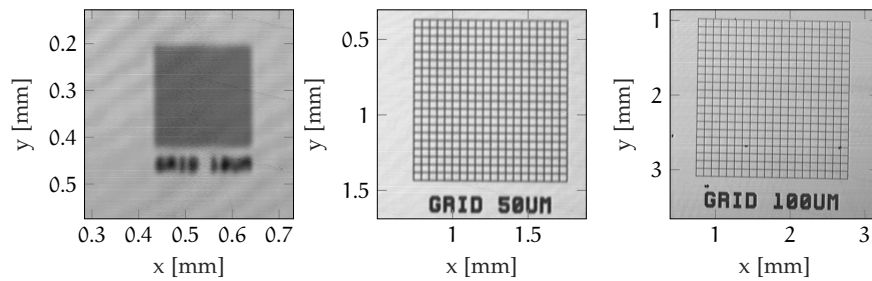


Figure 4.23: *En-face* projection of the grid pattern.

4.2.4.2 USAF 1951

The USAF 1951 is a resolution test pattern conforming to the MIL-STD-150A standard set by the United States Air Force in 1951. The pattern is composed by six groups of six elements, each consisting in

horizontal and vertical line pairs of different sizes. The resolution in lp/mm is computed as

$$\delta x, y = 2^{\text{Group} + \left(\frac{\text{Element}-1}{6}\right)}, \quad (4.14)$$

where "Element" is the largest set of non-distinguishable horizontal and vertical lines and "Group" is the index of the group in which this element is contained. The central part of this pattern is acquired and illustrated in Figure 4.24, where groups 4, 5, 6 and 7 are visible. Looking at elements 4, 5 and 6 of group 5, it appears that vertical lines are more easily distinguished than horizontal lines. In fact, the first element in which vertical lines are not distinguished is element 1 of group 6, while for horizontal lines it is element 6 of group 5. Using Equation 4.14, the x and y resolutions are

$$\delta x \approx 64 \text{ lp/mm} \Rightarrow 15.6 \mu\text{m} \quad (4.15)$$

$$\delta y \approx 57 \text{ lp/mm} \Rightarrow 17.5 \mu\text{m}, \quad (4.16)$$

which are a considerable improvement with respect to the theoretical value of 22.5 μm computed in Equation 3.18.

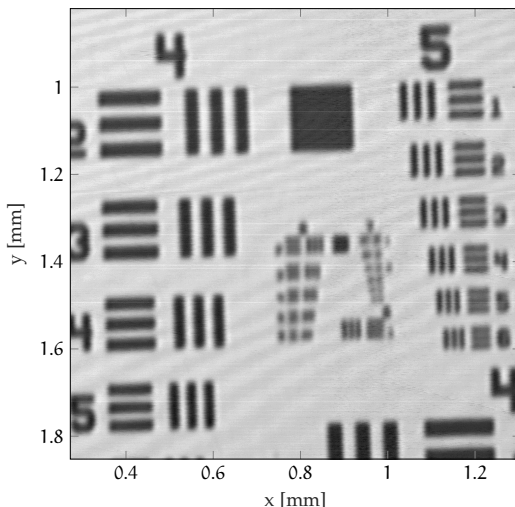


Figure 4.24: *En-face* projection of the USAF 1951 test target.

4.2.4.3 Ronchi rulings

Ronchi rulings are a set of parallel bars with widths that are equal to the distance between them. This pattern consists in thirteen 1 mm square Ronchi gratings with variable widths capable of measuring resolutions from 30 lp/mm up to 150 lp/mm. Figure 4.25 all the thirteen gratings are visible.

A detailed view of the 60, 70 and 80 lp/mm rulings is instead presented in Figure 4.26, where we can see that the vertical lines are distinguishable in the first two gratings but not in the last. Unlike

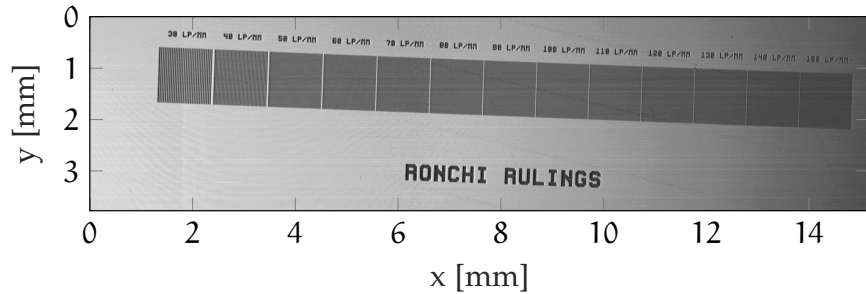


Figure 4.25: *En-face* projection of variable frequency Ronchi rulings.

with the USAF target, the resolution in this case is determined by the last grating that the system is able to resolve, resulting in

$$\delta x \approx 70 \text{ lp/mm} \implies 14.3 \mu\text{m} \quad (4.17)$$

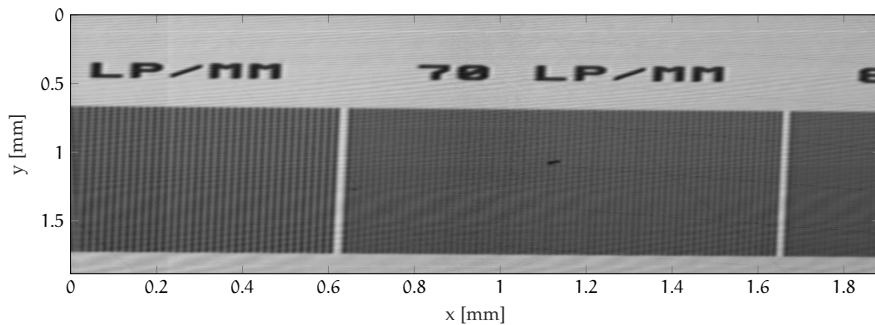


Figure 4.26: *En-face* projection of the 60, 70 and 80 lp/mm Ronchi gratings.

4.2.4.4 Star Sector

Sector star targets, also known as Siemens star targets, consist of a number of dark bars that increase in thickness as they radiate out from a shared center. Theoretically, the bars meet only at the exact middle point of the target, however this particular target has a blank center circle that cuts the bars off before they touch. Depending on the resolution of the optical system, the bars will appear to touch at some distance r from the center. By measuring this distance, the user is able to define the resolution of the optical system with the following equation:

$$\delta x = \frac{1}{2r \sin(\theta/2)}, \quad (4.18)$$

where θ is the number of degrees covered by one pair of light and dark bars, which for this particular target is equal to $\theta = 10^\circ$. To facilitate the reading of the radial distance, 10 clear concentric circles

cut through the bars. The radii of these circles are: 50, 100, 150, 200, 250, 300, 350, 400, 450 and 500 μm .

From Figure 4.27, the bars appear to touch when reaching the second circle, meaning that $r = 100 \mu\text{m}$ and resulting in

$$\delta x \approx 57.4 \text{lp/mm} \implies 17.4 \mu\text{m} \quad (4.19)$$

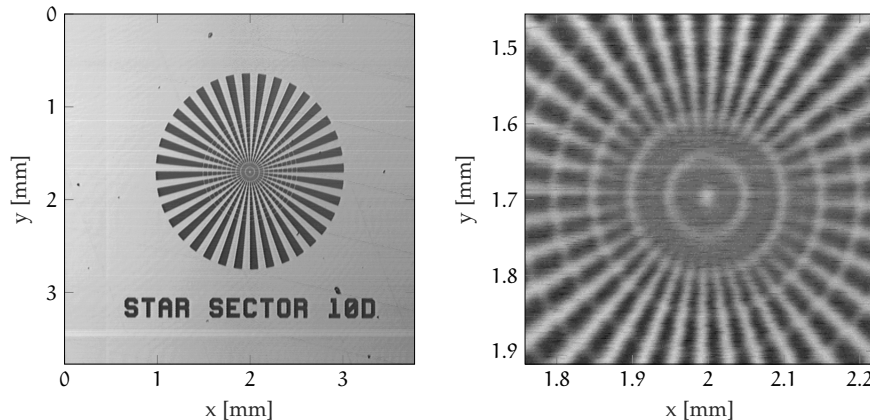


Figure 4.27: *En-face* projection of the star sector pattern.

4.2.4.5 Concentric circle

This pattern consists in 10 concentric circles with cross lines in the center. The radius of each circle is a multiple of 100 μm , starting from 100 μm up to 1 mm. The width of the arc line is instead 5 μm . Concentric circles are mainly used to identify focusing errors, astigmatism and other aberrations introduced by the scanning system.

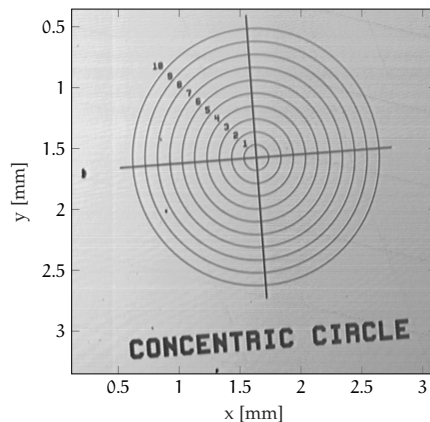


Figure 4.28: *En-face* projection of the concentric circles.

From Figure 4.28 no apparent distortion is visible, suggesting a correct setup of the focusing optics.

4.2.5 Volumetric Data

The last type of data that can be acquired with a OCT system is volumetric data. Each volume, or C-scan, is composed by a series of B-scans acquired at different positions on the sample. Unlike B-scans and *en-face* projections, 3D data requires complex and efficient algorithms for a correct visualization. For this purpose, a C++ OpenGL application implementing a basic frame-based volumetric algorithm was developed.

3D data is stored in a 3D texture object on the GPU, which will then compute a series of slices that cut through the texture perpendicular to the viewing direction (Figure 4.29). Slices are then blended together using a blending equation and displayed on screen. Each time the viewing direction changes the slices have to be recomputed.

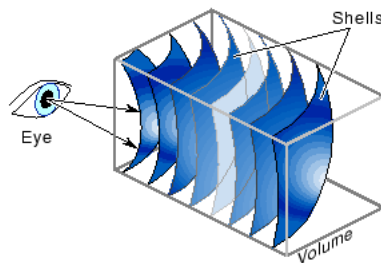


Figure 4.29: Slicing of a 3D texture.

In this implementation, B-scans are mapped from intensity values to RGBA space (Red, Green, Blue, Alpha) with a linear mapping, meaning that low intensity pixels will have a small Alpha value, making them more transparent. Advanced transfer functions can be implemented depending on the particular data that has to be visualized in order to use different colors for each material or structure in the sample.

The application can also slice the texture along three orthogonal axes to obtain an equivalent B-scan for each direction. An example of these slices can be seen in the top portion of Figure 4.30 along with the volumetric rendering of the USAF 1951 target.

Other examples of C-scan rendering are available in Figure 4.31, where the same datasets used to compute *en-face* projections in Section 4.2.3 are visualized.

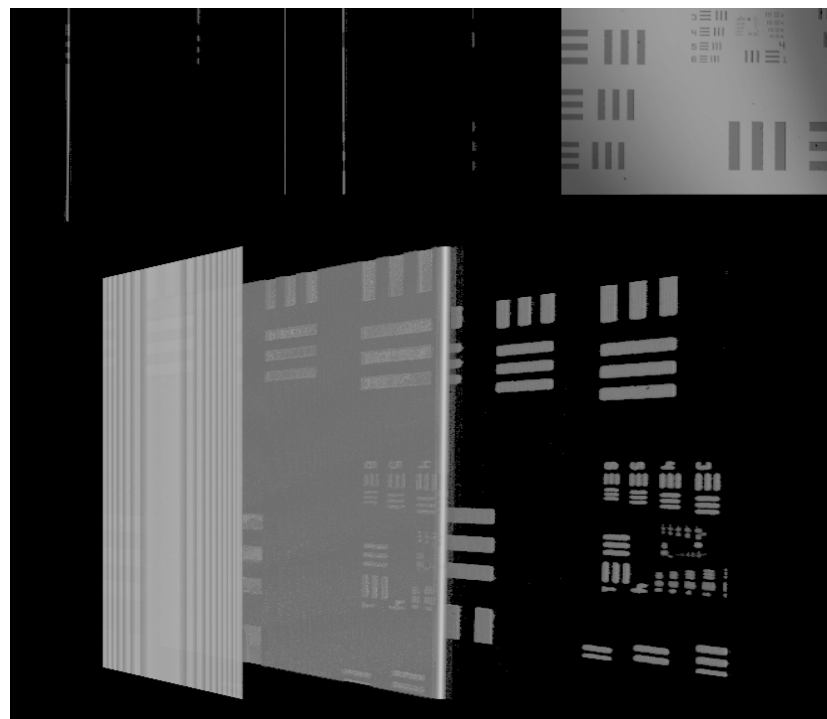
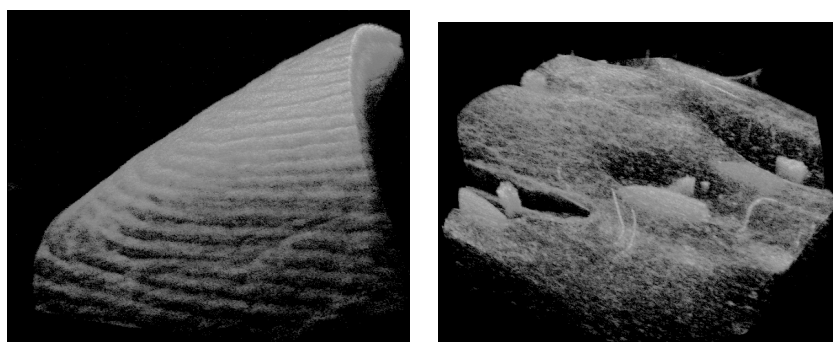
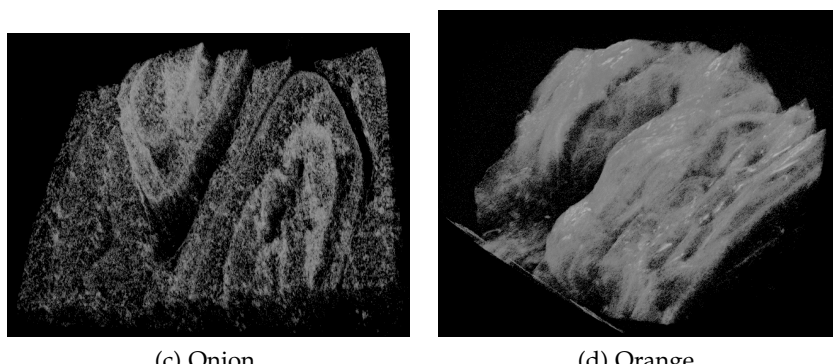


Figure 4.30: Volume rendering and slicing of the USAF 1951 target.



(a) Human fingertip.

(b) Strawberry.



(c) Onion.

(d) Orange.

Figure 4.31: Volume rendering of OCT data.

CONCLUSIONS

This thesis continued the work presented in [9], completing the design and implementation of a high-speed SS-OCT system. An axial resolution of $\sim 11 \mu\text{m}$ was achieved in air, comparable to the theoretical value of $\sim 9 \mu\text{m}$. Using a resolution test target the lateral resolution was also experimentally determined, reaching values as low as $\sim 14 \mu\text{m}$ and thus providing a substantial improvement on the $22 \mu\text{m}$ predicted by theory.

A multi-processing C++ OCT software capable of real-time low-delay video performance was entirely developed, integrating the control of the galvanometric mirrors and the high speed data acquisition board. Using this system, a wide range of samples have been imaged, producing axial, cross-sectional and volumetric data. Additionally, two methods to obtain *en-face* projections from three-dimensional data have been compared. Finally, a basic OpenGL volume rendering and slicing application has been implemented.

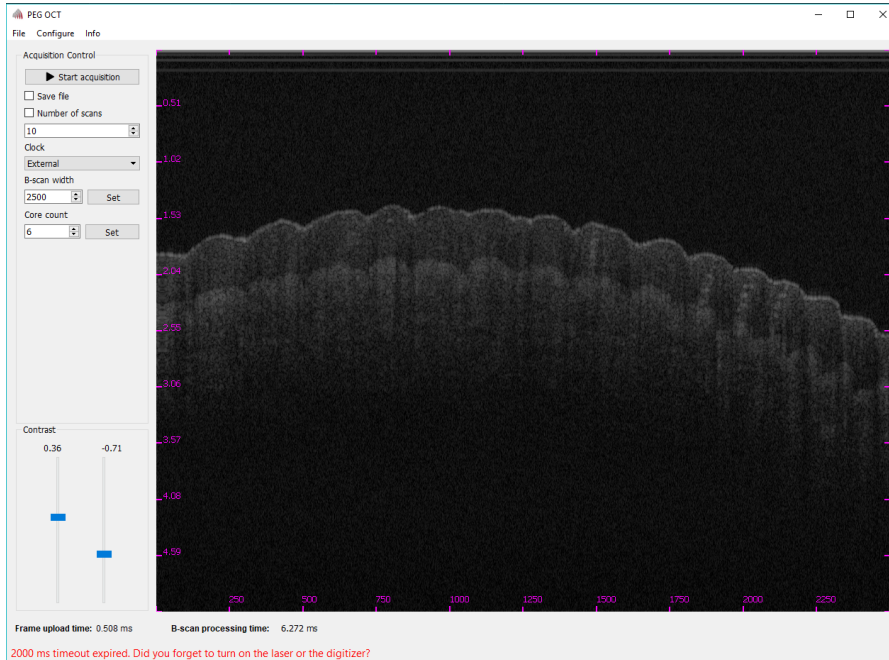


Figure 5.1: The GUI of the final OCT application, showing a B-scan of a finger.

Future developments of this work include the design of a polarization sensitive SS-OCT scheme capable of birefringence measurements,

along with the migration of the FFT computation from the FPGA module integrated on the DAQ board to the GPU, using a GPGPU approach. Several other improvements can be made, including the use of photodiodes designed to work in the 1310 nm range and the design of a dispersion compensating technique to enhance the axial resolution of the system. More advanced and efficient volume rendering algorithms can also be implemented to facilitate the visualization of 3D data.

A

APPENDIX - OFDR TRACES

Figure A.1, Figure A.2 and Figure A.3 represent the OFDR traces acquired for determining the length of the arms of the three fiber couplers, as discussed in Chapter 3. The title on top of each graph indicates the corresponding input port, while the color of the traces refers to the port connected to the patch cord (black is used instead of white).

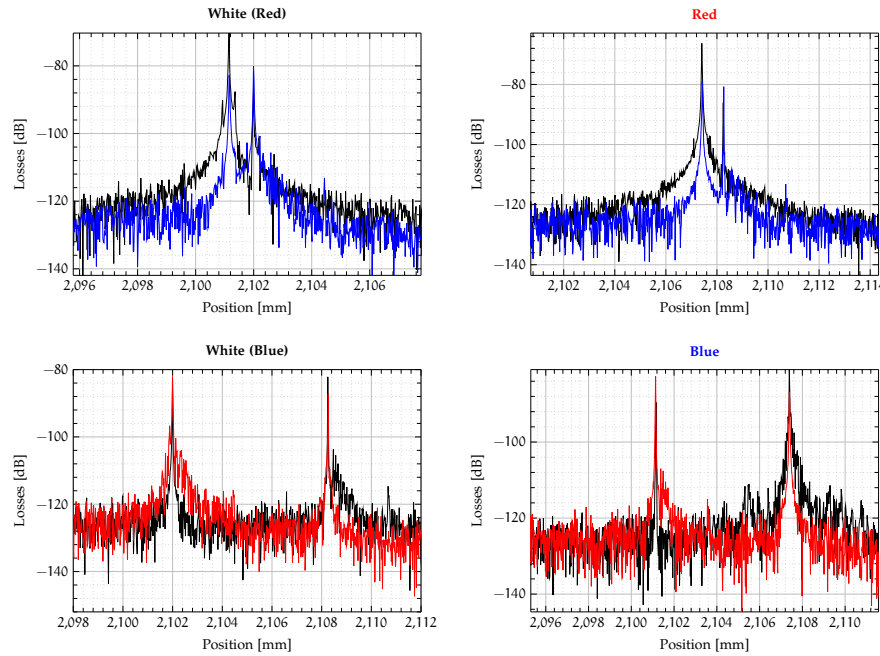


Figure A.1: OFDR traces of the first 50-50 coupler (Coupler A).

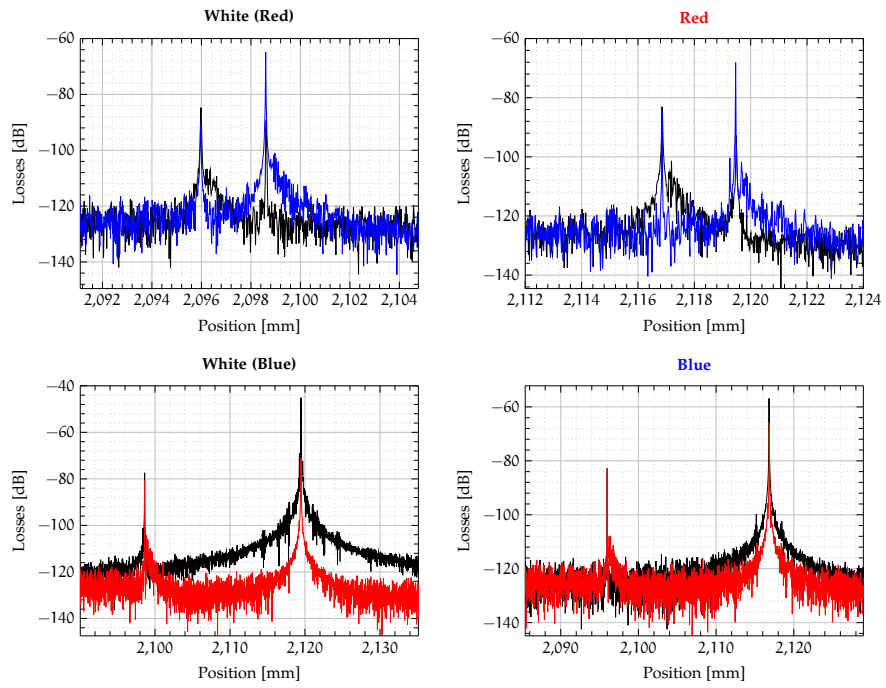


Figure A.2: OFDR traces of the second 50-50 coupler (Coupler B).

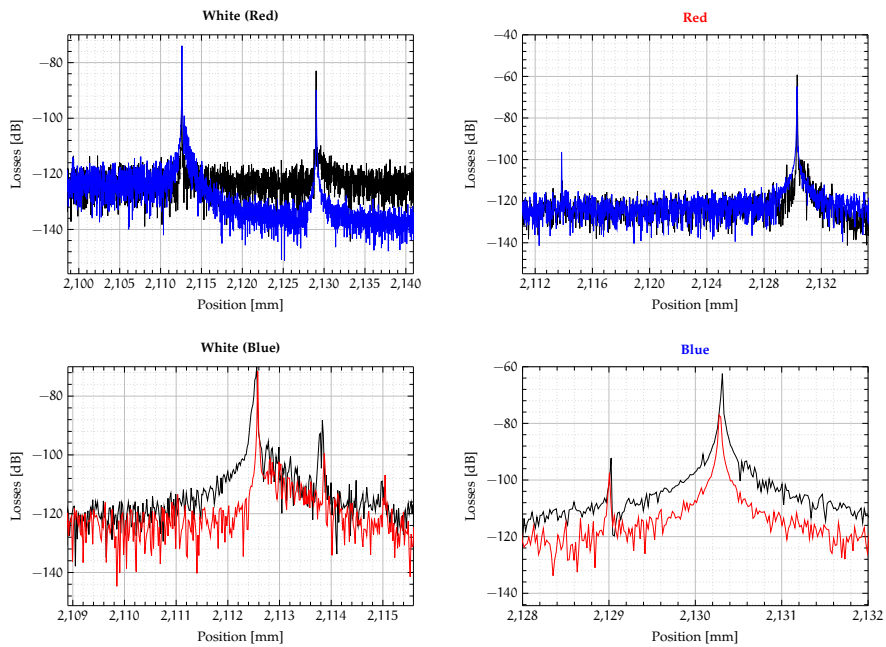


Figure A.3: OFDR traces of the 90-10 coupler.

BIBLIOGRAPHY

- [1] Erkki Alarousu, Leszek Krehut, Tuukka Prykäri, and Risto Myllylä. «Study on the use of optical coherence tomography in measurements of paper properties.» In: *Measurement Science and Technology* 16.5 (2005), p. 1131. URL: <http://stacks.iop.org/0957-0233/16/i=5/a=012>.
- [2] B. T. Amaechi, S. M. Higham, A. GH. Podoleanu, J. A. Rogers, and D. A. Jackson. «Use of optical coherence tomography for assessment of dental caries: quantitative procedure.» In: *Journal of Oral Rehabilitation* 28.12 (2001), pp. 1092–1093. ISSN: 0305-182X. DOI: 10.1046/j.1365-2842.2001.00840.x. URL: <http://doi.wiley.com/10.1046/j.1365-2842.2001.00840.x>.
- [3] Johannes F. de Boer, Thomas E. Milner, Martin J. C. van Gemert, and J. Stuart Nelson. «Two-dimensional birefringence imaging in biological tissue by polarization-sensitive optical coherence tomography.» In: *Optics Letters* 22.12 (1997), p. 934. ISSN: 0146-9592. DOI: 10.1364/OL.22.000934. URL: <https://www.osapublishing.org/abstract.cfm?URI=ol-22-12-934>.
- [4] Stephen A. Boppart, Juergen Herrmann, Costas Pitris, Debra L. Stamper, Mark E. Brezinski, and James G. Fujimoto. «High-Resolution Optical Coherence Tomography-Guided Laser Ablation of Surgical Tissue.» In: *Journal of Surgical Research* 82.2 (1999), pp. 275–284. ISSN: 00224804. DOI: 10.1006/jsre.1998.5555. URL: <http://linkinghub.elsevier.com/retrieve/pii/S002248049895555X>.
- [5] Stephen A. Boppart, Wei Luo, Daniel L. Marks, and Keith W. Singletary. «Optical Coherence Tomography: Feasibility for Basic Research and Image-guided Surgery of Breast Cancer.» In: *Breast Cancer Research and Treatment* 84.2 (2004), pp. 85–97. ISSN: 1573-7217. DOI: 10.1023/B:BREA.0000018401.13609.54. URL: <https://doi.org/10.1023/B:BREA.0000018401.13609.54>.
- [6] Max Born, Emil Wolf, A. B. Bhatia, P. C. Clemmow, D. Gabor, A. R. Stokes, A. M. Taylor, P. A. Wayman, and W. L. Wilcock. *Principles of Optics: Electromagnetic Theory of Propagation, Interference and Diffraction of Light*. 7th ed. Cambridge University Press, 1999. DOI: 10.1017/CBO9781139644181.
- [7] B E Bouma et al. «Evaluation of intracoronary stenting by intravascular optical coherence tomography.» In: *Heart* 89.3 (2003), pp. 317–320. ISSN: 1355-6037. DOI: 10.1136/heart.89.3.317. eprint: <http://heart.bmjjournals.org/content/89/3/317.full.pdf>. URL: <http://heart.bmjjournals.org/content/89/3/317>.

- [8] Brian Cabral, Nancy Cam, and Jim Foran. «Accelerated Volume Rendering and Tomographic Reconstruction Using Texture Mapping Hardware.» In: *Proceedings of the 1994 symposium on Volume visualization - VVS '94*. New York, New York, USA: ACM Press, 1994, pp. 91–98. ISBN: 0897917413. DOI: 10.1145/197938.197972. URL: <http://portal.acm.org/citation.cfm?doid=197938.197972>.
- [9] Marco Calabrese. «Progetto di un Tomografo a Coerenza Ottica ad Alta Velocità.» MA thesis. Dipartimento di Ingegneria dell'Informazione, Padova (Italy): Università degli Studi di Padova, 2017.
- [10] Dong-hak Choi, Hideaki Hiro-Oka, Kimiya Shimizu, and Kohji Ohbayashi. «Spectral domain optical coherence tomography of multi-MHz A-scan rates at 1310 nm range and real-time 4D-display up to 41 volumes/second.» In: *Biomedical Optics Express* 3.12 (2012), p. 3067. ISSN: 2156-7085. DOI: 10.1364/BOE.3.003067. URL: <https://www.osapublishing.org/abstract.cfm?URI=boe-3-12-3067>.
- [11] Tzu H. Chow, Khay M. Tan, Beng K. Ng, Sirajudeen G. Razul, Chia M. Tay, Tet F. Chia, and Wee T. Poh. «Diagnosis of virus infection in orchid plants with high-resolution optical coherence tomography.» In: *Journal of Biomedical Optics* 14.1 (2009), p. 014006. ISSN: 10833668. DOI: 10.1117/1.3066900. URL: <http://biomedicaloptics.spiedigitallibrary.org/article.aspx?doi=10.1117/1.3066900>.
- [12] Seyed Hamid Hosseiny Darbazi. «GPU-Accelerated Optical Coherence Tomography Signal Processing and Visualization.» PhD thesis. Universidade do Porto, 2016.
- [13] Anjul M. Davis, Michael A. Choma, and Joseph A. Izatt. «Heterodyne swept-source optical coherence tomography for complete complex conjugate ambiguity removal.» In: *Journal of Biomedical Optics* 10.6 (2005), p. 064005. ISSN: 10833668. DOI: 10.1117/1.2136147. URL: <http://biomedicaloptics.spiedigitallibrary.org/article.aspx?doi=10.1117/1.2136147>.
- [14] Al-Hafeez Dhalla, Derek Nankivil, and Joseph a. Izatt. «Complex conjugate resolved heterodyne swept source optical coherence tomography using coherence revival.» In: *Biomedical Optics Express* 3.3 (2012), p. 633. ISSN: 2156-7085. DOI: 10.1364/BOE.3.000633.
- [15] Wolfgang Drexler and James G. Fujimoto, eds. *Optical Coherence Tomography*. Cham: Springer International Publishing, 2015. ISBN: 978-3-319-06418-5. DOI: 10.1007/978-3-319-06419-2. URL: <http://link.springer.com/10.1007/978-3-319-06419-2>.

- [16] Klaus Engel, Martin Kraus, and Thomas Ertl. «High-quality pre-integrated volume rendering using hardware-accelerated pixel shading.» In: *Proceedings of the ACM SIGGRAPH/EUROGRAPHICS workshop on Graphics hardware - HWWS '01*. New York, New York, USA: ACM Press, 2001, pp. 9–16. ISBN: 158113407X. doi: 10.1145/383507.383515. URL: <http://portal.acm.org/citation.cfm?doid=383507.383515>.
- [17] P. F. Escobar, J. L. Belinson, A. White, N. M. Shakhova, F. I. Feldchtein, M. V. Karetz, and N. D. Gladkova. «Diagnostic efficacy of optical coherence tomography in the management of preinvasive and invasive cancer of uterine cervix and vulva.» In: *International Journal of Gynecological Cancer* 14.3 (2004), pp. 470–474. ISSN: 1048-891X. doi: 10.1111/j.1048-891x.2004.14307.x. URL: <http://doi.wiley.com/10.1111/j.1048-891x.2004.14307.x>.
- [18] Daniel Fried, John Xie, Sahar Shafi, John D. B. Featherstone, Thomas M. Breunig, and Charles Le. «Imaging caries lesions and lesion progression with polarization sensitive optical coherence tomography.» In: *Journal of Biomedical Optics* 7.4 (2002), p. 618. ISSN: 10833668. doi: 10.1117/1.1509752. URL: <http://biomedicaloptics.spiedigitallibrary.org/article.aspx?doi=10.1117/1.1509752>.
- [19] J G Fujimoto, C a Puliafito, R Margolis, A Oseroff, S De Silvestri, and E P Ippen. «Femtosecond optical ranging in biological systems.» In: *Optics Letters* 11.3 (1986), p. 150. ISSN: 0146-9592. doi: 10.1364/OL.11.000150. URL: <https://www.osapublishing.org/abstract.cfm?URI=ol-11-3-150>.
- [20] G. Loeb and J. K. Barton. «Imaging Botanical Subjects With Optical Coherence Tomography: A Feasibility Study.» In: *Transactions of the ASAE* 46.6 (2003), pp. 1751–1757. ISSN: 2151-0059. doi: 10.13031/2013.15616. URL: <http://elibrary.asabe.org/abstract.asp?JID=3&AID=15616&CID=t2003&v=46&i=6&T=1>.
- [21] T Gambichler, G Moussa, M Sand, D Sand, P Altmeyer, and K Hoffmann. «Applications of optical coherence tomography in dermatology.» In: *Journal of Dermatological Science* 40.2 (2005), pp. 85–94. ISSN: 09231811. doi: 10.1016/j.jdermsci.2005.07.006. URL: <http://linkinghub.elsevier.com/retrieve/pii/S092318110500201X>.
- [22] Alexandre R. Hariri Lidaand Tumlinson, David G. Besselsen, Urs Utzinger, Eugene W. Gerner, and Jennifer K. Barton. «Endoscopic optical coherence tomography and laser-induced fluorescence spectroscopy in a murine colon cancer model.» In: *Lasers in Surgery and Medicine* 38.4 (2006), pp. 305–313. ISSN: 0196-8092.

- DOI: 10.1002/lsm.20305. URL: <http://doi.wiley.com/10.1002/lsm.20305>.
- [23] David Huang et al. «Optical Coherence Tomography HHS Public Access.» In: *Science*. November 22.2545035 (1991), pp. 1178–1181. ISSN: 0036-8075. DOI: 10.1002/jcp.24872. The. arXiv: 15334406.
 - [24] Ik-Kyung Jang et al. «Visualization of coronary atherosclerotic plaques in patients using optical coherence tomography: comparison with intravascular ultrasound.» In: *Journal of the American College of Cardiology* 39.4 (2002), pp. 604–609. ISSN: 0735-1097. DOI: 10.1016/S0735-1097(01)01799-5. eprint: [http://www.onlinejacc.org/content/39/4/604](http://www.onlinejacc.org/content/39/4/604.full.pdf). URL: <http://www.onlinejacc.org/content/39/4/604>.
 - [25] Yali Jia et al. «Quantitative Optical Coherence Tomography Angiography of Choroidal Neovascularization in Age-Related Macular Degeneration.» In: *Ophthalmology* 121.7 (2014), pp. 1435–1444. ISSN: 01616420. DOI: 10.1016/j.ophtha.2014.01.034. URL: <http://linkinghub.elsevier.com/retrieve/pii/S0161642014001043>.
 - [26] Vrushali R. Korde et al. «Using optical coherence tomography to evaluate skin sun damage and precancer.» In: *Lasers in Surgery and Medicine* 39.9 (2007), pp. 687–695. ISSN: 01968092. DOI: 10.1002/lsm.20573. arXiv: NIHMS150003.
 - [27] Philippe Lacroute and Marc Levoy. «Fast volume rendering using a shear-warp factorization of the viewing transformation.» In: *Proceedings of the 21st annual conference on Computer graphics and interactive techniques - SIGGRAPH '94*. New York, New York, USA: ACM Press, 1994, pp. 451–458. ISBN: 0897916670. DOI: 10.1145/192161.192283. URL: <http://portal.acm.org/citation.cfm?doid=192161.192283>.
 - [28] Haida Liang, Marta Gomez Cid, R. G. Cucu, G. M. Dobre, A. Gh. Podoleanu, Justin Pedro, and David Saunders. «En-face optical coherence tomography - a novel application of non-invasive imaging to art conservation.» In: *Optics Express* 13.16 (2005), p. 6133. ISSN: 1094-4087. DOI: 10.1364/OPEX.13.006133. URL: <https://www.osapublishing.org/abstract.cfm?URI=oe-13-16-6133>.
 - [29] Wenchao Liao, Tianyuan Chen, Chengming Wang, Wenxin Zhang, Zhangkai Peng, Xiao Zhang, Shengnan Ai, Deyong Fu, Tieying Zhou, and Ping Xue. «Endoscopic optical coherence tomography with a focus-adjustable probe.» In: *Optics Letters* 42.20 (2017), p. 4040. ISSN: 0146-9592. DOI: 10.1364/OL.42.004040. URL: <https://www.osapublishing.org/abstract.cfm?URI=ol-42-20-4040>.

- [30] Monika Machoy, Julia Seeliger, Liliana Szyszka-Sommerfeld, Robert Koprowski, Tomasz Gedrange, and Krzysztof Woźniak. «The Use of Optical Coherence Tomography in Dental Diagnostics: A State-of-the-Art Review.» In: *Journal of Healthcare Engineering* 2017 (2017). ISSN: 20402309. doi: 10.1155/2017/7560645.
- [31] Mohammad Sultan Mahmud, David W. Cadotte, Barry Vuong, Carry Sun, Timothy W. H. Luk, Adrian Mariampillai, and Victor X. D. Yang. «Review of speckle and phase variance optical coherence tomography to visualize microvascular networks.» In: *Journal of Biomedical Optics* 18.5 (2013), p. 050901. ISSN: 1083-3668. doi: 10.1117/1.JBO.18.5.050901. URL: <http://biomedicaloptics.spiedigitallibrary.org/article.aspx?doi=10.1117/1.JBO.18.5.050901>.
- [32] MS; Michael R. Hee. «Quantitative Assessment of Macular Edema With Optcal Coherence Tomography.» In: *Journal of Chemical Information and Modeling* 39.9 (1995), pp. 1689–1699. ISSN: 1098-6596. doi: 10.1017/CBO9781107415324.004. arXiv: arXiv:1011.1669v3.
- [33] Michele Midrio. *Campi Elettromagnetici*. Via Lagrange 3, Padova - 35143: SGE Editoriali, 2006. ISBN: 88-86281-82-X.
- [34] T Prykari, J Czajkowski, E Alarousu, and R Myllyla. «Optical coherence tomography as an accurate inspection and quality evaluation technique in paper industry.» In: *Optical Review* 17.3 (2010), pp. 218–222. ISSN: 1340-6000. doi: 10.1007/s10043-010-0039-y.
- [35] Naresh Kumar Ravichandran, Eranga Wijesinghe, Seung-yeol Lee, Muhammad Faizan, Kibeom Park, Hee-young Jung, Mansik Jeon, and Jeehyun Kim. «Swept source optical coherence tomography for in vivo growth monitoring of capsicum annuum seeds treated with different NaCl concentrations.» In: 10323 (2017), pp. 1–4. ISSN: 1996756X. doi: 10.1117/12.2267457.
- [36] M Sabuncu and M Akdogan. «Photonic Imaging with Optical Coherence Tomography for Quality Monitoring in the Poultry Industry: a Preliminary Study.» In: *Revista Brasileira de Ciência Avícola* 17.3 (2015), pp. 319–324.
- [37] Marinko V. Sarunic, Michael A. Choma, Changhuei Yang, and Joseph A. Izatt. «Instantaneous complex conjugate resolved spectral domain and swept-source OCT using 3x3 fiber couplers.» In: *Optics Express* 13.3 (2005), p. 957. ISSN: 1094-4087. doi: 10.1364/OPEX.13.000957. URL: <https://www.osapublishing.org/oe/abstract.cfm?uri=oe-13-3-957>.
- [38] Carlo G. Someda. *Electromagnetic Waves*. 2nd ed. CRC, 2006.

- [39] Richard F. Spaide, James M. Klancnik, and Michael J. Cooney. «Retinal Vascular Layers Imaged by Fluorescein Angiography and Optical Coherence Tomography Angiography.» In: *JAMA Ophthalmology* 133.1 (2015), p. 45. ISSN: 2168-6165. DOI: 10.1001/jamaophthalmol.2014.3616. URL: <http://archopht.jamanetwork.com/article.aspx?doi=10.1001/jamaophthalmol.2014.3616>.
- [40] Rong Su, Mikhail Kirillin, Ernest W. Chang, Ekaterina Sergeeva, Seok H. Yun, and Lars Mattsson. «Perspectives of mid-infrared optical coherence tomography for inspection and micrometrology of industrial ceramics.» In: *Optics Express* 22.13 (2014), p. 15804. ISSN: 1094-4087. DOI: 10.1364/OE.22.015804. URL: <https://www.osapublishing.org/oe/abstract.cfm?uri=oe-22-13-15804>.
- [41] Yuankai K. Tao, Mingtao Zhao, and Joseph A. Izatt. «High-speed complex conjugate resolved retinal spectral domain optical coherence tomography using sinusoidal phase modulation.» In: *Optics Letters* 32.20 (2007), p. 2918. ISSN: 0146-9592. DOI: 10.1364/OL.32.002918. URL: <https://www.osapublishing.org/abstract.cfm?URI=ol-32-20-2918>.
- [42] G. J. Tearney, S. A. Boppart, B. E. Bouma, M. E. Brezinski, N. J. Weissman, J. F. Southern, and J. G. Fujimoto. «Scanning single-mode fiber optic catheter-endoscope for optical coherence tomography.» In: *Opt. Lett.* 21.7 (1996), pp. 543–545. DOI: 10.1364/OL.21.000543. URL: <http://ol.osa.org/abstract.cfm?URI=ol-21-7-543>.
- [43] Karin Wiesauer, Michael Pircher, Erich Götzinger, Siegfried Bauer, Rainer Engelke, Gisela Ahrens, Gabi Grützner, Christoph Hitzenberger, and David Stifter. «En-face scanning optical coherence tomography with ultra-high resolution for material investigation.» In: *Optics express* 13.3 (2005), pp. 1015–1024. ISSN: 1094-4087. DOI: 10.1364/OPEX.13.001015.
- [44] Wolfgang Wieser, Wolfgang Draxinger, Thomas Klein, Sebastian Karpf, Tom Pfeiffer, and Robert Huber. «High definition live 3D-OCT in vivo: design and evaluation of a 4D OCT engine with 1 GVoxel/s.» In: *Biomed. Opt. Express* 5.9 (2014), pp. 2963–2977. DOI: 10.1364/BOE.5.002963. URL: <http://www.osapublishing.org/boe/abstract.cfm?URI=boe-5-9-2963>.
- [45] Maciej Wojtkowski, Rainer Leitgeb, Andrzej Kowalczyk, Tomasz Bajraszewski, and Adolf F. Fercher. «In vivo human retinal imaging by Fourier domain optical coherence tomography.» In: *Journal of Biomedical Optics* 7.3 (2002), p. 457. ISSN: 10833668. DOI: 10.1117/1.1482379. URL: <http://biomedicaloptics.spiedigitallibrary.org/article.aspx?doi=10.1117/1.1482379>.

- [46] Tuqiang Xie, Huikai Xie, Gary K. Fedder, and Yingtian Pan. «Endoscopic optical coherence tomography with a modified microelectromechanical systems mirror for detection of bladder cancers.» In: *Applied Optics* 42.31 (2003), p. 6422. ISSN: 0003-6935. DOI: 10.1364/AO.42.006422. URL: <https://www.osapublishing.org/abstract.cfm?URI=ao-42-31-6422>.
- [47] Kang Zhang and Jin U. Kang. «Real-time 4D signal processing and visualization using graphics processing unit on a regular nonlinear-k Fourier-domain OCT system.» In: *Opt. Express* 18.11 (2010), pp. 11772–11784. DOI: 10.1364/OE.18.011772. URL: <http://www.opticsexpress.org/abstract.cfm?URI=oe-18-11-11772>.